Advanced Laser Applications for New Process Technologies and Diagnostics of Reactive Plasmas

Tsuyoshi Yamaguchi

Contents

Chapter 1

Introduction

1.1 Demand of high accuracy fabrication for new generation ULSIs

1.1.1 Trend of ULSIs

Recently, the market of information technology (IT) industry becomes around 17 % of that of all industries. Especially, silicon (Si) based ultra-large scale integrated circuits (ULSIs) are supporting all fields including electric communication in modern society. Therefore, the importance of ULSIs, which is a core device leading the IT industry, increases more and more. The ULSIs consist of Metal-Oxide-Semiconductor Field-Effect-Transistors (MOSFETs), capacitors, and multilevel wirings. Figure 1.1 shows a cross sectional schematic diagram of the basic structure of complementary metal-oxide-semiconductor (CMOS) [1]. In future ULSIs devices, the high-speed operation to process huge information as well as the complex function are demanded. The principle of the development is based on the scaling law [2].

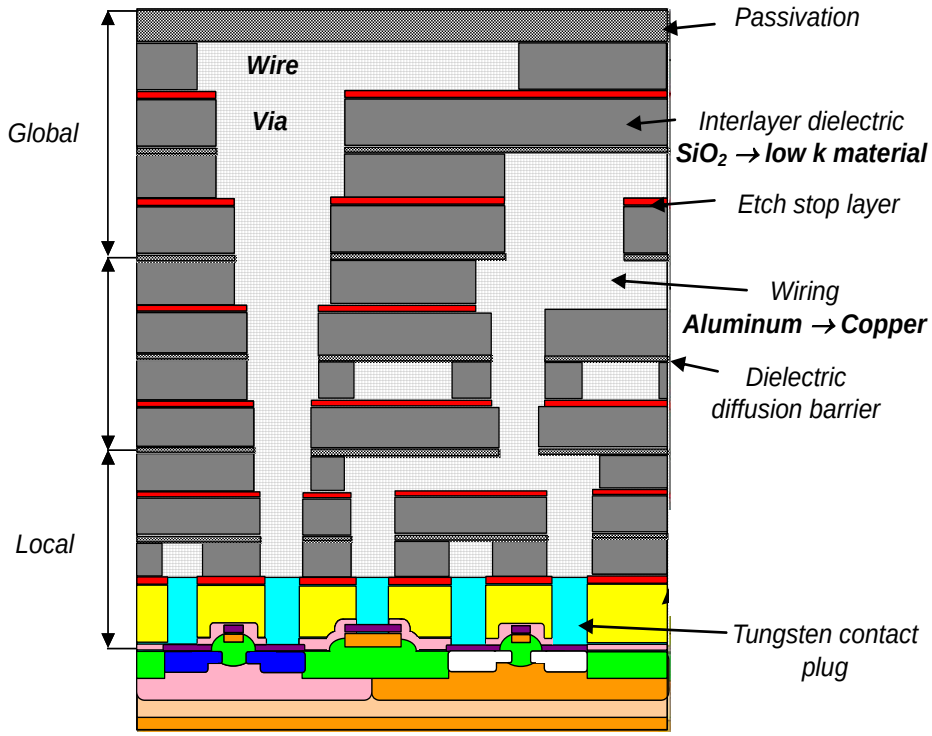

Figure 1.1 Cross section of CMOS LSI multilevel wiring structure.

Future demands for developing semiconductor technology are complied in International Technology Roadmap for Semiconductors (ITRS). For example, future demand device features are shown in Fig. 1.2. Responding to such demands the ULSI today has been developed by the shrinkage of device dimension and the high integration of semiconductor devices based on the scaling law. The shrinking of 70 % has been advanced in the size of the gate and wiring of the MOSFET every several years. Nowadays, the physical gate length of the MOSFET has already become 50 nm and below. As for high performances of micro processing units (MPU), the devices with the physical gate length of 25 nm have been developed. Moreover, first dynamic random access memory (DRAM) developed in 1970 was 1 Kbit in capacity, 1 Gbit DRAM was developed in 1998. A microprocessor (MPU) developed in Intel Corporation in 1971 consisted of about 2,300 transistors, and was operating at 108 kHz of clock frequency.

On the other hand, Pentium™ 4 processor developed in 2001 consisted of 55 million transistors, and was operating at 2.2 GHz of clock frequency. Recently, Intel Corporation has commercialized the 45nm Intel Core™ i7 Processor in 2009, formerly known as Nehalem. This is a complex system on a chip with multiple functional units and multiple interfaces, including four cores, transistors of 731 million, 8 MB of cache size and operating at frequency higher than 3.6 GHz [3]. The number of device components on a chip for MPU and DRAM follows an exponential growth as Dr. Gordon Moore predicted, permitting over millions and soon billions of transistors to be integrated on a chip. In 2014, the 1 Tbit DRAM and MPU with 3.6 billion transistors will be expected. For this purpose, the interconnecting technology is getting more complicated.

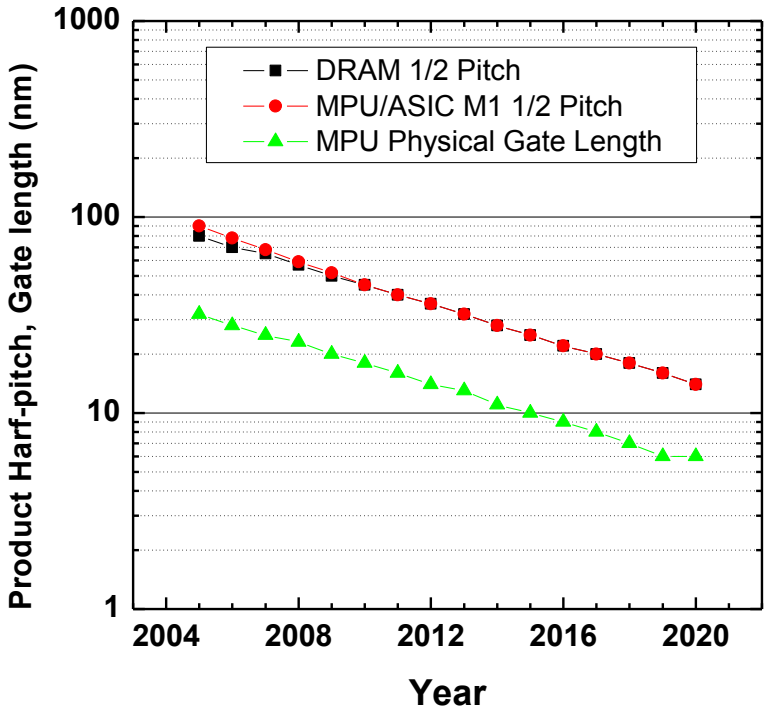

Figure 1.2 Technology node of the DRAM and MPU.

However, we have many difficulties in the device development because the multilevel interconnection process needs to use several kilometers of the metal interconnect wiring in one chip. Consequently, ULSI is mostly occupied with the interconnect wiring and the wiring delay has come to play a dominant role in determining the total signal delay in ULSI rather than basis gate delay [4,5]. It is important to reduce the wiring resistance and capacitance (RC delay) in order to improve signal transmission rates and power consumptions [6,7].

Recently, in order to reduce the RC delay, interlayer film with low dielectric (low-k) constant has been widely used in high speed and low power consumption CMOS devices in the replace of SiO_2 film, which is a traditional interlayer dielectric with a dielectric constant of 4.0. Historically, as a dielectric material, SiO_2, which has a unique structure (atom ratio of Si : O = 1 : 2 and film density of 2.4 g/cm^3), has been used because it has excellent thermal and mechanical stability and is easy to fabricate. Low-k films, such as SiOCHs [8-11], however, have C and H (such as methyl groups $-CH_3$) in the film network and have a relatively lower film density than SiO_2 to create a lower dielectric constant. Furthermore, many kinds of "SiOCH" exist with different film compositions that depend on the fabrication method, for example, chemical vapor deposition (CVD), plasma CVD, spin-on-glass (SOG), and so on. Table 1.1 shows dielectric materials for interlayer connections. The dielectric properties of films are related with the chemical composition and structures such as packing density and porosity. There are two types of dielectrics as low-k materials. One is inorganic dielectric film including SiO_2, SiOF [12-16], HSQ (hydrogensilses-quioxane) [17], and porous silica [18]. The other is an organic dielectric film including SiOCH [19,20], MSQ (methylsilses-quioxane) [21], polyimide, parylane, SiLK^{TM} [22], tefron, and

F-doped amorphous carbon [23]. Thermal stability, mechanical stability, adhesion, and etch and strip resistance are important properties required for low-k films.

Moreover, although aluminum (Al) has been used as a material of the interconnection wiring until 180 nm design rules, it has been transposed to copper (Cu) with low resistances after 130 nm design rules corresponding to the shrinking of the wiring [24]. The multilevel wiring of Cu is formed by repeating dual damascene processes. A typical process flow, specifically how to fabricate dual damascene interconnects, is as follows. First, a resist pattern for a via hole was formed on the stacked structure of SiO_2 over SiOCH. During etching of the SiOCH hole pattern, high selectivity to SiC is required to reduce the loss of the bottom stopper materials. Next, the via hole is filled with organic polymer, and a resist mask for trench pattern is formed on the SiO_2 layer. After that, the SiO_2 over SiOCH trench is etched, the resist mask is removed by ashing plasma, and the SiC stopper layer is finally etched.

Table 1.1 Dielectric materials for interlayer connections.

	Material		Process	Dielectric constance	Structure	Thermal stability	Concerns
Inoraganic dielectrics	SiO_2		plasma CVD	4	-	>1000℃	-
	SiOF		plasma CVD	3.4～3.6	-	>750℃	F atabity
	HSQ (hydrogensilses-quioxane)		Spin-On	2.8～3.0	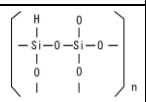	～400℃	Thermal stability O_2 plasma
	Porous silica		Spin-On	1.8～2.4	-	-	Mechanical
Organic dielectrics	SiOCH		plasma CVD	2.7～2.9	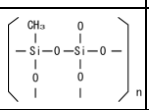	～700℃	O_2 plasma
	Porous SiOCH		plasma CVD	2.2～2.5	-	-	Mechanical O_2 plasma
	MSQ (methylsilses-quioxane)		Spin-On	2.7～2.9	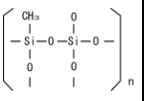	～700℃	O_2 plasma
	Pourous MSQ		Spin-On	1.8～2.5	-	-	Mechanical O_2 plasma
	Org-Polymer	Polyimide	Spin-On	3.0～3.5	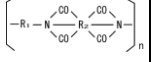	～450℃	O_2 plasma
		Parylane	Spin-On, CVD, plasma polymerization	2.2～3.0		～400℃	O_2 free process Adhesion
		B-staged polymer(SiLK™)	Spin-On	2.6～2.7	-	-	O_2 free process
		Tefron	plasma CVD	2.0～2.4	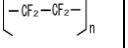	～100℃	Thermal stability O_2 plasma
	amorphous carbon (F-doped)		plasma CVD	<2.5	-	～700℃	O_2 plasma

1.1.2 Fluorocarbon chemistry in dielectric film selective etching

Figure 1.3 shows an illustration of a fluorocarbon-based plasma etching. Fluorocarbon gases such as CF_4, C_4F_8, and $C_5F_{10}O$ are introduced to the plasma reactor together with rare gases (Ar, He, etc.) and addition gases (O_2, N_2, H_2, etc.). Plasmas have been generated with the power of excitation frequencies from 13.56 MHz to 2.45 GHz. Radicals, ions, and electrons are generated by the electron impact dissociation of the feed gas. The species are generated by complicated chemical reactions in the plasmas, such as dissociation, excitation, ionization, recombination, elastic scattering, charge transfer, and so on. An excited state of the species can decay to lower energy state by emission of a photon.

The plasma provides radicals, ions, and electrons onto the wafer surface. The radicals diffuse thermally onto the wafer surface since they are electrically neutral. On the other hand, the ions are accelerated perpendicularly to the wafer surface by the sheath field on the wafer and then bombard the wafer surface [25]. In common case of the high-density plasma etching, the ion bombardment is enhanced by applying RF bias power to the wafer. Generally, the RF-bias frequency is chosen from a few hundred kHz to 13.56 MHz. One of the advantages of the plasma etching is its anisotropic etching characteristic. As ions perpendicularly bombard on the wafer, the activation of the surface takes place only on the bottom of the pattern, and not on the sidewall. As a result, the radicals contribute to etch the bottom and deposit fluorocarbon polymer on the sidewall, which prevents the sidewall from being etched. Ion energy distribution strongly depends on the frequency of the bias. The radicals and ions react on the surface, and the byproducts are emitted to the plasma region. The byproducts are exhausted together with other products from the plasma by a pump system.

It is believed that CF_x (x=1-3) radicals work as precursors of the selective etching of SiO_2 films. CF_x (x=1-3) radicals etch the surface film, if the wafer surface is activated by the ion bombardment with high energies [26-29]. On the contrary, the CF_x (x=1-3) radicals work as precursors of the deposition of fluorocarbon polymers, if the surface is insufficiently activated by the ion bombardment with low energies [27]. Thus, the etching process using fluorocarbon plasmas proceeds in competition with the polymer deposition on the surface of the wafer [30-35]. The formation of the fluorocarbon polymer strongly depends on plasma chemistry, that is, the selection of feed gases considerably influences the selectivity. The rare gases and addition gases are introduced in order to control the behaviors of ions and radicals in the plasma, and to control the formation of the polymer on the surface. Rare gas such as Ar plays a role to achieve a high ion/radical ratio. Addition gases such as H_2, O_2, and N_2 molecules increase the chemical reaction in the plasma and on the surface. When H_2 gas is added to the fluorocarbon plasma, fluorocarbon radicals is generated with not only electron impact dissociation, but also F abstraction by H atoms [36]. Additions of O_2 and N_2 gases are known to play a role to suppress the excess deposition of polymers on the surface. O atoms are easy to associate with fluorocarbon radicals, and to decrease the density of fluorocarbon radicals in the plasma [37]. However, behaviors of fluorocarbon radicals in the N_2 addition plasma have not been understood enough. The temperature of radicals and neutral molecules is one of the most important parameters for understanding and controlling the plasma process, because the temperature governs the density profiles, the transport of radicals, the reaction rate on the surface, and so on.

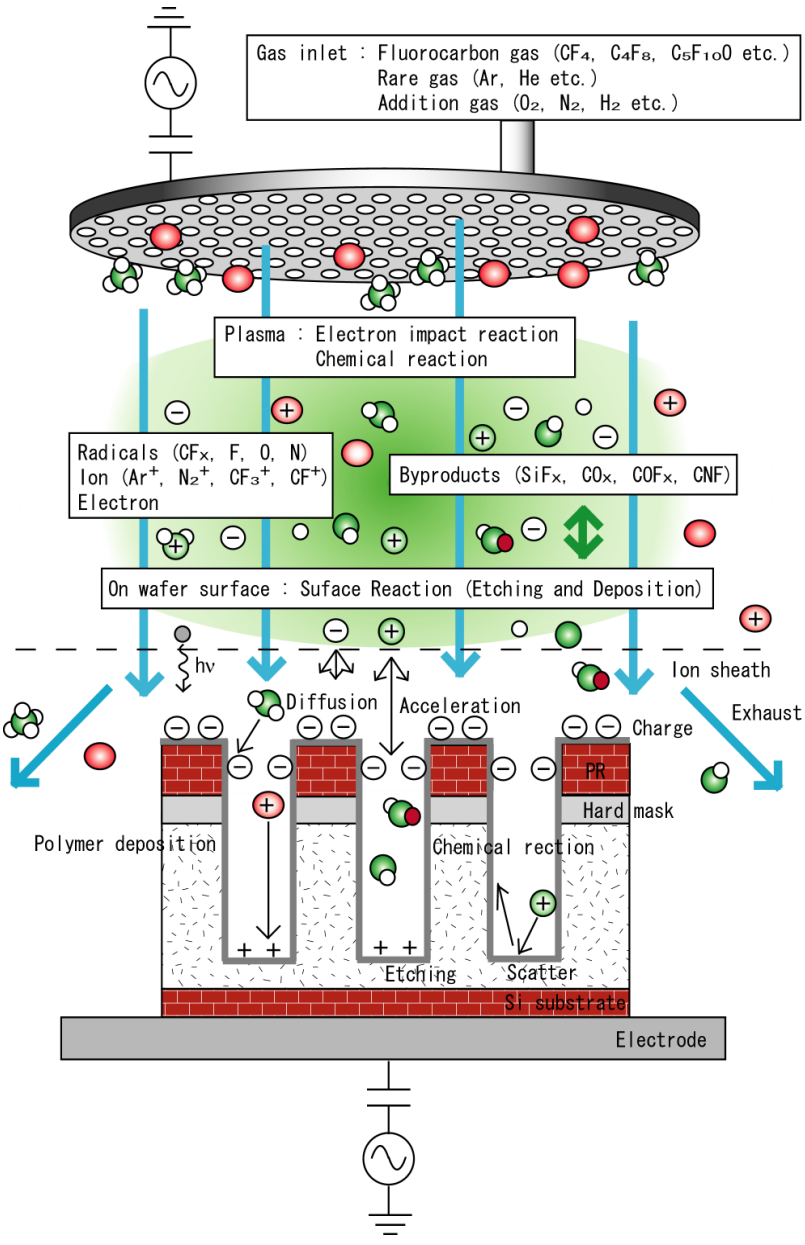

Figure 1.3 Illustration of a fluorocarbon-based plasma etching.

Perfluocarbon (PFC) gases have been widely used in etching processes of dielectric films, in deposition processes of fluorocarbon films and in cleaning processes of chemical vapor deposition (CVD) chambers in fabricating ultralarge-scale integrated circuits (ULSIs). Etchings of poly-Si and dielectric films such as SiO_2 and SiOCH are essential processes for fabricating deep contact holes and interconnections. The poly-Si is fabricated on the Si substrate by a thermal CVD using a SiH_4 gas after ion implantations. The poly-Si is etched for the gate circuits using high-density plasmas employing, Cl_2, CF_4, HBr, and so on.

The contact hole is needed to provide an electrical contact between the field-effect-transistor (FET) and the upper layer. Conventionally, SiO_2 are used as the insulator between the contact holes, and etched by high-density plasmas employing PFC gases such as C_4F_8, CF_4, CHF_3, and so on.

The first metal layer of the contact hole is fabricated by a single damascene process in the CMOS. Tungsten (W) plugs are used as the metal of interconnects on the silicided regions of the silicon and poly-Si. The tungsten plug has been deposited in the contact hole by the CVD process using a WF_6 gas. In these CVD processes, serious problems arise when poly-Si and W films are deposited on the chamber walls. These polymers deposited on the chamber wall cause the generation of the excessive particles in the chamber. Therefore, these polymers greatly influence the quality of films and the reproducibility of the CVD process. Plasma cleaning with SF_6 and PFC (CF_4, C_2F_6)/O_2 gases has been generally used for removing the particles. In these chamber cleaning processes, F atoms generated from the electron impact dissociation of SF_6 and PFC gases play an important role in etching reactions of poly-Si and W films.

Thus, PFC gases have been widely used for various fields and are very

important for the current and future semiconductor industry. It is believed that the fluorocarbon chemistry plays important roles in the fabrication of ULSI.

1.1.3 Problems in dielectric film etching

Etchings of dielectric films are important processes in fabricating the contact hole and trench. As technology nodes are progressed, the process window for the plasma process is more tight and difficult.

Table 1.2 shows the problems of dielectric film etching in fluorocarbon plasma process. One of problems in the etching process with high-density plasmas is poor etching selectivity of a dielectric film over photo resist (PR) and underlying materials. This is due to poor protection films deposited on the surface. The selective deposition on PR and underlying materials decreases their etch rate, and therefore increases the selectivity. However, excessive amounts of the CF_x (x=1-3) radicals result in the deposition on dielectric films as well, which cause an etching stop and taper shape [40].

Other problem is the etch rate uniformity. In the case of a 200 mm wafer, it is said that uniformity of less than 3 %, within a diameter of 195 mm, is required [41]. Recently, semiconductor industries demand large-area etching of a 300 mm wafer. Non-uniformity causes excess discharge times to etch dielectric films over the underlying materials. One of the mechanisms of etching non-uniformity is non-uniform distribution of ions, radicals, and electric field over the wafer [41, 42]. Koshiishi *et. al.* reported that the improvement of the electric field enable us to control a etch rate distribution [41]. Diagnostics of CF_x (x=1-3) radicals and active species are useful to understand the poor selectivity and etching non-uniformity.

High-aspect-ratio SiO_2 contact-hole etching is one of the key technologies.

However, there are many serious problems, such as charge-buildup damage [43-45], etching-stop [46], and microloading effects [46]. Charge accumulation in contact hole during etching is one of the main causes of these problems. It is well known that fluorocarbon polymers deposited on the sidewall influence on the etching characteristics and charge accumulation.

Table 1.2 Problems of dielectric film in fluorocarbon etching plasma process.

Problem	Cause
Poor etching selectivity	Poor protection film
Etching nonuniformity	Ion and radical nonuniformity
Microtrench	Positive and negative charge
Microloading	Transfer-dependence on aspect ratio
O_2 damage	Oxidation ($SiOCH \rightarrow SiO_2$) in strip resist process
Resist degradation	Resist modification
Line edge roughness	Sidewall roughness
Facet	Etcing yield dependence on incident angle
VUV damage	VUV irragiation

Microtrench is another problem observed in the dielectric etching. The formation of microtrench during the etching of dielectric films is often explained by two reasons, that is, ion scattering from sloped sidewalls [47-49], and different charging at the sidewalls and bottom of the contact hole due to a difference in the angular

distribution for ions and electrons [50,51]. As shown in Table 1.2, there are many other problems during etching processes. It is important to understand the mechanism of the problem and to monitor the plasma using plasma diagnostics.

Recently, the interlayer film with low dielectric constant (low-k) has been used in the replace of SiO_2 films. Among the low-k materials, SiOCH films are one of the most attractive and useful materials. The etching of SiOCH has problems of plasma damage as compared with conventional SiO_2. One of the plasma damages is oxidation reaction during the etching process and PR stripping process using O_2 plasma [52]. The sidewall is modified with O_2 plasma, that is, SiOCH is converted to SiO_2. As a result, the dielectric constant is increased. In order to decrease the dielectric constant of SiOCH films for the future technology node, they would use porous films. Plasma damage becomes more serious problem in porous-SiOCH because the damage are related with the pore structure [53, 54].

O_2 gas has been added to fluorocarbon gases plasma in the SiO_2 etching in order to suppress excess depositions of polymer on the etched surface. On the other hand, N_2 gas is sometimes added to fluorocarbon gases plasma in the SiOCH etching. It is believed that N_2 plasma makes protection films on the stop layer of SiC and SiN to increase selectivity. The N_2 addition to fluorocarbon plasmas has advantages of high selectivity and low plasma damage because of O_2-free chemistry. Typically, gas mixtures such as Ar, N_2, C_4F_8, and CF_4 gases were used for the etching of SiOCH [52, 55-57]. It is essential to understand behaviors of radicals in SiOCH etching and to achieve effective plasma process.

1.1.4 New technology for advanced plasma processing

The successful use of capacitively coupled plasmas (CCPs) in microelectronics fabrication is predicated because of the ability of controlling the energy and angular distributions of reactant species to the wafer [58]. In conventional single-frequency CCPs, there is a tradeoff between controlling the ion energy and angular distribution and the rate of plasma production as a function of excitation frequency and gas pressure [59]. More advanced dual-frequency CCPs separate these functions by attempting to control the IEAD using low frequency excitation and using a high frequency excitation to control the production of the plasma and so the magnitude of fluxes to the substrate [60].

Recently, dual frequency CCP with negative dc bias superposed on the VHF power on the upper electrode have been proposed as a new technology for advanced plasma processing. The superposition of a negative dc voltage to the lower electrode in parallel-plate type CCP was first reported in the 1990s [61]. Recently, several researchers reported their computational results that the sheath structure is superposed electromagnetically by a dc sheath and an rf sheath when the negative dc voltage is applied to the electrode [62-67]. It has been experimentally recognized that the sheath voltage is modulated by this superposition, and the bombardment of ions accelerated by the high sheath voltage will enhance the generation of secondary electron emission [67]. The electrons generated on the electrode surface accelerate back into the plasma, thereby increasing the plasma density [62-67]. Nagai *et al*. reported that the secondary electrons injected from the top electrode superposed by two different frequencies of 450 kHz and 13.56 MHz were accelerated by the sheath and suppressed the micro-trenching at deep trench bottom due to the relaxation of positive charge on the trench bottom by

high energetic electrons [68]. Thus the highly energetic secondary electrons improved the etching properties. Very recently, Wang and Kushner reported plasma etching of SiO_2 in a dc-augmented CCP using a *c*-C_4F_8/O_2/Ar gas mixture. Their computational results showed that improvements for randomly occurring divergence of hole or trench shapes from the vertical were obtained by impinging highly energetic secondary electrons onto the lower electrode surface [69, 70].

1.2 Diagnostics for activated species in the plasma

Activated species are very important in determining the performances of the plasma process. Therefore, the information on behaviors of these species in the gas phase is essential to understanding the plasma chemistries and thereby to control the plasma in advanced plasma processing. In reactive plasmas, many species have been investigated so far by using various diagnostics techniques.

1.2.1 Measurement for atomic radicals

Table 1.3 shows measurement techniques for atomic radicals. Optical emission spectroscopy (OES) is one of the most popular techniques to measure the activated species in plasmas, since OES does not require special laser equipment which is expensive.

Relative densities of species can be measured by using the actinometric OES (AOES) method in reactive plasmas [71]. Using the AOES, the detection of fluorine (F) atoms has been made with reliability in the etching plasma processing. The validity of AOES has been investigated extensively by using the established measurement method for F atom density [72-77].

The hydrogen (H) atom densities have been derived from OES using two line Balmer lines (BOES) where the emission intensities of Balmer α (H_α 656.3 nm) and Balmer β (H_β 486.1 nm) are compared [78]. This method is based on the fact that the upper level of Balmer lines is populated both by electron impact on the ground-state atoms and ground-state molecules. For this method, the availability of reliable cross-sections of direct excitation and dissociative excitation of two lines are very important. In general, however, the knowledge of the cross-sections is insufficient and also is necessary to estimate the electron energy distribution function (EEDF) close to threshold accurately.

Optical absorption spectroscopy is a powerful tool to obtain the information about the absolute density of radicals directly in the plasmas. This technique does not disturb the plasma and does not need the procedure of calibration for estimating the absolute density. The Si atom densities in the parallel-plate RF and ECR SiH_4 plasmas were measured by ultraviolet absorption spectroscopy (UVAS) using a incoherent hollow cathode lamp, which is a very compact light source [79,80]. Hiramatsu et al. have measured Si atom densities in the parallel-plate SiH_4 plasma employing UVAS with a ring dye laser which has a narrow linewidth [81].

Tachibana and Kamisugi have developed the vacuum ultraviolet laser absorption spectroscopy (VUVLAS) for measuring the F atoms in the plasma [82], in which coherent VUV emission at 95-96 nm has been obtained by two-photon resonance four wave frequency mixing technique using Xe gas. This method is very reliable and extended to the measurement of the densities of C atoms [83], H atoms, N atoms, and O atoms [84] in the ground state. Umemoto et al. have measured H atoms in Cat-CVD with SiH_4/H_2 by VUVLAS with the phase-match third harmonic generation technique

[85]. These methods basically need a specialized skill to operate the dye laser system and sophisticated techniques such as frequency mixing and phase-matching, etc.

The VUV absorption spectroscopy (VUVAS) using resonance fluorescence emission in the VUV region has been proposed to measure F atom densities in the etching plasmas [86]. However, the self-absorption exists generally in the light source and it causes the distortion of line shape of the probe emission considerably from Gaussian profile. Therefore, this technique has some issues to be solved in measuring the absolute densities of F atoms in the plasma.

Takashima et al. have developed a reliable measurement technique for atomic radicals in the reactive plasmas employing the VUVAS with a high pressure microdischarge hollow cathode lamp (MHCL). This emission line profile does not involve a large Doppler broadening due to excited atomic radicals and the distortion of the line shape does not occur. Moreover, this measurement system is very compact. This technique is successfully applied to the measurement of the absolute density of H atoms in reactive plasmas employing SiH_4 and CH_4, and extended to the measurements of the absolute densities of O, C, and N atoms with various kind of plasma processing [87-94].

Two-photon absorption laser induced fluorescence (TALIF) technique has been applied to the measurement of H atoms in H_2 plasmas [95-98], O atom in O_2 plasmas [99-101] and O_2/CF_4 plasmas [102]. This technique has potentially a high temporal and spatial resolution and a wide dynamic range, but the calibration procedure for obtaining the absolute scale requires many assumptions. Moreover, the laser used in TALIF sometimes causes the dissociation of feed gases and other species in the plasma.

Table 1.3 Various techniques for measurement of atomic radicals.

Measurement methods	Measured Radicals	Gases	Reference
Optical emission spectroscopy (OES)			
Actinometric optical emission spectroscopy (AOES)	F	CF_4	[71]
OES due to two Balmer lines (BOES)	H	H_2	[78]
Otpical absorption spectroscopy (OAS) with incoherent ligh sources			
Ultraviolet absorption spectroscopy (UVAS)	Si	SiH_4	[79~81]
Vacuum ultraviolet absorption spectroscopy (VUVAS)	H	H_2, SiH_4, CH_4	[87~89]
	O	O_2	[93,94]
	N	N_2	[92]
	F	C_4F_8, CF_4	[86]
Vacuum ultaviolet laser absorption spectroscopy (VUVLAS)	H	H_2, SiH_4	[85]
	O	O_2	[84]
	N	N_2	[84]
	F	CHF_3, CF_4, C_2F_6	[82]
	C	CHF_3, CF_4, C_2F_6	[83]
Two-photon absorption laser induced fluorescence (TALIF)	H	H_2	[95~98]
	O	O_2, CF_4/O_2	[99~102]

1.2.2 Measurement for molecular radicals

Table 1.4 shows the measurement techniques of molecular radicals. Molecular radicals such as CF_x (x=1~3), SiH_x (x=1~3), and CH_x (x=1~3) are so important that their behaviors and their gas phase kinetics should be measured and clarified for controlling the plasma processing. Infrared diode laser absorption spectroscopy (IRLAS) has been applied to the measurement of the absolute density of radicals in reactive plasmas. In the case of measurement of rotation-vibration transitions in the ground state with IRLAS, the sensitivity of the absorption is relatively low compared with that of other methods detecting the electronic transitions. However, neutral non-emissive radicals in the electronic ground state such as CF_3, SiH_3, and CH_3, which

had never been measured in the past by various optical measurement methods, were successfully measured by IRLAS. CF_x (x=1~3) radical in C_2F_6 plasmas [106], CHF_3 plasmas [107,108], and C_4F_8 plasmas [109,110], SiH and SiH_3 in SiH_4 plasmas [111,112], and CH_3 in CH_4 and CH_3OH plasmas [113,114] have been reported previously. Intracavity laser absorption spectroscopy (ICLAS) was developed where the plasma was placed inside the laser resonator for getting a long absorption length and low-density SiH_2 radicals [115].

Recently, to improve the detection limit of radicals in the plasma, the cavity ring down spectroscopy (CRDS) has been applied to the measurement of the molecular radical densities in reactive plasmas with high sensitivity [116,117]. It realized the increase of the sensitivity of detection with pulse light sources. The sensitivity was significantly greater than those with the conventional absorption measurements employing the continuous light sources. This technique led to the development of the novel measurement systems such as phase-shift CRDS [118], Fourier transform CRDS [119], and cavity enhanced magnetic rotation spectroscopy [120] and extended to the detection of a lot of important radicals such as SiH and CH radicals in reactive plasmas.

LIF has been frequently applied to the measurement of spatial distribution of radicals in reactive plasmas. Surface reaction rates and sticking probabilities have been also measured by using the LIF [121]. CF and CF_2 radicals in C_2F_6, C_4F_8, and CHF_3 plasmas [122-126], SiH and SiH_2 radicals in SiH_4 plasmas [127,128], SiF and SiF_2 radicals in SiF_4 plasmas [129-131], and CH radical in CH_4 plasmas [132] have been reported previously.

Appearance mass spectroscopy (AMS) was developed for measuring the absolute density of several kinds of radicals such as CF_x (x=1~3) [133], and CH_x

(x=1~3) [134] but had experimental difficulties in reliable measurement of radicals of relatively high sticking coefficient such as SiH_x (x=1~3) [134].

Table 1.4 Various techniques for measurement of molecular radicals.

Measurement methods	Measured Radicals	Gases	Reference
Otpical absorption spectroscopy (OAS) with incoherent ligh sources			
Ultraviolet absorption spectroscopy (UVAS)	CH_3	CH_4/H_2	[103]
	CF, CF_2	$C_4F_8/C_2H_2F_2$/Ar	[104, 105]
Infrared diode laser absorption spectroscopy (IRLAS)	CF, CF_2, CF_3	C_2F_6, CHF_3, C_4F_8	[106~110]
	SiH, SiH_3	SiH_4	[111, 112]
	CH_3	CH_4, CH_3OH	[113, 114]
Intracavity laser absorption spectroscopy (ICLAS)	SiH_2	SiH_4	[115]
Cavity ring down spectroscopy (CRDS)	SiH_3, SiH, CH_3, CH, etc	SiH_4, CH_4	[116~120]
Laser-induced fluorescence spectroscopy (LIF)	CF, CF_2	C_2F_6, C_4F_8, CHF_3	[122~126]
	SiH, SiH_2	SiH_4	[127, 128]
	SiF_2	SiF_4	[129~131]
	CH	CH_4	[132]
Appearance mass spectroscopy (AMS)	CF, CF_2, CF_3	CF_4	[133]
	CH, CH_2, CH_3	CH_4	[134]

1.2.3 Measurement for radical temperatures

Various diagnostics techniques have been applied to the measurement of temperature of species, as shown in Table 1.5. The measured radical temperatures generally mean translational one. However, molecular radicals have translational, rotational, vibrational, and excitation temperatures. In the previous study, Doppler broadening of absorption [138-143], or fluorescence [144-147] were investigated to obtain the translational temperatures of radicals. On the other hand, analyses of rotational and vibrational spectra of absorption [104,148-154], emission [155-164], or fluorescence [162] were carried out to investigate the rotational and vibrational

temperatures. Popular measurement technique for obtaining the radical temperature is the analysis of the rotational and vibrational band shapes by using OES and Fourier transform infrared spectroscopy. The translational temperature of radical is a very important factor to obtain the information of surface reaction of the radicals on the substrate. The chemisorbed flux of radicals incident on the substrate is defined as

$$\Gamma_{ads} = s\Gamma, \tag{1.4}$$

where s and Γ are the sticking coefficient and the radical flux incident on the substrate, respectively. The flux of radicals Γ incident on the solid surface is given by

$$\Gamma = \frac{1}{4} n \sqrt{\frac{8kT}{\pi m}}, \tag{1.5}$$

where n, m, and k are the absolute density of radical, the mass, and Boltzmann constant, respectively. T is the translational temperature of the radical. Therefore, the translational temperature of radicals is a key parameter to determine the process feature in the plasma process, and the measurement of Doppler broadening by using the coherent light source is the most powerful technique to measure the translational temperature of selected species directly.

Table 1.5 Various techniques for measurement of radical temperatures.

Method		Species	Reference
Rotational and vibrational spectra	Absorption	CF, CF_2, CF_3, CF_4	[104, 148~151]
		SiH_3	[152, 153]
		N_2O	[154]
	Optical emission	N_2	[155~158]
		N_2^+	[158, 159]
		C_2, CO, SiF, CN, CF	[160, 161]
		CCl	[162]
		SiH	[163]
		CH	[164]
	Fluorescence	CCl	[162]
Doppler broadening	Absorption	CF, CF_2, CF_4	[139-140]
		Si	[141~143]
		H	[138]
	Fluorescence	Ar^+,	[144]
		Fe	[145]
		SiH_2	[146]
		CF	[147]

1.3 Purpose and composition of this thesis

The industrial application of plasma includes many processes such as deposition and etching technologies for semiconductor processing, surface modification abatement of poisonous substance, etc. In these plasma application processes, the plasma generation and the control for each process are needed and it is important to understand the reaction process in plasma and on the surface. The development of the plasma generation and control technology based on fundamental knowledge the plasma science, the plasma diagnostics technology and a new plasma application process is demanded and advanced. The purpose of the research work presented in this thesis is to

clarify the mechanism of high etching performance by the dc bias superposed on the dual frequency capacitively coupled plasma (CCP), which is proposed as advanced plasma processing for ULSI fabrication; it is also to clarify the physical properties of plasma generated by YAG laser in liquid which is noted as the new generation laser application.

In Chapter 2, diagnostics techniques and analysis methods are presented that are absolutely necessary to measure the plasma parameters and the process properties. In this chapter, the theories of plasma absorption probe (PAP), laser Thomson scattering, Mach-Zender interferometer, laser induced fluorescence (LIF), vacuum ultra violet absorption spectroscopy (VUVAS) and optical emission spectroscopy (OES), which are mainly used for investigating plasma characteristics, were described. Also introduced are X-ray photoelectron spectroscopy (XPS) and spectroscopic ellipsometer used for the analysis of analyzing film properties.

In Chapter 3, 4 and 5, the author has investigated dual frequency CCP with negative dc bias superposed on the VHF power on the upper electrode. The dc superposed dual frequency CCP has been proposed as an advanced plasma processing technology for achieving high etching performances in ULSI fabrication.

In chapter 3, the effect of dc bias superposition to dual frequency CCP was estimated by measuring the plasma parameters such as electron density and the electron energy distribution function (EEDF) using laser Thomson scattering. Measurement of the plasma parameters is important for understanding the physical processes and laser Thomson scattering is considered to be the most reliable method to measure the plasma parameters in reactive plasmas.

In chapter 4, high accuracy processing, that is, a high selectivity etching of

SiOCH films over SiC films was actually realized in negative dc superposed dual frequency CCP c-C_4F_8/N_2/Ar plasma. The mechanism of high selectivity etching by dc superposed plasma was clarified on the basis of the results obtained using PAP, LIF and VUVAS.

In chapter 5, the spatial distribution of plasma parameters such as plasma density, gaseous temperature, and absolute CF and CF_2 radical densities were investigated in the dual frequency CCP with 60 MHz VHF superposed negative dc bias. The uniformity of electron density was obtained by applying a dc bias. It was noteworthy that the spatial distributions of CF and CF_2 densities were also uniform in correlation with the uniform electron-density distribution.

In chapter 6, the physical properties of plasma generated by YAG laser in liquid, which is noted as a new generation laser application, were clarified. The physical properties of plasma in liquid were estimated by using Mach-Zender interferometer and OES.

Finally, the results in the present study are summarized and future scope is described in Chapter 7.

References

[1] R. H. Havenmann and J. A. Hutchby, *Proceeding of the IEEE*, **89**, 586 (2001).

[2] R. H. Dennard, F. H. Gaensslen, H-N. V. L. Rideout, E. Bassous, and A. R. LeBlanc, IEEE J. Solid-State Circuits **SC-9**, 256 (1976).

[3] R. Kumar and G. Hinton, "A Family of 45nm IA Processors," ISSCC Dig. Tech. Papers, Paper 3.2, Feb. 2009.

[4] S. P. Sun, S. P. Murarka, and C. J. Lee, J. Vac. Sci. Technol. B **6**, 1963 (1988).

[5] M. J. Shapiro, S. V. Nguyen, T. Matsuda, and D. Dobuzinsky, Thin Solid Film **270**, 503 (1995).

[6] T. Usami, K. Shimokawa, and M. Yoshimaru, Jpn. J. Appl. Phys. **33**, 408 (1994).

[7] W. W. Lee, and P. S. Ho, Mater. Res. Soc. Bull. **22**, 19 (1997).

[8] S. Purushothaman, et al. Tech. Digest IEDM 23.2.1 (2001).

[9] R. D. Goldblatt, et al. Tech Dig. IEDM 261 (2000)

[10] S. Ogawa, et al. Proc. of the 2002 IITC, vol. **10.2**, 220 (2002).

[11] T. Jacobs, et al. Proc. of the 2002 IITC, vol. **11.2**, 236 (2002).

[12] T. Homma, R. Yamaguchi, and Y. Murao, J. Electrochem. Soc. **140**, 687 (1993).

[13] Y. H. Kim, M. S. Hwang, H. J. Kim, J. Y. Kim, and Y. Lee, J. Appl. Phys. **90**, 3367 (2001).

[14] W. S. Yoo and R. Swope, Jpn. J. Appl. Phys. **33**, 408 (1994).

[15] H. Kitoh, M. Muroyam, M. Sasaki, M. Iwasawa, and H. Kimura, Jpn. J. Appl. Phys. **35**, 1464 (1996).

[16] M. K. Bhan, J. Huang, and D. Cheung, Thin Solid Films **308-309**, 507 (1997).

[17] H. J. Lee, C. L. Soles, D. W. Liu, B. J. Bauer, E. K. Lin, W. L. Wu, and A. Grill, J. Appl. Phys. **95**, 2355 (2004).

[18] Y. Morikawa, N. Mizutani, M. Ozawa, T. Hayashi, W. Chen, and T. Uchida, J. Vac. Sci. Technol. B **21**, 1344 (2003).

[19] X. Hua, X. Wang, D. Fuentevilla, G. S. Oehrlein, F. G. Celii, and K. H. R. Kirmse, J. Vac. Sci. Technol. A **21**, 1708 (2003).

[20] N. Posseme, T. Chevolleau, O. Joubert, L. Vallier, and P. Mangiagalli, J. Vac. Sci. Technol. B **21**, 2432 (2003).

[21] A. T. Kohl, R. Mimna, R. Shick, L. Rhodes, Z. L. Wang, and P. A. Kohl, Electrochem. Solid-State Lett. **2**, 77 (1999).

[22] R. Kanamura, Y. Ohoka, M. Fukasawa, K. Tabuchi, K. Nagahata, S. Shibuki, M. Muramatsu, H. Miyajima, T. Usui, A. Kajita, H. Shibata, and S. Kadomura, Dig. Symp. VLSI Technology, 35 (2003).

[23] L. M. Han, R. B. Timmons, W. W. Lee, Y. Chen, and Z. Hu, J. Appl. Phys. **84**, 439 (1998).

[24] Y. Hayashi, Oyo Buturi, **74**, No.9 1178 (2005).

[25] T. Namura, H. Okada, Y. Naitoh, Y. Todokoro, and M. Inoue, Jpn. J. Appl. Phys. **29**, 2251 (1990).

[26] D. L. Flamm, V. M. Donnelly, and D. E. Ibbotson, J. Vac. Sci. Technol. B **1**, 23 (1983).

[27] G. S. Oehrlein, Y. Zhang, D. Vender, M. Haverlag, J. Vac. Sci. Technol. A **12**, 323 (1994).

[28] T. Sikola, D. G. Armour, and A. V. Berg, J. Vac. Sci. Technol. A **14**, 3156 (1996).

[29] T. Shirafugi, W. W. Stoffels, H. Moriguchi, and K. Tachibana, J. Vac. Sci. Technol. A **15**, 209 (1997).

[30] T. Akimoto, S. Furuoya, K. Harasima, and E. Ikawa, Jpn. J. Appl. Phys. **33**, 2151

(1994).

[31] Ch. Cardinaud and G. Turban, Appl. Surface Sci. **45**, 109 (1990).

[32] S. Fang. C. Chiang, D. Fraser, B. Lee, P. Keswick, M. Chang, and K. Fung, J. Vac. Sci. Technol. A **14**, 1092 (1996).

[33] G. E. Potter, G. H. Morrison, P. K. Charvat, and A. L. Ruoff, J. Vac. Sci. Technol. B **10**, 2398 (1992).

[34] T. Akimoto, H. Nanbu, and E. Ikawa, J. Vac. Sci. Technol. B **13**, 2390 (1995).

[35] K. H. R. Kirmse, A. E. Wendt, S. B. Disch, J. Z. Wu, I. C. Abraham, J. A. Meyer, R. A. Breun, and R. C. Woods, J. Vac. Sci. Technol. A **13**, 877 (1995).

[36] H. Doh, J. Kim, S. Lee, and K. Whang, J. Vac. Sci. Technol. A **14**, 2827 (1996).

[37] K. Takahashi, M. Hori, and T. Goto, J. Vac. Sci. Technol. A **14**, 2004 (1996).

[38] R. C. Reid, J. M. Prausnitz, and T. K. Sherwood, The Properties of Gases and Liquids (McGraw-Hill, New York, 1977).

[39] B. Chapmann, Glow Discharge Processes, Sputtering and Plasma Etching (Wiley, New York, 1980).

[40] S. B. Kim, D. G. Choi, T. E. Hong, T. S. Park, D. S. Kim, Y. W. Song, and C. I. Kim, J. Vac. Sci. Technol. A **23**, 953 (2005).

[41] A. Koshiishi, Y. Araki, S. Himori and T. Iijima, Jpn. J. Appl. Phys. **40**, 6613 (2001).

[42] S. Yun and G. R. Tynan, J. Appl. Phys. **89**, 911 (2001).

[43] T. Nozawa and T. Kinoshita, Jpn. J. Appl. Phys. **34**, 2107 (1995).

[44] T. Kinoshita, M. Hane, and J. P. Mavittee, J. Vac. Sci. Technol. B **14**, 560 (1996).

[45] H. Ootera, Jpn. J. Appl. Phys. **33**, 6109 (1993).

[46] S. Samukawa and T. Mukai, J. Vac. Sci. Technol. B **18**, 166 (2000).

[47] S. V. Nguyen, D. Dobuzinski, S. R. Stiffler and G. Chrisman, J. Electrochem. Soc.

138, 1112 (1991).

[48] T. J. Dalton, J. C. Arnold, H. H. Sawin, S. Swan, and D. Corliss, J. Electrochem. Soc. **140**, 2395 (1993).

[49] A. C. Westerheim, A. H. Labum, J. H. Dublash, J. C. Arnold, H. H. Sawin, and V. Y. Wang, J. Vac. Sci. Technol. A **13**, 853 (1995).

[50] J. C. Arnold and H. H. Sawin, J. Appl. Phys. **70**, 5314 (1991).

[51] M. Schaeplens and G. S. Oehrlein, Appl. Phys. Lett. **72**, 1293 (1998).

[52] G. Mannaert, M. R. Baklanov, Q. T. Le, Y. Travaly, W. Boullart, S. Vanhaelemeersch, and A. M. Jonas, J. Vac. Sci. Technol. B **23**, 2198 (2005).

[53] F. Itoh, K. Hijioka, T. Takeuchi, and Y. Hayashi, Proc. Advanced Metallization Conf., San Diego, 381 (2004).

[54] M. Shimada, J. Shimanuki, N. Ohtsuka, A. Furuya, Y. Inoue, and S. Ogawa, Proc. IEEE Int. Interconnect Technology Conf., San Francisco, 178 (2004).

[55] N. Posseme, T. Chevolleau, O. Joubert, L. Vallier, and P. Mangiagalli, J. Vac. Sci. Technol. B **21**, 2432 (2003).

[56] T. Tatsumi, K. Urata, K. Nagahata, T. Saitoh, Y. Nogami, and K. Shinohara, J. Vac. Sci. Technol. A **23**, 938 (2005).

[57] H. Nagai, Y. Maeda, M. Hiramatsu, M. Hori, and T. Goto, Jpn. J. Appl. Phys. **42**, L326 (2003).

[58] S.-B. Wang and A. E. Wendt, J. Appl. Phys. **88**, 643 (2000).

[59] T. Novikova, B. Kalache, P. Bulkin, K. Hassouni, W. Morscheidt, and P. Roca i Cabarrocas, J. Appl. Phys. **93**, 3198 (2003).

[60] T. Kitajima, Y. Takeo, Z. Lj. Petrovic, and T. Makabe, Appl. Phys. Lett. **77**, 489 (2000).

[61] K. Kohler. J. W. Coburn, D. E. Horne, E. Kay, and J. H. Keller, J. Appl. Phys. **57**, 59 (1985).

[62] E. Kawamura, M. A. Lieberman, A. J. Lichtenberg, and E. A. Hudson, J. Vac. Sci. Technol. A **25**, 1456 (2007).

[63] E. Kawamura, A. J. Lichtenberg, and M. A. Lieberman, Plasma Sources Sci. Technol. **17**, 045002 (2008).

[64] K. Denpoh and P. L. G. Ventzek, J. Vac. Sci. Technol. A **26**, 1415 (2008).

[66] P. L. G. Ventzek, and K. Denpoh, J. Vac. Sci. Technol. A **27**, 287 (2009).

[67] L. Xu, L. Chen, M. Funk, A. Ranjan, M. Hummel, R. Bravenec, R. Sundarajan, D. J. Economou, and V. M. Donnelly, Appl. Phys. Lett. **93**, 261502 (2008).

[68] M. Nagai, M. Hori, and T. Goto, Jpn. J. Appl. Phys. **43**, L501 (2004).

[69] M. Wang, and M. J. Kushner, J. Appl. Phys. **107**, 023308 (2010).

[70] M. Wang, and M. J. Kushner, J. Appl. Phys. **107**, 023309 (2010).

[71] J. W. Coburn, M. Chen, J. Appl. Phys. **51**, 3134 (1980).

[72] K. Sasaki, Y. Kawai, K. Kadota, Appl. Phys. Lett. **70**, 1375 (1997).

[73] P. D. Hanish, J. W. Grizzle, M. D. Giles, F. L. Terry Jr., J. Vac. Sci. Technol. A 13, 1802 (1995).

[74] J. Jeng, J. Ding, J. W. Taylor, N. Hershkowitz, Plasma Sources Sci. Technol. 3, 154 (1995).

[75] V. M. Donnelly, W. C. Dautremont-Smith, D. L. Flamm, D. J. Werder, J. Appl. Phys. 55, 242 (1984).

[76] R. A. Gottscho, V. M. Donnelly, J. Appl. Phys. 56, 245 (1984).

[77] Y. Kawai, K. Sasaki, K. Kadota, Jpn. J. Appl. Phys. 36, L2161 (1997).

[78] V. S. der Gathen, H. F. Dobele, Plasma Chem. Plasma Process. 14, 87 (1994).

[79] M. Sakakibara, M. Hiramatsu, T. Goto, J. Appl. Phys. 69, 3467 (1991).

[80] Y. Yamamoto, M. Hori, T. Goto, M. Hiramatsu, J. Vac. Sci. Technol. A 14, 1999 (1996).

[81] M. Hiramatsu, M. Shirafuji, Y. Matsui, Jpn. J. Appl. Phys. 32, 5721 (1993).

[82] K. Tachibana, H. Kamisugi, Appl. Phys. Lett. 74, 573 (1999).

[83] N. Tanaka, K. Tachibana, J. Appl. Phys. **92**, 5684 (2002).

[84] K. Tachibana, Plasma Sources Sci. Technol. **11**, A166 (2002).

[85] H. Umemoto, K. ohara, D. Morita, Y. Nozaki, A. Matsuda, and H. Matsumura, J. Appl. Phys. **91**, 1650 (2002).

[86] K. Sasaki, Y. Kawai, K. Kadota, Appl. Phys. Lett **70**, 1375 (1997).

[87] S. Takashima, M. Hori, T. Goto, A. Kono, M. Ito, K. Yoneda, Appl. Phys. Lett. **75**, 3929 (1999).

[88] S. Takashima, M. Hori, T. Goto, K. Yoneda, J. Appl. Phys. **89**, 4727 (2001).

[89] S. Takashima, M. Hori, T. Goto, A. Kono, K. Yoneda, J. Appl. Phys. **90**, 5497 (2001).

[90] H. Ito, K. Teii. M. Ishikawa, M. Ito, M. Hori, T. Takeo, T. Kato, T. Goto, Jpn. J. Appl. Phys. **38**, 4504 (1999).

[91] S. Takashima, S. Arai, M. Hori, T. Goto, A. Kono, K. Yoneda, J. Vac. Sci. Techonl. A **19**, 599 (2001).

[92] S. Tada, S. Takashima, M. Ito, M. Hori, T. Goto, J. Appl. Phys. **88**, 1756 (2000).

[93] H. Nagai, M. Hiramatsu, M. Hori, and T. Goto, Rev. Sci. Instrum. **74**, 3453 (2003).

[94] J. P. Booth, O. Joubert, J. Pelletier, and N. Sadeghi, J. Appl. Phys. **69**, 618 (1991).

[95] K. Tachibana, Jpn. J. Appl. Phys. **33**, 4329 (1994).

[96] J. Jolly and J. P. Booth, J. Appl. Phys. **97**, 103305 (2005).

[97] L. Chérigier, U. Czarnetzki, D. Luggenhölscher, V. S. Gathen, and H. F. Döbele, J. Appl. Phys. **85**, 696 (1999).

[98] B. L. Preppernau, and T. A. Miller, J. Vac. Sci. Technol. A **8**, 1673 (1990).

[99] E. J. H. Collart, J. A. G. Baggerman, and R. J. Visser, J. Appl. Phys. **78**, 47 (1995).

[100] A. D. Tserepi and T. A. Miller, J. Appl. Phys. **77**, 505 (1995).

[101] J. Matsushita, K. Sasaki, and K. Kadota, Jpn. J. Appl. Phys. **36**, 4747 (1997).

[102] R. E. Walkup, K. L. Saenger, and G. S. Selwyn, J. Chem. Phys. **84**, 2668 (1986).

[103] B. A. Cruden and M. Meyyappan, J. Appl. Phys. **97**, 084311 (2005).

[104] J. Luque, E. A. Hudson, and J. P. Booth, J. Chem. Phys. **118**, 622 (2003).

[105] N. Bulcount, J. P. Booth, E. A. Hudson, J. Luque, D. K. W. Mok, E. P. Lee, F. T. Chau, and J. M. Dyke, J. Chem. Phys. **120**, 9499 (2004).

[106] W. L. Perry, K. Waters, M. Barela, and H. M. Anderson, J. Vac. Sci. Technol. A **19**, 2272 (2001).

[107] K. Miyata, M. Hori, and T. Goto, J. Vac. Sci. Technol. A **15**, 568 (1997).

[108] M. E. Littau, M. J. Sowa, and J. L. Cecchi, J. Vac. Sci. Technol. A **20**, 1603 (2002).

[109] K. Miyata, M. Hori, and T. Goto, Jpn. J. Appl. Phys. **36**, 5340 (1997).

[110] K. Miyata, K. Takahashi, S. Kishimoto, M. Hori, and T. Goto, Jpn. J. Appl. Phys. **34**, L444 (1995).

[111] N. Itabashi, K. Kato, N. Nishiwaki, T. Goto, Y. Yamada, and E. Hirota, Jpn. J. Appl. Phys. **27**, L1565 (1988).

[112] Y. Yamamoto, H. Nomura, T. Tanaka, M. Hiramatsu, M. Hori, and T. Goto, Jpn. J. Appl. Phys. **33**, 4320 (1994).

[113] S. Naito, N. Ito, T. Hattori, and T. Goto, Jpn, J, Appl. Phys. **32**, 5721 (1993).

[114] M. Ikeda, K. Aiso, M. Hori, and T. Goto, Jpn. J. Appl. Phys. **34**, 3273 (1995).

[115] K. Tachibana, T. Shirafuji, Y. Matsui, Jpn. J. Appl. Phys. **31**, 2588 (1992).

[116] A. O'Keefe, D. A. G. Deacon, Rev. Sci. Instrum. **59**, 2544 (1988).

[117] M. G. H. Boogaarts, P. J. Bocker, W. M. M. Kessels, D. C. Schram, M. C. M. van der Sanden, Chem. Phys. Lett. **326**, 400 (2000).

[118] R. Engeln, G. V. Helden, G. Berden, G. Meijer, Phys. Lett. **262**, 105 (1996).

[119] R. Engeln, G. Meijer, Rev. Sci. Instrum. **67**, 2708 (1996).

[120] R. Engeln, G. Berden, R. Peeters, G. Meijer, Rev. Sci. Instrum. **69**, 3763 (1998).

[121] N. M. Mackie, V. A. Venturo, and E. R. Fisher, J. Phys. B **101**, 9425 (1997).

[122] G. A. Hebner, J. Appl. Phys. **89**, 900 (2001).

[123] P. J. Hargis, Jr. and M. J. Kushner, Appl. Phys. Lett. **40**, 779 (1982).

[124] K. Kinomiya, K. Suzuki, S. Nishimatsu, and O. Okada, J. Vac. Sci. Technol. A **4**, 1791 (1986).

[125] J. O. Booth, G. Hancock, N. D. Perry, and M. J. Toogood, J. Appl. Phys. **66**, 5251 (1989).

[126] C. Suzuki, K. Sasaki, and K. Kadota, J. Appl. Phys. **82**, 5321 (1997).

[127] A. Kono, N, Koiske, K. Okuda, and T. Goto, Jpn. J. Appl. Phys. **32**, L543 (1993).

[128] H. Nomura, K. Akimoto, A. Kono, and T. Goto, J. Phys. D **28**, 1977 (1995).

[129] C. W. Watson and K. G. McKendrick, Chem. Phys. **187**, 87 (1994).

[130] A. C. Stanton, A. Freedman, J. Worthhoudt, and P. P. Gasper, Chem. Phys. Lett. **122**, 190 (1985).

[131] M. Nakamura, M. Hori, T. Goto, M. Ito, and N. Ishii, Jpn. J. Appl. Phys. **40**, 4730 (2001).

[132] K. Tachibana, T. Mukai, A. Yuuki, Y. Matsui, and H. Harima, Jpn. J. Appl. Phys.

29, 2156 (1990).

[133] Y. Hikosaka, M. Nakamura, H. Sugai, Jpn. J. Appl. Phys. **33**, 2157 (1994).

[134] H. Sugai, H. Toyota, J. Vac. Sci. Technol. A **10**, 1193 (1992).

[135] W. W. Stoffel, E. Stoffels, K. Tacihibana, Rev. Sci. Instrum. **69**, 116 (1998).

[136] K. Teii, M. Hori, M. Ito, T. Goto, J. Vac. Sci. Technol. A **18**, 1 (2000).

[137] M. Nakamura, Y. Hirano, Y. Shiokawa, M. Takayanagi, M. Nakata, J. Vac. Sci. Technol. A **24**, 385 (2006).

[138] D. Wagner, B. Dikmen, and H. F. Döbele, Rev. Sci. Instrum. **67**, 1800 (1996).

[139] M. Nakamura, M. Hori, T. Goto, M. Ito, and N. Ishii, J. Appl. Phys. **90**, 580 (2001).

[140] M. Haverlag, E. Stoffels, W. W. Stoffels, G. M. W. Kroesen, and F. De Hoog, J. Vac. Sci. Technol A **14**, 380 (1996).

[141] T. Ohta, M. Hori, T. Ishida, T. Goto, M. Ito, S. Kawakami, and N. Ishii, Jpn. J. Appl. Phys. **42**, L1532 (2003).

[142] M. Hiramatsu, M. Sakakibara, M. Mushiga, and T. Goto, Meas. Sci. Technol. **2**, 1017 (1991).

[143] T. Tanaka, M. Hiramatsu, M. Nawata, A. Kono, and T. Goto, J. Phys. D **27**, 1660 (1994).

[144] G. A. Hebner, J. Appl. Phys. **80**, 2624 (1996).

[145] K. Shibagaki, N. Nafarizal, and K. Sasaki, Jpn. J. Appl. Phys. **98**, 043310 (2005).

[146] A. Kono, S. Hirose, K. Kinoshita, and T. Goto, Jpn. J. Appl. Phys. **37**, 4588 (1998).

[147] H. Abada, P. Chabert, J. P. Booth, J. Robiche, and G. Cartry, J. Appl. Phys. **92**, 4223 (2002).

[148] M. E. Littau, M. J. Sowa, and J. L. Cecchi, J. Vac. Sci. Technol. A **20**, 1603 (2002).

[149] M. Haverlag, F. J. de Hogg, and G. M. W. Kroesen, J. Vac. Sci. Technol. A **9**, 327 (1991).

[150] M. Magane, N. Itabashi, N. Nishiwaki, T. Goto, C. Yamada, and E. Hirota, Jpn. J. Appl. Phys. **29**, L829 (1990).

[151] K. Maruyama, A. Sakai, and T. Goto, J. Phys. D **26**, 199 (1993).

[152] N. Itabashi, K. Kato, N. Nishiwaki, T. Goto, C. Yamada, and E. Hirota, Jpn. J. Appl. Phys. **28**, L325 (1989).

[153] N. Itabashi, N. Nishiwaki, M. Magane, S. Naito, T. Goto, A. Matsuda, C. Yamada, and E. Hirota, Jpn. J. Appl. Phys. **29**, L505 (1990).

[154] T. A. Cieiand and D. W. Hess, J. Appl. Phys. **64**, 1068 (1988).

[155] V. M. Donnely and M. V. Malyshev, Appl. Phys. Lett. **77**, 2467 (2000).

[156] R. A. Potter and W. R. Harshbarger, J. Electrochem. Soc. **126**, 460 (1979).

[157] E. M. van Veldhuizen, T. H. J. Bisschops, E. J. W. van Vliembergen, and H. M. C. van Wolput, J. Vac. Sci. Technol. A **3**, 2205 (1985).

[158] A. Chelouah, E. Marode, G. Hartmann, and S. Achat, J. Phys. D. **27**, 940 (1994).

[159] H. H. Brömer and F. Spieweck, Z. Phys. **184**, 481 (1965).

[160] B. A. Cruden, M. V. V. S. Rao, S. P. Sharma, and M. Meyyappan, J. Appl. Phys. **91**, 8955 (2002).

[161] M. Oshima, Jpn. J. Appl. Phys. **17**, 1157 (1978).

[162] G. P. Davis and R. A. Gottscho, J. Appl. Phys. **54**, 3080 (1983).

[163] S. Stamou, D. Mataras, and S. Achat, J. Phys. D: Appl. Phys. **27**, 940 (1994).

[164] J. Luque, M. Kraus, A. Wokaum, K. Haffner, U. Kogelschatz, and B. Eliasson, J.

Appl. Phys. **93**, 4432 (2003).

Chapter 2

Plasma Diagnostics Techniques for Evaluating the Internal Parameters and Film Analysis Methods

2.1 Plasma Absorption Probe (PAP)

Many methods have been used to measure the electron density, but they are usually not suitable for monitoring commercial processes in industrial reactors or even in research reactors. For example, Langmuir probes are usable in rare-gas discharges. In many industrial applications using reactive gases, however, insulating layers are formed on the probes, causing them to fail. In such depositing conditions, a microwave interferometer technique is available; however, it gives us only the line-averaged electron densities. Another useful technique is the plasma oscillation method (POM) [1-4] where a weak electron beam excites electrostatic waves oscillating at the electron plasma frequency. A disadvantage here is the use of a hot filament as the electron beam source: the filament has a short lifetime and induces contamination of heavy metals in plasma reactors.

It is possible to use the PAP in measuring the electron density in a space- and time-resolved manner [5, 6]. The PAP is fully covered with quartz; thus, reactor contamination is minimized and insulating layer deposition on the probe is unimportant. A PAP was constructed from a dielectric tube and a coaxial cable. The coaxial cable was

enclosed by a quartz tube (dielectric constant ε=3.78). This quartz tube probe was inserted through the chamber-wall to the center of the chamber. A 50 Ω semi-rigid coaxial cable of 3 mm outer diameter can be moved in the tube. A 5 mm lead of the center conductor (1 mm diameter) of the cable acts as a monopole antenna for radiating electromagnetic waves, to which a frequency-swept signal of 1 mW is fed from a network analyzer (Agilent E5071C). The network analyzer is conventionally used for measuring rf impedances and the power reflection coefficient which is defined as the ratio of the reflected power to the incident in a frequency range ω/π = 0.1 MHz – 8 GHz. Let the power reflection coefficient without plasma be $\Gamma_0 = \rho_0 \exp(i\theta_0)$, the coefficient with plasma be $\Gamma_p = \rho_p \exp(i\theta_p)$, and their ratio be $\Gamma = \Gamma_p/\Gamma_0$. The network analyzer displays the frequency dependence with the value of $\log|\Gamma| = \log\rho_p - \log\rho_0$, thus subtracting the spurious signals ρ_0.

From the plasma dispersion relationship, the surface wave resonance frequency f_{sw} is proportional to the square-root of the plasma density, n_e. Thus, the plasma density was estimated by the following relation,

$$n_e = 1.24\times10^{10}(1+\varepsilon) f_{SW}^2 \qquad (2.1)$$

where f_{sw} is $\omega_{SW}/2\pi$ in units of GHz. ε is 3.78 because the deposited film on the quartz tube is sufficiently negligibly thin. The proportional constant given here strongly depends on the probe geometric arrangement.

2.2 Laser Thomson Scattering

The Thomson scattering measurement is an optical technique in which the EEDF is derived from the Doppler shift of the laser light scattered by free electron in the plasma [7]; the method has the advantage of being nonintrusive and giving the EEDF straightforwardly.

Thomson spectra give one-dimensional projection velocity distribution functions, in which the projection velocity υ_p is related to the wavelength shift $\Delta\lambda$ as [7]

$$\upsilon_p = \frac{c}{2\sin(\theta/2)}\frac{\Delta\lambda}{\lambda_0} \tag{2.2.1}$$

Here, c is the light velocity, λ_0 the center wavelength, and θ the angle between the incident wave vector $\mathbf{k}_0$ and scattered wave vector $\mathbf{k}_s$; projection is in the direction of $\mathbf{k}_0$- $\mathbf{k}_s$ and θ=90˚. Defining $E_p \equiv m\upsilon_p/2$ (m is the electron mass) and replotting the illustrative spectra in Fig. 2.2.1 with E_p as the horizontal axis, we obtain Fig. 2.2.2. Expect in the part with E_p < 1 eV where the effect of the spatial filter exists (see 2.2.1), the function falls exponentially with increasing E_p. If the EEDF is Maxwellian and the electron temperature is directly obtained from the slope of the decaying part of the plot in Fig. 2.2.2. The electron density was also derived from the comparison of the Thomson scattering intensity with the Raman scattering intensity.

$$N_e = N\frac{S_T}{S_R}\frac{\sigma_R}{\sigma_T} \tag{2.2.2}$$

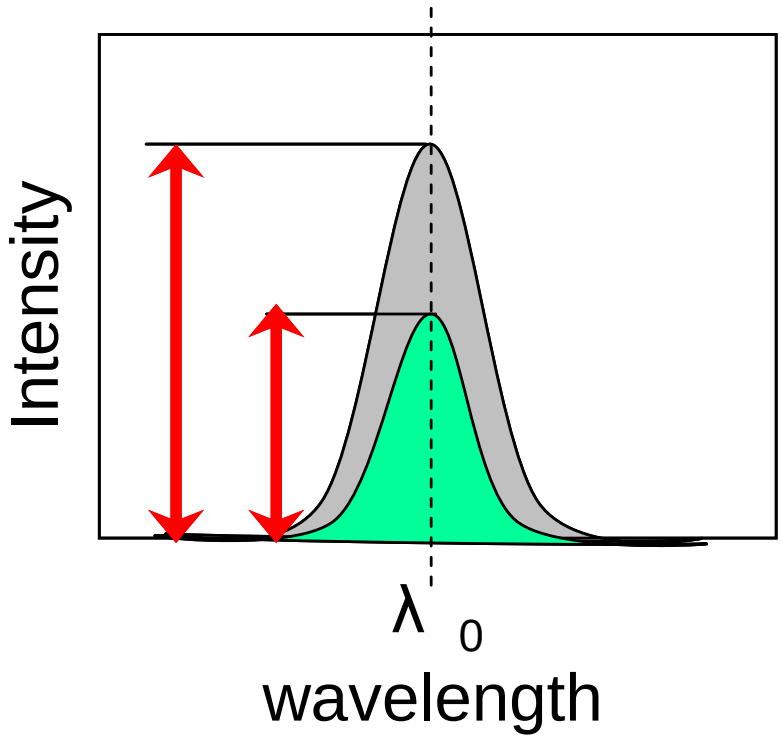

Figure 2.2.1 Thomson spectra.

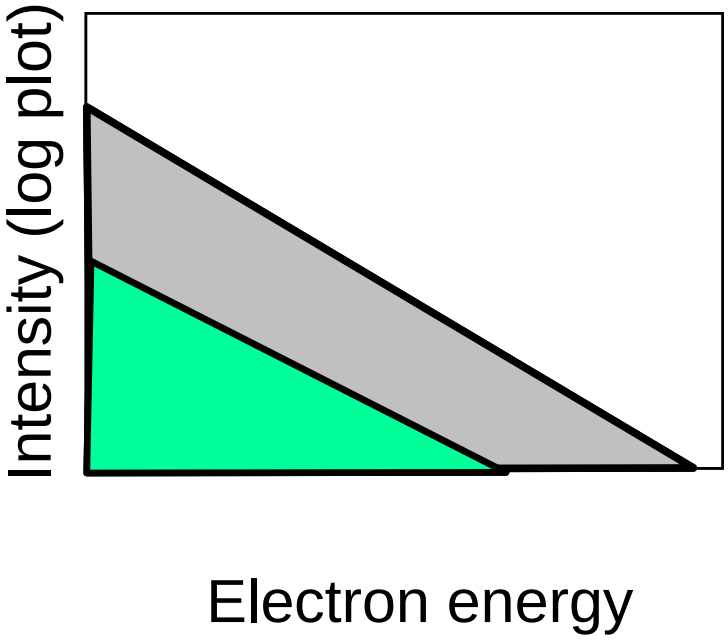

Figure 2.2.2 Thomson scattering intensity as a function of electron energy.

2.2.1 Triple Grating Spectrograph [8]

A spatial triple-grating spectrometer was constructed, which is equipped with a spatial filter for eliminating Rayleigh light, and thereby providing a dispersed Thomson spectrum with the Rayleigh background highly suppressed. Figure 2.2.3 shows the optical arrangement of the spectrometer. The light source for scattering measurements is supposed to be a frequency-doubled Nd:YAG laser and the angles of the three gratings (50 mm×50 mm Shimadzu blazed holographic grating with 1200 grooves/mm, blazed at 500 nm) are adjusted so that the center wavelength is 532 nm.

The first and second gratings are arranged so that the second one cancels the dispersion produced by the first one. In other words, the first grating produces a dispersed Thomson spectrum in the plane where the spatial filter is located, but the second grating combines the spectrum so that all wavelengths pass through the intermediate slit. The Rayleigh light diffracted by the first grating is focused to form the image of the entrance slit and is blocked by the central strip of the spatial filter because of its small Doppler width. The first grating not only diffracts but also scatters the Rayleigh light and the intensity level of this scattered light is considerable. However, though the scattered light pass through the spatial filter, it cannot pass through the intermediate slit. This is because at the wavelength of 532 nm the image of the central strip of the spatial filter covers the opening of the intermediate slit. Thus, in the light passing through the intermediate slit, the Rayleigh component is eliminated to a high degree. The third grating disperses the light again and produces a Thomson spectrum on the photocathode surface of the ICCD camera. In the resulting Thomson spectrum, the Rayleigh interference is reduced to a better level than is attained by single-channel measurements by using a conventional double monochromator.

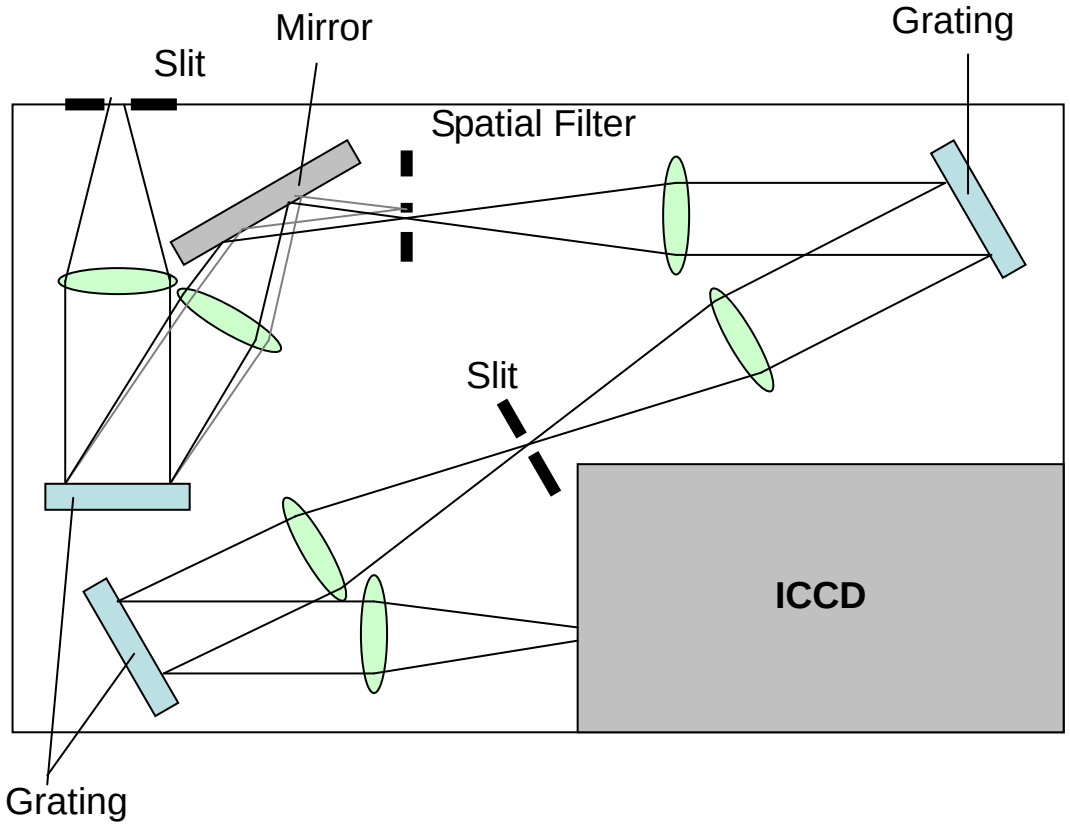

Figure 2.2.3 Optical arrangement of the triple-grating spectrometer with a spatial filter for eliminating Rayleigh interference.

2.3 Mach-Zander Interferometer

The electron density of the laser-produced plasma in liquid is measured using a Mach-Zender interferometer. The Mach-Zender interferometer is a two-beam interferometer in which the beams travel in only one direction. Two outputs are separate from the input. A phase changes are caused by variations of the refractive index in one arm. It is difficult to find out a turning point in the fringe pattern at which the electron density reaches a maximum. It is assumed that the laser pulse is very short compared with measuring time and the electron density decreases monotonically in the measurement time.

The maximum electron density is obtained from the following equation by estimating the maximum fringe number F_L,

$$n_e = 2.18\times10^{15}\frac{F_L}{L\lambda} \tag{2.3.1}$$

where n_e is the electron density, L is the optical length of the probe laser and is the wavelength of the probe laser. The optical length L that is necessary to estimate electron density from the fringe number is calculated from spot diameter of YAG laser and theoretical optical path of Gaussian beam.

2.4 Laser Induced Florescence (LIF)

Atomic or molecular species have quantized energy state. These species absorbs photons which has energy equal to the difference in energies between lower state and upper state, and then pumped to upper state. The species excited by the absorption of the photon emit the light called the fluorescence. A laser radiation which has the wavelength adjusted equal to the difference in energies between lower state and upper state is used. By measuring the LIF intensity, we estimate the concentration of the species in the lower state.

The laser system used for the LIF measurements consisted of a pulsed dye laser (SCANMATE 2E, LAMBDA PHYSIK) pumped with a XeCl laser (Compex 201, LAMBDA PHYSIK), with crystals for output wavelength conversion. For detection of the CF radical, the output of the dye laser was tuned at 232.66 nm wavelength of the transition A $^2\Sigma^+$-X $^2\Pi$ (0,0), and fluorescence at 255.2 nm due to A $^2\Sigma^+$-X $^2\Pi$ (0,3) was observed. In the case of the CF_2 radical, the excitation of 261.7 nm wavelength of the transition A (0,2,0)-X (0,0,0), and fluorescence at 271.0 nm due to A (0,2,0)-X (0,2,0) were used [9]. Since the detected signals overlaps with in the plasma emissions, the

fluorescence signal of the radical was evaluated by subtracting the plasma emission signal. By comparison with the absolute density obtained by single path infrared laser absorption, absolute radical densities were calculated from the fluorescence signal intensity. The fluorescence was detected by using an ICCD. The entrance and exit windows made of quartz for the ultraviolet laser transmission were attached at the chamber wall. The fluorescence was collected with a lens from the direction perpendicular to the laser beam axis and was focused on the entrance slit of a 75-cm spectrometer through the optical fiber.

Figure 2.4.1 shows the diagrams of energy levels and the optical system for LIF measurement. The rate equation of concentration at each energy level in *m*-level (m=3) system is given follow,

$$\frac{dn_2}{dt} = B_{12}\rho n_1 - B_{21}\rho n_2 - \left(A_{21} + A'_{23}\right), \tag{2.4.1}$$

$$\frac{dn'_3}{dt} = A'_{23} n_2, \tag{2.4.2}$$

$$n = n_1 + n_2 + n'_3, \tag{2.4.3}$$

where n_i is concentration in the level i, n is the ground state concentration before excitation by laser, ρ is the energy concentration of laser beam for excitation, and A_{jk} and B_{jk} are the Einstein A and B coefficients for transitions from level j to k, respectively. If intensity of laser beam excitation is sufficiently large, i.e., $\rho(B_{12}+B_{21}) >> (A_{21}+A'_{23})$, approximate solution of Eq. 2.4.1 is given by,

$$n_2(t) = \frac{g_2}{g_1 + g_2} n \exp\left(-\frac{g_2}{g_1 + g_2} A'_{23} t \right), \tag{2.4.4}$$

where g_i is the statistical weight in the level i. As the number of photons radiated per unit time and unit volume is $n_2A'_{23}$, the number of photons detected with is given by,

$$\int A_{2i} n_2(t) \frac{d\Omega}{4\pi} V dt = C \int A'_{23} n_2(t) dt = Cn \,, \tag{2.4.5}$$

$$CA'_{23} = \frac{d\Omega}{4\pi} V A_{2i} \,. \tag{2.4.6}$$

Therefore, detected signal intensity is in proportion of the ground state concentration *n*. In the case where the laser beam for excitation is not sufficiently large, detected signal intensity is in proportion of the ground state concentration *n*, too [10].

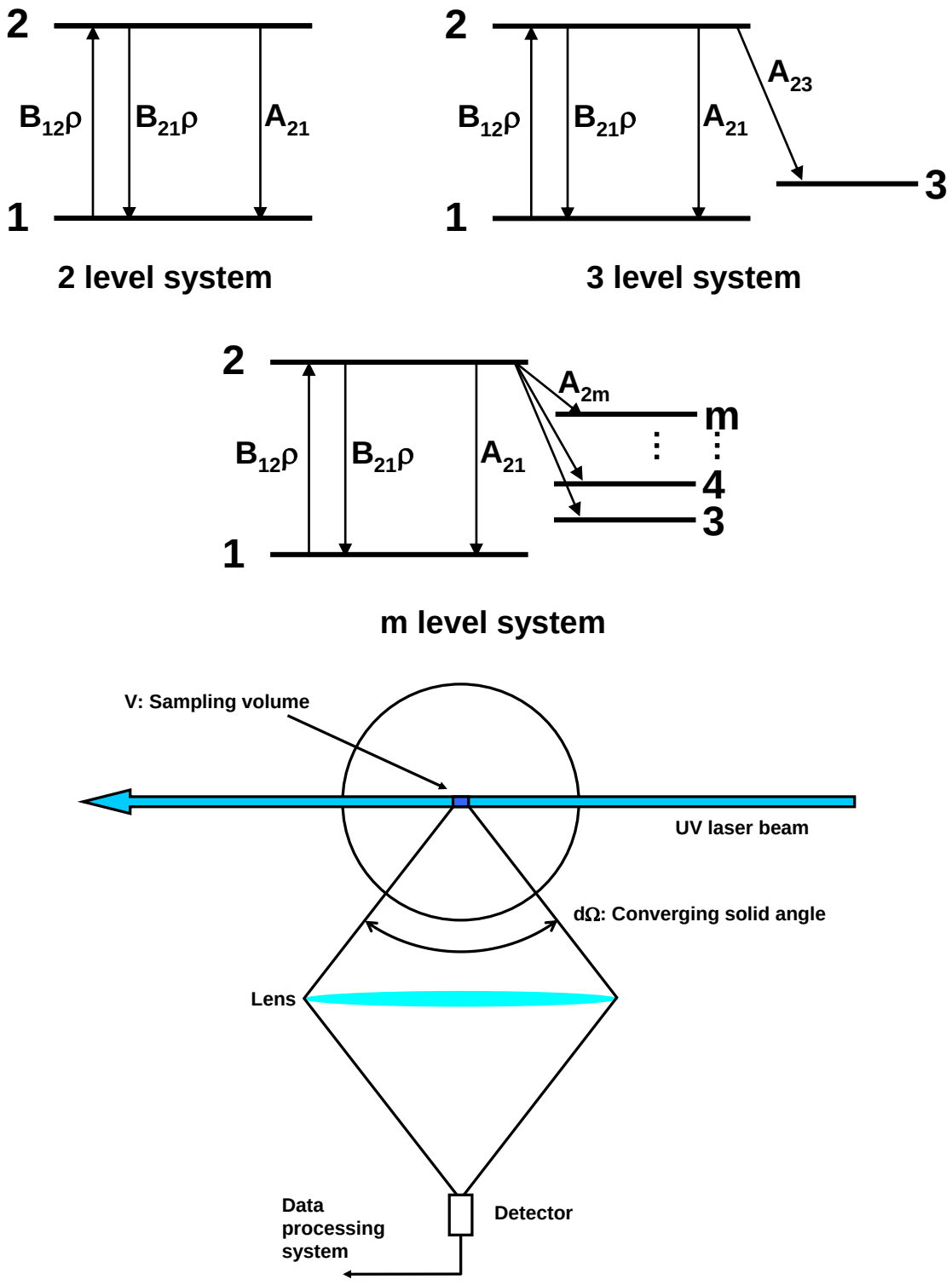

Figure 2.4.1 Diagrams of energy level and optical system for LIF measurement.

2.5 Vacuum Ultraviolet Absorption Spectroscopy (VUVAS)

Optical measurement techniques, such as absorption spectroscopy, OES etc. are very powerful for detecting the behaviors of activated species without disturbing of process plasmas. Recently, these techniques have employed the light in the optical range between vacuum ultraviolet (VUV) and infrared (IR) for probing atomic and molecular radicals. Figure 2.5.1 shows the classification of light. In this study, we have used the absorption spectroscopy employing VUV light for the measurement of atomic radicals, because the atomic radicals have resonance lines in the VUV region. Generally, VUV light is defined as the wavelength region between 0.2 and 200 nm, and is not transmitted through the air medium because of the absorption due to Schmann-Runge band of the oxygen molecular. The spectroscopy in VUV region basically needs some specialized equipments and skills. Therefore, it is very difficult to carry out the measurement of atomic radicals employing VUV spectroscopy.

In the following, the theory of absorption spectroscopy and VUV light sources, such as a micro hollow cathode discharge lump and tunable VUV laser radiation techniques, will be described in detail.

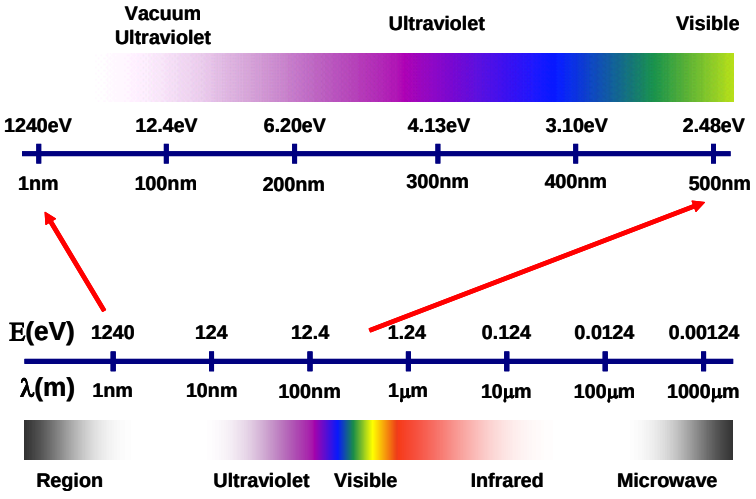

Figure 2.5.1 Classification of light.

2.5.1 Theory of absorption spectroscopy

If the parallel light from a source passes through an absorption medium such as the reactive plasma, the intensity of the light transmitted through the medium is given as follows [11],

$$I(\nu)=I_0(\nu)\exp[-k(\nu)L], \tag{2.5.1}$$

where ν is the frequency, $I(\nu)$ and $I_0(\nu)$ are the intensities of the transmitted light and the incident light, respectively. L is the absorption path length and $k(\nu)$ is the absorption coefficient as a function of frequency ν. The broadening of the absorption coefficient is caused by the phenomena as follows,

(1) Natural broadening due to the finite lifetime of the excited state.
(2) Doppler broadening due to the motions of the atoms.
(3) Lorentz broadening due to collisions with other gases.
(4) Holtsmark broadening due to collisions with other absorption atoms of the same kind
(5) Stark broadening due to collisions with electrons and ions

In this study, the Doppler broadening and the Lorentz broadening should be taken into account because the densities of the electron and the same kind atoms should be low. When a parallel beam-light of frequency ν passes through a layer with the length of dL, we assume that the ground state atom of dN_l cm^{-3} absorb the parallel beam-light in the frequency range from ν to $\nu+d\nu$ and the excited state atoms of dN_u cm^{-3} emit the light in the same frequency range. Moreover, neglecting the effect

of spontaneous re-emission in view of the fact that it takes place in all direction, the decrease of the light-beam energy is given by [12]

$$-\left(I(\nu)\right)d\nu = dN_l dL\rho(\nu)B_{lu}h\nu - dN_u dL\rho(\nu)B_{ul}h\beta\nu\,, \tag{2.5.2}$$

where B_{lu} and B_{ul} are Einstein B coefficient from ground state l to excited state u and from u to l, respectively, h is Planck's constant, and $\rho(\nu)$ is the radiation energy density given by $I(\nu)=c\rho(\nu)$, (c: light velocity). Rewriting Eq. (2.5.2), we obtain

$$-\frac{1}{I(\nu)}\frac{d\left(I(\nu)\right)}{dL}d\nu = \frac{h\nu}{c}\left(B_{lu}dN_l - B_{ul}dN_u\right). \tag{2.5.3}$$

Recognizing that the left-hand term is $k(\nu)$ as defined by Eq. (2.5.1), Eq.(2.5.3) becomes

$$k(\nu)d\nu = \frac{h\nu}{c}\left(B_{lu}dN_l - B_{ul}dN_u\right). \tag{2.5.4}$$

And integrating over the whole absorption line, neglecting the slight variation in ν throughout the line,

$$\int k(\nu)d\nu = \frac{h\nu_0}{c}\left(B_{lu}dN_l - B_{ul}dN_u\right), \tag{2.5.5}$$

where ν_0 is the frequency at the center of the line. Here we use the Einstein *A* coefficient,

$$\begin{aligned}\int k(\nu)d\nu &= \frac{c^2}{8\pi{\nu_0}^2}\frac{g_u}{g_l}AN_l\left(1-\frac{g_l N_u}{g_u N_l}\right)\\ &\cong \frac{c^2}{8\pi\nu^2}\frac{g_u}{g_l}AN_l,\end{aligned} \tag{2.5.6}$$

where g_l and g_u are the statical weights of the lower and upper level, respectively.

Therefore, by measuring $I_0(\nu)$ and $I(\nu)$, $k(\nu)$ is decided and we can estimate the density N_l.

When the beam-light is incoherent such as for a lamp or the linewidth of frequency cannot be neglected in comparison with the broadening of absorption coefficient of observed species, we must consider the linewidth of beam-light to obtain the absorption intensity. The intensity of measured light is the integrated value over the frequency as follows,

$$I_0 = \int e_0 f_0(\nu) d\nu, \tag{2.5.7}$$

$$I_a = \int e_0 f_0(\nu) [1 - \exp\{-k_0 f_a(\nu) L\}] d\nu, \tag{2.5.8}$$

where I_0 and I_a are the intensities of the incident light and the absorption, respectively, $f_0(\nu)$ is the emission line-profile function for the light source, e_0 is the emission intensity of the light source at a center frequency of $f_0(\nu)$, $f_a(\nu)$ is the absorption line-profile function, and k_0 is the absorption coefficient at the center frequency of $f_a(\nu)$. The absorption intensity $A(k_0 L)$ is given by the following formula.

$$\begin{aligned} A(k_0 L) &= 1 - \frac{I_a}{I_0} \\ &= \frac{\int f_0(\nu) [1 - \exp\{-k_0 f_a(\nu) L\}] d\nu}{\int f_0(\nu) d\nu}. \end{aligned} \tag{2.5.9}$$

From $A(k_0 L)$ obtained by the measurement, k_0 is determined by assuming the line-profile function $f_0(\nu)$ and $f_a(\nu)$. Then, the number density of state l, N_l is estimated by using Eq. (2.5.6) as

$$N_l = \frac{8\pi \nu_0^{\,2}}{c^2} \frac{g_l}{g_u} \frac{1}{A} k_0 \int f_a(\nu) d\nu. \tag{2.5.10}$$

2.5.2 VUVAS with microdischarge hollow cathode lamp (MHCL)

Recently, our group has developed a measurement system of absolute densities of H [13], N [14], and O [15] atomic radicals in the ground state using the VUVAS with MHCL as a light source. Traditions used for measuring the absolute H, N and O atom densities are Lyman α (L_α) line at 121.6 nm, $2p^2 3s\,^4P_{5/2,\,3/2,\,1/2}$ - $2p^3\,^4S^o_{3/2}$ at 119.96, 120.02 and 120.07 nm, $3s^3S^o$ - $2p^4\,^3P_{2,1,0}$ at 130.22, 130.49 and 130.6 nm, respectively. Each emission line can be obtained using the H_2, N_2 and O_2 plasma, respectively. However, these emissions are caused by two major processes [16-18]. One is the direct excitation of ground state atomic radicals by the electron impact.

$$X + e \rightarrow X^* + e \rightarrow X + h\nu + e, \tag{2.16}$$

where X is the atomic radical of interest, X^* is X atoms in the excited state. The other is the dissociative excitation of ground state of X_2 by the electron impact.

$$X_2 + e \rightarrow X^* + X + e \rightarrow X + X + h\nu + e. \tag{2.17}$$

Reaction (2.16) is responsible for production of slow excited X^* atoms. Reaction (2.17) can produce fast excited X atoms which produce a large Doppler broadening. Therefore, the structure of the atomic radical emission line profile consists of a two-component velocity distribution arising from two different excitation processes shown in Eqs. (2.16) and (2.17). It is difficult to estimate the emission line profile, which involves a two-component velocity distribution.

In view of the above problem in the measurement of absolute atomic radical density, we have developed a high pressure MHCL as a light source for VUVAS. The specific merits of the MHCL we expect are as follows,

(1) The emission line profile will not involve a large Doppler shift due to the fast excited atomic radical arising from dissociative excitation of molecules, since they should be thermalized before they emit light.

(2) The size of the hollow cathode is as small as 0.1 mm in diameter, resulting in a high current density in the cathode, which is favorable for attaining a high dissociation degree of molecules and obtaining spectrally pure atomic radical emission.

(3) A point-source-like emission from a microhollow can be efficiently coupled to the entrance slit of a monochromator using an appropriate lens system.

(4) The lamp is compact and is operated with an inexpensive dc power source.

The cathode and anode consist of a cupper plate of 0.5 mm thickness with a through-hole hollow of 0.1 mm in diameter. Helium gas containing a small amount of H_2, N_2 or O_2 gas was used. The MHCL was operated at a total pressure of 0.1 MPa.

2.5.3 VUVAS with Electron Cyclotron Resonance (ECR) plasma

To detect F radical by absorption spectroscopy, the most severe technical issue arises from the wavelength of the probe emission. Since the first electronic state of the F radical is located at 12.98 eV above the ground state, the wavelength of the probe emission should be shorter than 100 nm. The transition lines used for F radical measurements are $2p^4 3s^2 P_{1/2}$ - $2p^5\ ^2S^o_{3/2}$ at 95.19 nm, $2p^4 3s^2 P_{3/2}$ - $2p^5\ ^2S^o_{3/2}$ at 95.48 nm, $2p^4 3s^2 P_{1/2}$ - $2p^5\ ^2S^o_{1/2}$ at 95.56 nm and $2p^4 3s^2 P_{3/2}$ - $2p^5\ ^2P^o_{1/2}$ at 95.85 nm. In this VUV wavelength range, no window materials can be used to separate the light source from the target plasma. Thus, the VUVAS system with MHCL as a light source cannot be

used.

For a measurement of absolute F radical density in the grand state, VUVAS with ECR plasma have been used as a light source [19, 20]. The basic principle of VUVAS is the same as that of usual absorption spectroscopy using MHCL. He gas mixed with a small amount of F_2 gas was used as the operating gas of the ECR light source. A set of electromagnet produced a divergent magnetic field of 875 G, which is resonant for a microwave power at a frequency of 2.45 GHz. The light source ECR plasma was typically operated with a microwave power 100 W and a gas pressure of 10 Pa.

2.6 Optical Emission Spectroscopy (OES)

2.6.1 Measurement of Optical Emission Spectrum

Many optical emissions originating from excited species (e.g. atomic and molecular radicals) are generally observed in the plasma. Specific species is identified from the photon energy of the optical emission. Excited species are generated by various processes such as electron collision, dissociation, impact of other excited species, photon absorption, etc. Generally, excitation by electron impact frequently occurs in the plasma. Electron impact excitation of the ground state is given by

$$e + X \rightarrow X^* + e\,, \tag{2.6.1}$$

where X is the species of interest. De-excitation is followed by the emission of a photon from the excited state as,

$$X^* \rightarrow X + h\nu\,. \tag{2.6.2}$$

The intensity of the optical emission due to the transition from an excited state to the ground state is given by

$$I_x \propto n_e n_X \int \sigma_X(\varepsilon) v(\varepsilon) f_e(\varepsilon) d\varepsilon = k_{eX} n_e n_X \quad , \tag{2.6.3}$$

where n_e is the electron density, n_X is the concentration of X, $\sigma X(\varepsilon)$ is the collision cross section for the electron impact excitation of X as a function of electron energy ε, $v(\varepsilon)$ is the electron velocity and $f_e(\varepsilon)$ is the electron energy distribution function (EEDF). $k_e X(\varepsilon)$ is the excitation rate coefficient for X^* by the electron impact on X. Under the condition where k_{eX} and n_e are kept constant, the emission intensity is proportional to the concentration of species. However, both of them are affected by the experimental conditions and are generally so difficult to be kept constant when external parameters, such as input power, working pressure, are varied in the plasma processing. Thereby, optical emission spectroscopy (OES) technique is widely used as a monitoring tool in various plasma processes. Moreover, in order to compare those emission intensities with the concentration of species, it is necessary to assume that emissions from exited states chosen are proportional to the concentration of the same species in the ground state. Therefore, the special technique such as actinometric optical emission spectroscopy (AOES) is frequently applied to estimate relative concentration of species in the ground state [19, 21-26].

Optical emission spectra are generally measured by using a spectrometer. Usually, a monochromator with a photomultiplier tube (PMT) and multi-channel spectrometer with a charged coupled device (CCD) array are used. In a monochromator the light intensity is detected through the exit slit by PMT, as shown in Fig. 2.6.1(a). On the other hand, in a multi-channel spectrometer the light intensity is detected by each pixel of CCD, as shown in Fig. 2.6.1(b). The advantage of the multi-channel spectrometer is that it can measure a wide range (several tens of nm) of wavelength simultaneously; however, the defect of the multi-channel spectrometer is

that the resolution is restricted by the size of the pixel of CCD. The resolution of spectrometer sometimes limits the accuracy of measurements.

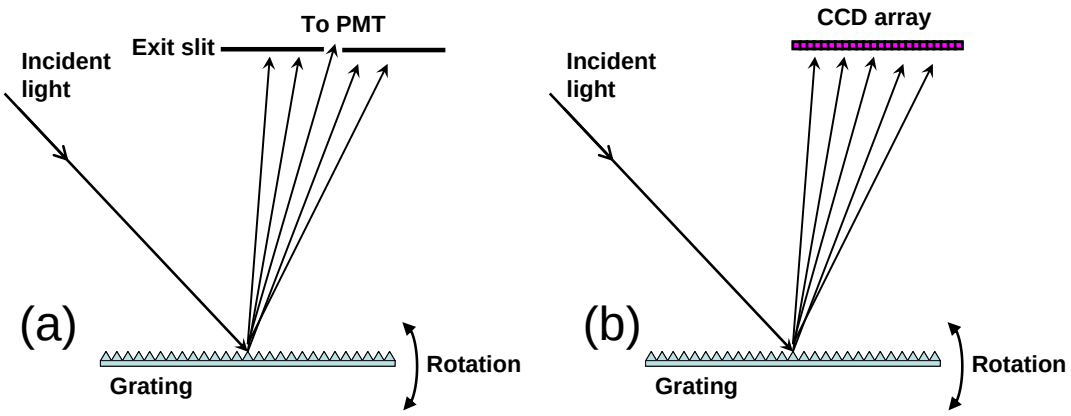

Figure 2.6.1 The schematic illustration of

(a) monochromator and (b) multi-channel spectrometer.

2.6.2 Measurement of rotational temperature of N_2 molecule

The rotational temperature of N_2 molecule can be determined by calculating optical emission spectra of $C^3\Pi_u$ - $B^3\Pi_g$ electronic transitions of N_2 molecule. The electronic transitions take place from the rotational levels of the various vibrational levels of one electronic state to the rotational and vibrational levels of another electronic state. One of the emission spectra of N_2 molecule is called "second positive system", which are due to the electronic transition from $C^3\Pi_u$ state to $B^3\Pi_g$ state having some rotational and vibrational levels. The emission spectra of one vibrational band depend on the rotational temperature because the rotational structures in both $C^3\Pi_u$ state to $B^3\Pi_g$ state are known to follow Boltzmann distributions. Therefore, the rotational temperatures of N_2 molecule can be determined by comparing results between an experimental and a theoretical spectrum.

In this study, the emission spectra of the N_2 (0-2) band at about 308.5 nm were measured. Here, the (0-2) band means the vibrational band of an electronic transition where the vibrational quantum number of the upper state ($C^3\Pi_u$ state) is 0, and the vibrational quantum number of the lower state ($B^3\Pi_g$ state) is 2.

Because line strengths and energy levels of the electronic transition depend on molecular structures, calculations are necessary to determine the theoretical spectrum. The procedure of the calculation is as following.

(1) Calculation of the energy levels for the $C^3\Pi_u$ state and the $B^3\Pi_g$ state.

(2) Calculation of the wavelengths of the transition for each branch followed by selection rules.

(3) Calculation of the line strengths using Hönl-London factors for each transition wavelengths.

(4) Calculation of line shapes and Boltzmann population distributions as functions of spectrum widths and the rotational temperatures.

(5) Fitting of measured spectra with calculated spectra by least-squares approximation using parameters of the spectrum width and the rotational temperature.

The rotational temperature tends to equilibrate with a kinetic temperature because of collisions between neutral and excited molecules. The rotational temperature of N_2 molecule can be used to determine the kinetics of gas temperature.

A) Energy levels of electronic transition

Energy of a molecule can be represented as sums of three parts, that is, an electronic energy T_e, a vibrational energy G_v, and a rotational energy F as follows.

$$E = T_e + G_v + F \,. \tag{2.6.11}$$

The electronic energy T_e and the vibrational energy G_v of N_2 molecule in the $C^3\Pi_u$ state and the $B^3\Pi_g$ state are given in Herzberg [27, 28]. The vibrational term values of an anharmonic oscillator are given by

$$G(v) = w_e\left(v+\frac{1}{2}\right) - w_e x_e\left(v+\frac{1}{2}\right)^2 + w_e y_e\left(v+\frac{1}{2}\right)^3 + \cdots \tag{2.6.12}$$

where the vibrational quantum number v can take the values 0, 1, 2, · · ·. The first term is the term of a harmonic oscillator. w_e, $w_e x_e$, and $w_e y_e$ are constants of the vibrational frequency in wavenumber units (cm^{-1}).

The rotational term values are given as functions of a rotational quantum number J and a rotational constant. The rotational energy levels of the $C^3\Pi_u$ and $B^3\Pi_g$ state are triplet states of spins, and then the rotational term values are given for the multiplet rotational components (Ω=0,1,2). For a Π state (Λ=1), the rotational term values are given by [29]

Table 2.6.1 Electronic, vibrational, and rotational constants in the $C^3\Pi_u$ and $B^3\Pi_g$ state of N_2 molecule. All units are in cm^{-1}.

	$C^3\Pi_u$			$B^3\Pi_g$		
v	B_v	Y_v	$D_v \times 10^6$	B_v	Y_v	$D_v \times 10^6$
0	1.8149	21.5	6.7	1.62849	25.9	6.4
1	1.7933	21.5	6.8	1.61047	26.2	6.5
2	1.7694	21.4	7.3	1.59218	26.4	6.7
3	1.7404	21.1	8.5	1.57365	26.8	6.8
4	1.6999	20.3	12.5	1.55509	27.0	6.9
5	-	-	-	1.53676	27.3	7.0
6	-	-	-	1.51787	27.6	7.2
7	-	-	-	1.49896	27.9	7.3
8	-	-	-	1.47940	28.2	7.5
9	-	-	-	1.46016	28.5	7.7
10	-	-	-	1.44124	28.8	8.0

$C^3\prod_u$: $T_e = 89147.3$, $w_e = 2035.1$, $w_e x_e = 17.08$, $w_e y_e = -2.15$.
$B^3\prod_g$: $T_e = 59626.3$, $w_e = 1734.11$, $w_e x_e = 14.47$.

$$F_0(J) = B_v\left[J(J+1) - Z_1^{1/2} - 2Z_2\right] - D_v\left(J - \frac{1}{2}\right)^4,$$

$$F_1(J) = B_v\left[J(J+1) + 4Z_2\right] - D_v\left(J + \frac{1}{2}\right)^4, \qquad (2.6.13)$$

$$F_2(J) = B_v\left[J(J+1) + Z_1^{1/2} - 2Z_2\right] - D_v\left(J + \frac{3}{2}\right)^4,$$

where

$$Z_1 = Y(Y-4) + \frac{4}{3} + 4J(J+1),$$

$$Z_2 = \frac{1}{3Z_1}\left[Y(Y-1) - \frac{4}{9} - 2J(J+1)\right]. \qquad (2.6.14)$$

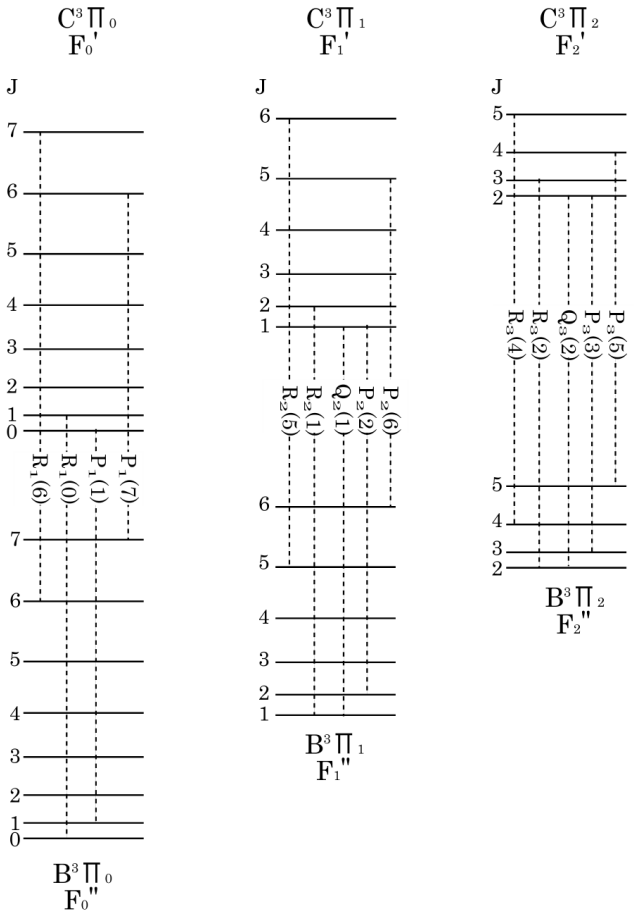

Figure 2.6.2 Energy level diagram for the $C^3\Pi_u$ - $B^3\Pi_g$.

Here, B_v and D_v are rotational constants, and Y is a spin-axis coupling constant, which is a degree of a coupling of a spin to a direction of a nuclear axis. The rotational constant was reported by Hartmann *et al.*[30]. Table 2.6.1 shows the electronic, vibrational, and rotational constant in the $C^3\Pi_u$ and $B^3\Pi_g$ state of N_2 molecule.

The transition energy of the rotation-vibration levels in between the upper state and the lower state can be calculated by

$$E = \left(T_e^{'} - T_e^{''}\right) + \left(G_v^{'} - G_v^{''}\right) + \left(F^{'} - F^{''}\right) . \qquad (2.6.15)$$

Here, wavenumbers of the rotational transitions are obtained for a band *v'-v"* on account of selection rules as following.

$$\begin{aligned}
&\text{R branches} && \nu^{R}_{\Omega;J} = F'_{\Omega;J+1} - F''_{\Omega;J} && \Omega=0,\ 1,\ 2 \\
&\text{Q branches} && \nu^{Q}_{\Omega;J} = F'_{\Omega;J} - F''_{\Omega;J} && \Omega=1,\ 2 \\
&\text{P branches} && \nu^{P}_{\Omega;J} = F'_{\Omega;J-1} - F''_{\Omega;J} && \Omega=0,\ 1,\ 2
\end{aligned} \qquad (2.6.16)$$

Figure 2.6.2 shows an energy level diagram for the $C^3\Pi_u$ - $B^3\Pi_g$ transition. The branches have splits caused by Λ-type doubling, but this effect is typically small relative in this spectrometer resolution, and is neglected in this study.

B) Intensity distributions

On emissions, the rotational distribution population is followed by line strengths, which depend on some branches because of selection rules. The precise formula for the line strength was first given on the basis of the old quantum theory by Hönl and London [31], and then called "Hönl-London factors". The various formulas of the Hönl-London factors are given at the different angular momenta in the molecule, which consist of an electron spin, electronic orbital angular momentum, and angular momentum of nuclear rotation. For the N_2 second positive system ($C^3\Pi_u$ - $B^3\Pi_g$), the intensity distributions are defined with Hund's case (a), in which the interaction of the nuclear rotation with the electronic motion (spin as well as orbital) is very weak, whereas the electronic motion itself is coupled very strongly to the line joining the nuclei [32]. The splitting between the multiplet rotational energy terms of $C^3\Pi_u$ - $B^3\Pi_g$ transitions is about 39 cm^{-1}, where the value is represented by the spin-orbit coupling constant A ($Y=A/B_v$). The value of A is much larger than the splitting between the

rotational lines. The Hönl-London factors of Hund's case (a) are that of a symmetric top with Ω instead of the angular momentum *K* about the top axis [33]. The line strengths *S* using the Hönl-London factors including static weights in the upper state are given by

$$S_{\Omega}^{R}(J) = \frac{(J+\Omega)(J-\Omega)}{J} \quad \text{for } \Delta J=+1 \text{ (R branch)},$$

$$S_{\Omega}^{Q}(J) = \frac{(2J+1)\Omega^2}{J(J+1)} \quad \text{for } \Delta J=0 \text{ (Q branch)}, \tag{2.6.17}$$

$$S_{\Omega}^{P}(J) = \frac{(J+1+\Omega)(J+1-\Omega)}{J+1} \quad \text{for } \Delta J=-1 \text{ (P branch)}.$$

The intensities of the rotational levels are given by thermal distributions of as following [34].

$$I_{em.} = \frac{C_{em,}}{Q_r} S_J \exp\left(-\frac{F'hc}{kT_r}\right). \tag{2.6.18}$$

Here, $C_{em.}$ is a constant depending on the change of the dipole moment and the number of molecules in the upper level, *F*' is the rotational term value of the upper state in Eq. (2.6.13), *h* is a Planck constant, *c* is a light velocity, *k* is a Boltzmann constant, T_r is a rotational temperature, and Q_r is a rotational partition function ($Q_r = kT_r/hcB$). The rotational distribution for the each vibrational transition with a rotational temperature is determined using the equations from Eq. (2.6.13) to Eq. (2.6.18).

To determine the relative vibrational band intensities $I_{v'v''}$, the vibration temperature T_v to give some vibrational structure is known to be given by

$$I_{v'v''} \propto A_{v'v''} \cdot \nu_{v'v''}{}^4 \exp(-E_{v'}/kT_v). \tag{2.6.19}$$

Here, *v'* is a vibrational quantum number of the upper state, *v''* is a vibrational quantum number of the lower state, $A_{v'v''}$ is a Franck-Condon factor [35], $\upsilon_{v'v''}$ is a frequency of the light, and $E_{v'}$ is a vibrational energy of the upper state. Table 2.6.2 shows the

Franck-Condon factor used for the (0-2), (1-3), and (2-4) band of the N_2 $C^3\Pi_u$ - $B^3\Pi_g$ electronic transitions.

Table 2.6.2 Franck-Condon factor of the N_2 $C^3\Pi_u$ - $B^3\Pi_g$ electronic transitions.

Frank-Condon factor			
v'-v''	0-2	1-3	2-4
$\lambda_{v'v''}$	380.5nm	375.5nm	371.0nm
$A_{v'v''}$	0.1462	0.1989	0.1605

C) Calculated emission spectra with rotational and vibrational temperature

The emission distribution caused by the rotational structures is affected by a rotational temperature and a width of each rotational line. The width of the rotational line may be due to an optical phenomenon such as Doppler and Stark broadening, or may be due to instrumental effects such as a slit width of a spectrometer. These effects produce different line shapes which theoretically extend to infinity. The finite line shape is given by [34]

$$g(\Delta\lambda) = \frac{a - (2\Delta\lambda / W)^2}{a + (a-2)(2\Delta\lambda / W)^2}, \qquad (2.6.20)$$

where α and W are variables of line widths, and $\Delta\lambda$ is the wavelength. When the value of α is large, the line shape is similar to a Lorentzian line shape.

Figure 2.6.3 shows the calculated emission spectra of the N_2 $C^3\Pi_u$ - $B^3\Pi_g$ transitions. The emission spectra are calculated at different rotational

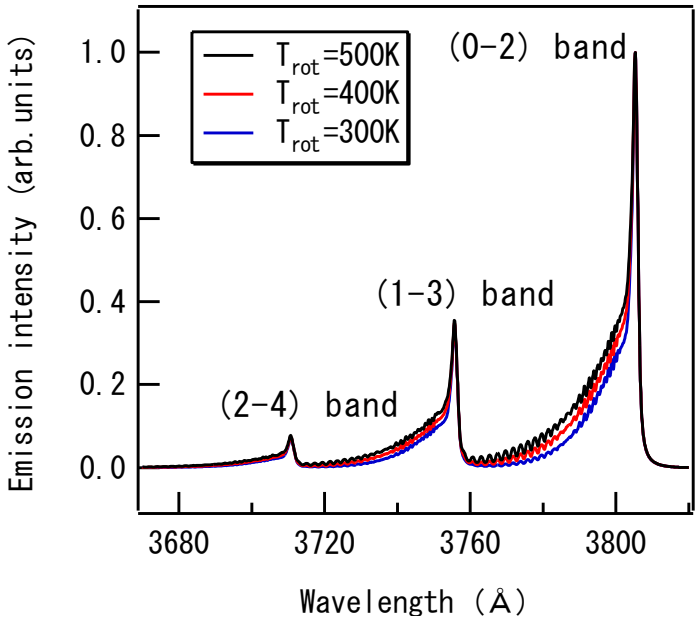

Figure 2.6.3 Calculated emission spectra of the N_2 $C^3\Pi_u$ - $B^3\Pi_g$ electronic transitions at different rotational temperatures of 300 K, 400 K, and 500 K. Spectra line width is calculated using α of 1000 and W of 0.9, and a vibrational temperature T_{vib} is 2000 K.

temperatures of 300 K, 400 K, and 500 K in the condition of α of 1000, W of 0.9, and a vibrational temperature T_{vib} of 2000 K. The calculated emission spectra are normalized at the band head of (0-2) band in 380.4 nm. The distribution of the emission intensities of one vibration band depends on the rotational temperatures, and the relative intensities in the short wavelength with a band head of 380.4 nm were increased with increasing the rotational temperature T_{rot}. The wiggles in the spectra are due to the rotational quantum number of the P, Q, and R branches. The relative positions of the rotational energy levels become wider in high rotational levels J. Therefore, the wiggles could be obviously seen in the region of the short wavelength at one vibrational band.

2.7 Methods for evaluating thin films

2.7.1 Spectroscopic Ellipsometry

Ellipsometry measures a change in polarization as light reflects from or passes through a material structure. The polarization change is represented as an amplitude ratio, Ψ, and the phase difference, Δ. The measured response depends on optical properties and thickness of individual materials. Thus, ellipsometry is primarily used to determine film thickness and optical constants. However, it is also applied to characterize composition, crystallinity, roughness, doping concentration, and other material properties associated with a change in optical response. Since the 1960s, as ellipsometry developed to provide the sensitivity necessary to measure nanometer-scale layers used in microelectronics, interest in ellipsometry has grown steadily. Today, the range of its applications has spread to the basic research in physical sciences, semiconductor communication and data storage devices, flat panel display, biosensor, and optical coating industries.

Ellipsometry measures the interaction between light and material. Light can be described as an electromagnetic wave traveling through space. For purposes of ellipsometry, it is adequate to discuss the waves's electric field behavior in space and time, also known as polarization. The electric field of a wave is always orthogonal to the propagation direction. Therefore, a wave traveling along the z-direction can be described by its x- and y- components. When the light has completely random orientation and phase, it is considered unpolarized. For ellipsometry, however, we are interested in the kind of electric field that follows a specific path and traces out a distinct shape at any point. This is known as polarized light. When two orthogonal light waves are in-phase, the resulting light will be linearly polarized [Fig. 2.7.1(a)]. The relative amplitudes determine the resulting orientation. If the orthogonal waves are 90°

out-of-phase and equal in amplitude, the resultant light is circularly polarized [Fig. 2.7.1(b)]. The most common polarization is “elliptical”, one that combines orthogonal waves of arbitrary amplitude and phase [Fig. 2.7.1(c)].

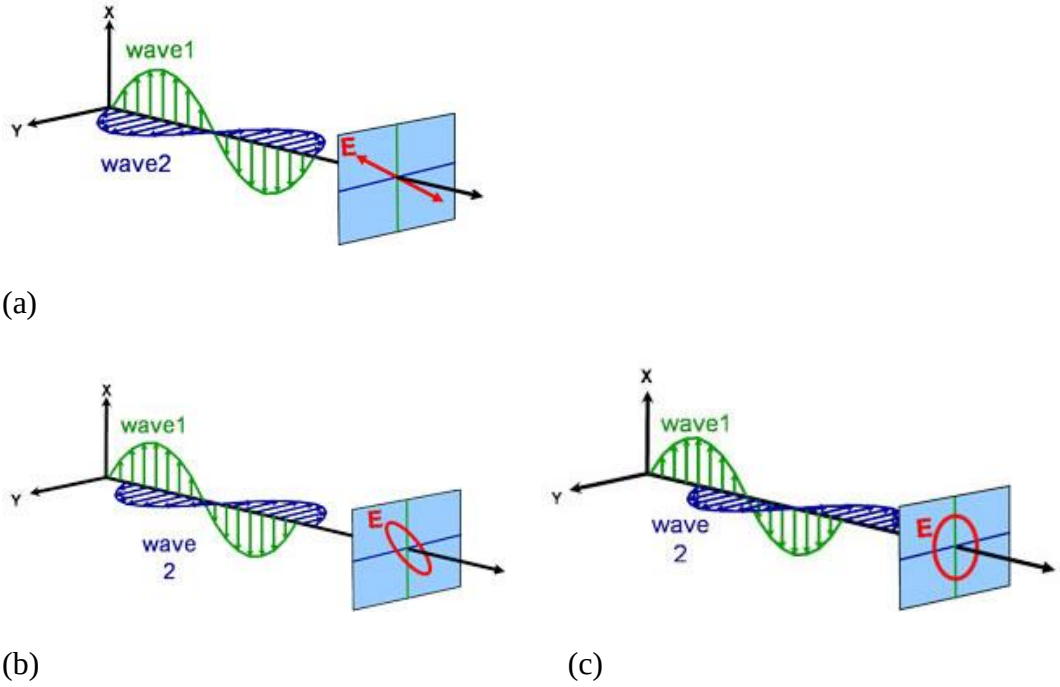

Figure 2.7.1 Orthogonal waves combined to demonstrate polarization:

(a) linear, (b) circular and (c) elliptical.

Maxwell’s equations must remain satisfied when light interacts with a material, which leads to boundary conditions at the interface. Incident light will reflect and refract at the interface, as shown in Fig. 2.7.2. The angle between the incident ray and sample normal (Φ_i) will be equal to the reflected angle, (Φ_r). Light entering the material is refracted at an angle (Φ_t) given by:

$$n_0 \sin(\Phi_i) = n_i \sin(\Phi_t) \tag{2.7.1}$$

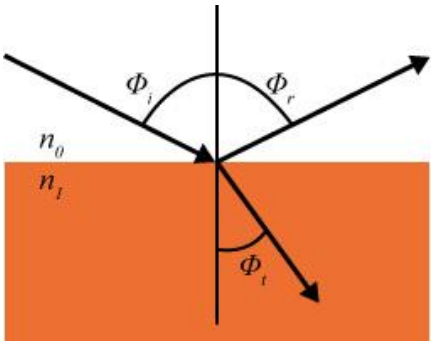

Figure 2.7.2 Light reflects and refracts according to Snell's law.

The same occurs at each interface where a portion of light reflects and the remainder transmits at the refracted angle. This is illustrated in Fig. 2.7.3. The boundary conditions provide different solutions for electric fields parallel and perpendicular to the sample surface. Therefore, light can be separated into orthogonal components with relation to the plane of incidence. Electric fields parallel and perpendicular to the plane of incidence are considered p- and s- polarized, respectively. These two components are independent and can be calculated separately. Fresnel described the amount of light reflected and transmitted at an interface between materials:

$$r_s = \left(\frac{E_{or}}{E_{0i}}\right)_s = \frac{n_i \cos(\Phi_i) - n_t \cos(\Phi_t)}{n_i \cos(\Phi_i) + n_t \cos(\Phi_t)} \tag{2.7.2}$$

$$r_p = \left(\frac{E_{or}}{E_{0i}}\right)_p = \frac{n_t \cos(\Phi_i) - n_i \cos(\Phi_t)}{n_i \cos(\Phi_t) + n_t \cos(\Phi_i)} \tag{2.7.3}$$

$$t_s = \left(\frac{E_{ot}}{E_{0i}}\right)_s = \frac{2n_i \cos(\Phi_i)}{n_i \cos(\Phi_i) + n_t \cos(\Phi_t)} \tag{2.7.4}$$

$$t_p = \left(\frac{E_{ot}}{E_{0i}}\right)_p = \frac{2n_i \cos(\Phi_i)}{n_i \cos(\Phi_t) + n_t \cos(\Phi_i)} \tag{2.7.5}$$

Thin film and multilayer structures involve multiple interfaces, with Fresnel reflection and transmission coefficients applicable at each interface. It is important to track the relative phase of each light component to determine correctly the overall reflected or transmitted beam. For this purpose, we define the film phase thickness as:

$$\beta = 2\pi\left(\frac{t_1}{\lambda}\right)n_1\cos(\Phi_1) \tag{2.7.6}$$

The superposition of multiple light waves introduces interference that depends on the relative phase of each light wave. Figure 2.7.3 illustrates the combination of light waves in the reflected beam and their corresponding Fresnel calculations.

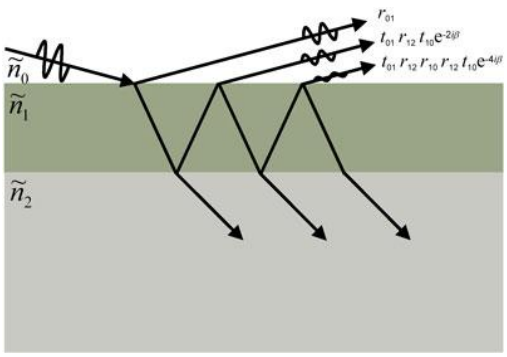

Figure 2.7.3 Light reflects and refracts at each interface, which leads to multiple beams in a thin film. Interference between beams depends on relative phase and amplitude of the electric fields. Fresnel refection and transmission coefficients can be used to calculate the response from each contributing beam.

Ellipsometry is primarily interested in how *p*- and *s*- components change upon reflection or transmission in relation to each other. In this manner, the reference beam is part of the experiment. A known polarization is reflected or transmitted from the sample

and the output polarization is measured. The change in polarization is the ellipsometry measurement, commonly written as:

$$\rho = \tan(\psi)e^{i\Delta} \tag{2.7.7}$$

A sample ellipsometry measurement is shown in Fig. 2.7.4. The incident light is linear with both p- and s- components. The reflected light has undergone amplitude and phase changes for both p- and s- polarized light, and ellipsometry measures their changes.

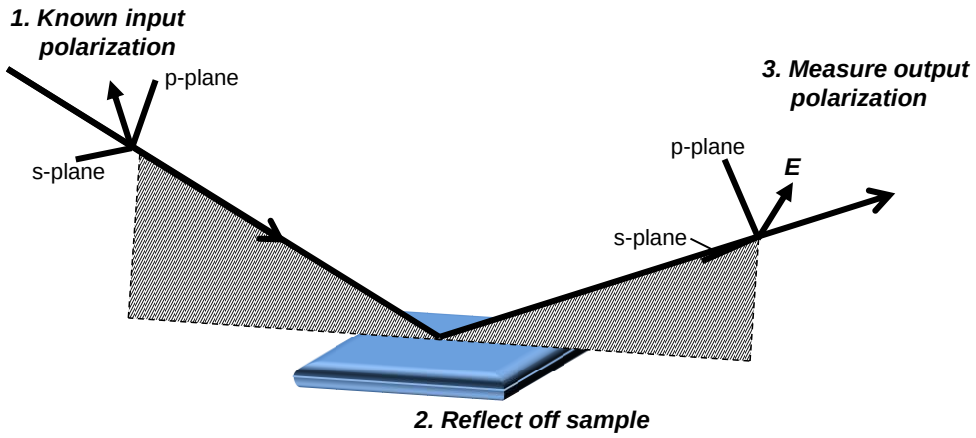

Figure 2.7.4 Typical ellipsometry configuration, where linearly polarized light is reflected from the sample surface and the polarization change is measured to determine the sample response.

The film thickness is determined by interference between light reflecting from the surface and light traveling through the film. Depending on the relative phase of the rejoining light to the surface reflection, interference can be defined as constructive or destructive. The interference involves both amplitude and phase information. The phase information from Δ is very sensitive to films down to sub-monolayer thickness. Ellipsometry is typically used for films whose thickness ranges from sub-nanometers to

a few microns. As films become thicker than several tens of microns, interference oscillations become increasingly difficult to resolve, except with longer infrared wavelengths. Other characterization techniques are preferred in this case. Thickness measurements also require that a portion of the light travel through the entire film and return to the surface. If the material absorbs light, thickness measurements by optical instruments will be limited to thin, semi-opaque layers. This limitation can be circumvented by targeting measurements to a spectral region with lower absorption. For example, an organic film may strongly absorb UV and IR light, but remain transparent at mid-visible wavelengths. For metals, which strongly absorb at all wavelengths, the maximum layer for thickness determination is typically about 100 nm.

2.7.2 X-Ray Photoelectron Spectroscopy (XPS)

X-ray photoelectron spectroscopy (XPS) is currently the most widely used surface-analytical technique, and is therefore described here in more detail than any of the other techniques. At its inception by Seigbahn and coworkers [36], it was called ESCA (electron spectroscopy for chemical analysis), but the name ESCA is now considered too general, because many surface-electron spectroscopies exist, and the name given to each one must be precise. The name ESCA is, nevertheless, still used in many places, particularly in industrial laboratories and their publications. Briefly, the reasons for the popularity of XPS are the exceptional combination of compositional and chemical information that it provides, its ease of operation, and the ready availability of commercial equipment.

The surface to be analyzed in irradiated with soft X-ray photons. When a photon of energy *hv* interacts with an electron in a level X with the binding energy E_B,

the entire photon energy is transferred to the electron, with the result that a photoelectron is ejected with the kinetic energy

$$E_{kin}\,(_{hv}, X) = h\nu - E_B - \Phi_s \qquad (2.7.8)$$

where Φ_s is a small, almost constant, work function term. Obviously, $h\nu$ must be greater than E_B. The ejected electron term can come from a core level or from the occupied portion of the valence band, but in XPS most attention is focused on electrons in core levels. Because no two elements share the same set of electronic binding energies, measurement of the photoelectron kinetic energies enables elemental analysis. In addition, Eq. (2.7.8) indicates that any changes in E_B are reflected in E_{kin}, which means that changes in the chemical environment of an atom can be followed by monitoring changes in the photoelectron energies, leading to the provision of chemical information. XPS can be used for analysis of all elements in the periodic table except hydrogen and helium.

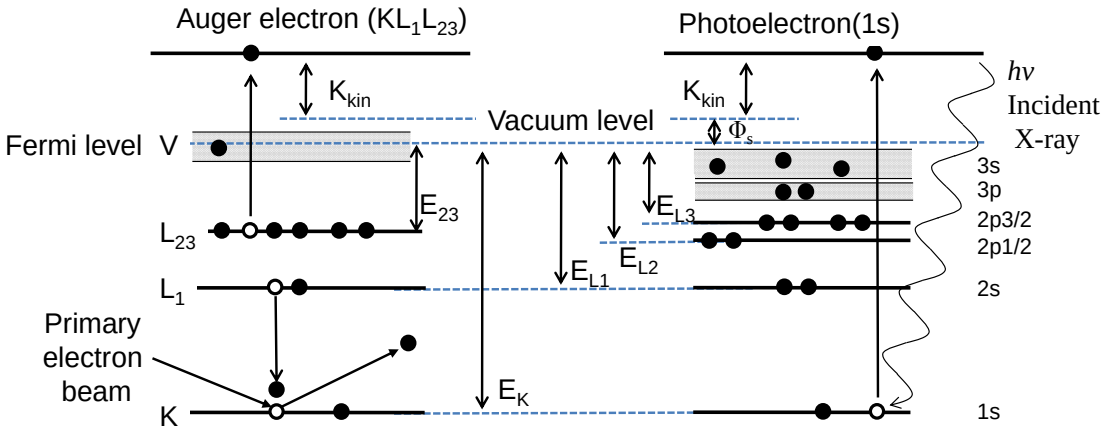

Figure 2.7.5 Schematic diagram of electron emission processes in solids.

Left side: Auger process, right side: photoelectron process.

Electrons involved in the emission processes are indicated by open circles in Fig. 2.7.5. Although XPS is concerned principally with photoelectron and their kinetic energies, ejection of electron by other processes also occurs. An ejected photoelectron leaves behind a core hole in the atom. The sequence of events following the creation of the hole is shown schematically in Fig. 2.7.5 (right side). In the example, the hole has been created in the K-shell, giving rise to a photoelectron, the kinetic energy of which would be ($h\nu$-E_K), and is filled by an electronic transition from the unresolved L_{23} shell. The energy E_K-E_{L23} associated with the transition can then either be dissipated as a characteristic X-ray photon or given up to an electron in the same or a higher shell, shown in this example also as the L_{23}. The second of these possibilities is called the Auger process after its discoverer [37], and the resulting ejected electron is called an Auger electron and has kinetic energy given by:

$$E_{kin}(KL_1L_{23}) = E_K - E_{L1} - E_{L23} - E_{inter}(L_1L_{23}) + E_R - \Phi_s \qquad (2.7.9)$$

where $E_{kin}(KL_1L_{23})$ is the interaction energy between the holes in the L_1 and L_{23} shell and E_R is the sum of the intra-atomic relaxation energies. X-ray photon emission and Auger electron emission are obviously competing processes, but for the shallow core levels involved in XPS and AES the Auger process is for more likely.

Thus in all X-ray photoelectron spectra, features appear as a result of both photo-emission and Auger emission. In XPS, the Auger features can be useful but are not central to the technique, whereas in AES, Eq. 2.7.9 forms the basis of the technique. At this point the nomenclature used in XPS and AES should be explained. In XPS the spectroscopic notation is used, and in AES the X-ray notation. The two are equivalent, the different usage having arisen for historical reasons, but the differentiation is a convenient one. They are both based on the so-called *j-j* coupling scheme describing the

orbital motion of an electron around an atomic nucleus, in which the total angular momentum of an electron is found by summing vectorially the individual electron spin and orbital angular momentum. Thus if l is the electronic orbital angular momentum quantum number and s the electronic spin angular momentum quantum number, the total angular momentum for each electron is given by $j = l \pm s$. Because l can take the values 0, 1, 2, 3, 4, … and s = 1/2 clearly j = 1/2. 3/2, 5/2 etc. The principal quantum number n can take values 1, 2, 3, , … In spectroscopic notation, states with l = 0, 1, 2, 3, … are designated *s, p, d, f,* … respectively, and the letter is preceded by the number n; the j values are then appended as suffixes. Therefore, one obtains 1*s*, 2*s*, $2p_{1/2}$, $2p_{3/2}$.

In X-ray notation, states with n = 1, 2, 3, 4 … are designated K, L, M, N, …, respectively, and states with various combinations of l = 0, 1, 2, 3, … and j = 1/2, 3/2, 5/2 are appended as the suffixes 1, 2, 3, 4 … In this way one arrives at K, L_1, L_2, L_3, M_1, M_2, M_3, etc. The equivalence of the two notations is set out in Table 2.7.1.

Table 2.7.1 Spectroscopic and X-ray notaion.

Quantum number			*Spectroscopic state*	*X-ray state*
N	***L***	***J***		
1	0	1/2	1*s*	K
2	0	1/2	2*s*	L_1
2	1	1/2	$2p_{1/2}$	L_2
2	1	3/2	$2p_{3/2}$	L_3
3	0	1/2	3*s*	M_1
3	1	1/2	$3p_{1/2}$	M_2
3	1	3/2	$3p_{3/2}$	M_3
3	2	3/2	$3d_{3/2}$	M_4
3	2	5/2	$3d_{5/2}$	M_5
etc.	*etc.*	*etc.*	*etc.*	*etc.*

References

[1] T. Shirakawa and H. Sugai, Jpn. J. Appl. Phys. **32** 5129 (1993).

[2] T. H. Ahn, K. Nakamura and H. Sugai, Jpn. J. Appl. Phys. **34** L1405 (1995).

[3] M. Goto, H. Toyoda, M. Kitagawa, T. Hirao and H. Sugai, Jpn. J. Appl. Phys. **36** 3714 (1997).

[4] A. Schwabedissen, E. C. Benck and J. R. Roberts, Plasma Sources Sci. Technol. **7** 119 (1998).

[5] K. Nakamura, H. Kokura, I. Ghanashev and H. Sugai, Bull. Am. Phys. Soc. **43** 1416 (1998)

[6] H. Kokura, K. Nakamura, I. P. Ghanashev and H. Sugai, Jpn. J. Appl. Phys. **38** 5262 (1999)

[7] A. W. DeSilva and G. C. Goldenbaum, in *Methods of Experimental Physics*, edited by H. R. Lovbereg (Academic, New York, 1970), Vol. 9.

[8] A. Kono and K. Nakatani, Rev. Sci. Instrum. 71 2716 (2000).

[9] C. Suzuki, K. Sasaki, and K. Kadota, J. Appl. Phys. 82, 5321 (1997).

[10] C. Suzuki, DC Thesis, Appendix A, Nagoya University (1999).

[11] A. G. G. Mitchell, and M. W. Zemensky, Resonance Radiation and Excited Atoms (Cambridge, London, 1961).

[12] M. Shimazu, J. Spectroscopical Res. Japan, 24, 255 (1975).

[13] S. Takashima, M. Hori, T. Goto, A. Kono, M. Ito, and K. Yoneda, Appl. Phys. Lett., **75** 3929 (1999)

[14] S. Takashima, S. Arai, A. Kono, M. Ito, K. Yoneda, M. Hori, and T. Goto, J. Vac. Sci. Technol. A **19**, 599 (2001).

[15] H. Nagai, M. Hiramatsu, M. Hori, and T. Goto, Rev. Sci. Instrum. **74**, 3453 (2003).

[16] R. S. Freund, J. A. Schiavone, and D. F. Brader, J. Chem. Phys., **64**, 1122 (1976)

[17] K. Ito, N. Oda, Y. Hatano, and T. Tsuoi, Chem. Phys., **21**, 203 (1977)

[18] S. Djurovic and J. R. Roberts, J. Appl. Phys., **74**, 6558 (1993)

[19] Y. Kawai, K. Sasaki and K. Kadota, Jpn. J. Appl. Phys. Vol. **36** L1261 (1997).

[20] K. Sasaki, Y. Kawai and K. Kadota, Appl. Phys. Lett. **70** 1375 (1997).

[21] J. W. Corburn and M. Chen, J. Appl. Phys. **51**, 3134 (1980).

[22] R. E. Walkup, K. L. Saenger, and G. S. Sewyn, J. Chem. Phys. **84**, 2668 (1986).

[23] H. M Katsch, A. Tewes, E. Quandt, A. Goehlich, T. Kawetzki, and H. F. Dobele, J. Appl. Phys. **88**, 6232 (2000).

[24] S. F. Durrant and M. A. B. Moraes, J. Vac. Sci. Technol. A, **13**, 2513 (1995).

[25] S. F. Durrant and M. A. B. Moraes, J. Vac. Sci. Technol. A , **16**, 509 (1998).

[26] A. Gicquel, M. Chenevier, Kh. Hassouni, A. Teserepi, and M. Dubus, J. Appl. Phys. **83**, 7504 (1998).

[27] G. Herzberg, Molecular Spectra and Molecular Structure, Vol. **I**, 552 (1966).

[28] G. Herzberg, The Spectra and Structures of Simple Free Radicals, Chapter 2, 24 (1971).

[29] G. Herzberg, Molecular Spectra and Molecular Structure, Vol. **I**, Caapter 5, 235 (1966).

[30] G. Hartmann and P. C. Johnsont, J. Phys. B: Molec. Phys. **11**, 1597 (1978).

[31] H. Hönl and F. London, Z. Physik **33**, 803 (1925).

[32] G. Herzberg, Molecular Spectra and Molecular Structure, Vol. **I**, Chapter 5, 219 (1966).

[33] G. Herzberg, Molecular Spectra and Molecular Structure, Vol. **Ⅲ**, Chapter 2, 226 (1966).

[34] D. M. Phillips, J. Phys. D: Appl. Phys. **8**, 507 (1975).

[35] W. Benesch, J. T. Vanderslice, S. G. Tilford, and P. G. Wilkinson, Astrophys. **144**, 408 (1966).

[36] K. Siegbahn, C. Nordling, A. Fahlman, R. Nordberg, K. Hamrin,J. Hedman, G. Johnsson, T. Bergmark, S.-E. Karisson, I. Lindgreen, B. Lindberg: ESCA: Atomic, Molecular, and Solid Sate Structure Studied by Means of Electron Spectroscopy. Almqvist and Wiksells, Uppsala 1967.

[37] P. Auger, J. Phys. Radium 6, 205 (1925)

Chapter 3

Measurements of electron energy distribution function in dual frequency capacitively coupled plasma using laser Thomson scattering

3.1 Introduction

The successful use of capacitively coupled plasmas (CCPs) in microelectronics fabrication is predicated because of the ability of controlling the energy and angular distributions of reactant species to the wafer [1]. In conventional, single frequency CCPs, there is a tradeoff between controlling the ion energy and angular distribution (IEAD) and the rate of plasma production as a function of excitation frequency and gas pressure [2]. More advanced dual-frequency CCPs separate these functions by attempting to control the IEAD using low frequency excitation and using a high frequency excitation to control the production of the plasma and so the magnitude of fluxes to the substrate [3]. New designs of CCPs are intended to provide additional control of the reactant fluxes to the substrate. One such example is a dc-superposed CCP. Recently, dual frequency CCP with negative dc bias superposed on the VHF power on

the upper electrode have been proposed as a new technology for advanced plasma processing. The superposition of a negative dc voltage to the lower electrode in parallel-plate type CCP was first reported in the 1990s [4]. Recently, several researchers reported their computational results that the sheath structure is superposed electromagnetically by a dc sheath and an rf sheath when the negative dc voltage is applied to the electrode [5-9]. It has been experimentally recognized that the sheath voltage is modulated by this superposition, and the bombardment of ions accelerated by the high sheath voltage will enhance the generation of secondary electron emission [9]. The electrons generated on the electrode surface accelerate back into the plasma, thereby increasing the plasma density [5-9]. Kawamura *et al*. have reported simulation results for the characteristics of a superposed dc/rf sheath. They concluded that secondary electron emission from the surface of the electrodes significantly affected plasma parameters such as electron density and the electron energy distribution function (EEDF) [4,5]. They did not, however, report any experimental results, only computational results. Thus, any effects of the dc-superposition need to be analyzed and experimentally demonstrated.

In this study, we report the results of electron property measurements of dc-superposed CCP using laser Thomson scattering. Laser Thomson scattering is a relatively complicated method experimentally, but has significant advantages including being a non-perturbing method and allowing straightforward interpretation of experimental results.

3.2 Experimental setup

Figure 3.1 shows a schematic of a commercially available dual frequency

capacitively-coupled-plasma reactor. The reactor can process 300-mm diameter wafers. In the conventional CCP setup for dielectric material etching processes, VHF (60 MHz) power is applied to the upper electrode made of silicon and sustained the plasma discharge. The temperature of the upper electrode and side wall were maintained at 60 °C by circulating a temperature-control coolant. Radio frequency (13.56 MHz) power was applied to the lower electrode to control the energies for ion-bombardment onto the samples. A-300 mm wafer was electrostatically chucked on the lower electrode which was cooled to a temperature of 20 °C. In the case of dc-superposition, a dc bias was simultaneously applied to the upper electrode. The highest dc bias was -410 V for the experiments in this chapter. A mixture of Ar, O_2 and c-C_4F_8 gases with flow rates of 800, 20, and 2 sccm, respectively, were introduced into the chamber through the shower-head of the upper electrode and maintained at a pressure of 5.3 Pa by an automatic pressure controller. The gap between the electrodes was 35 mm.

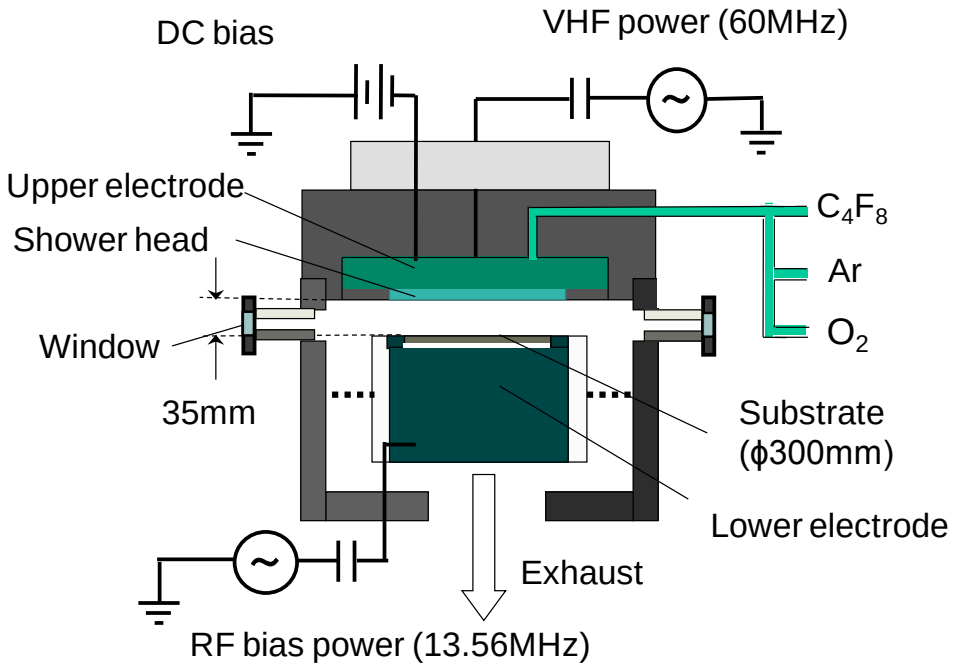

Figure 3.1 Schematic of dual-frequency CCP reactor.

Figure 3.2 shows a schematic diagram of a laser Thomson scattering measurement system. The light source was a frequency doubled Nd:YAG laser (532 nm) operated at a pulse repetition frequency 30 Hz and a pulse width 5 ns. The laser energy in the scattering volume was 550 mJ and the signal was accumulated for 1×10^5 laser shots. The laser beam with vertical polarization was focused at the center of the plasma chamber using a lens of a focal length of 50 cm. Thomson light scattered from the vicinity of the focal point was collected by a lens and focused on the entrance slit to enhance the ratio between the Thomson signal and the background plasma emission. To eliminate the effect of background plasma emission, Q switching of the YAG laser was suppressed in every other exposure and only the light emitted from the plasma was recorded; the data were subtracted from those acquired with the laser beam on.

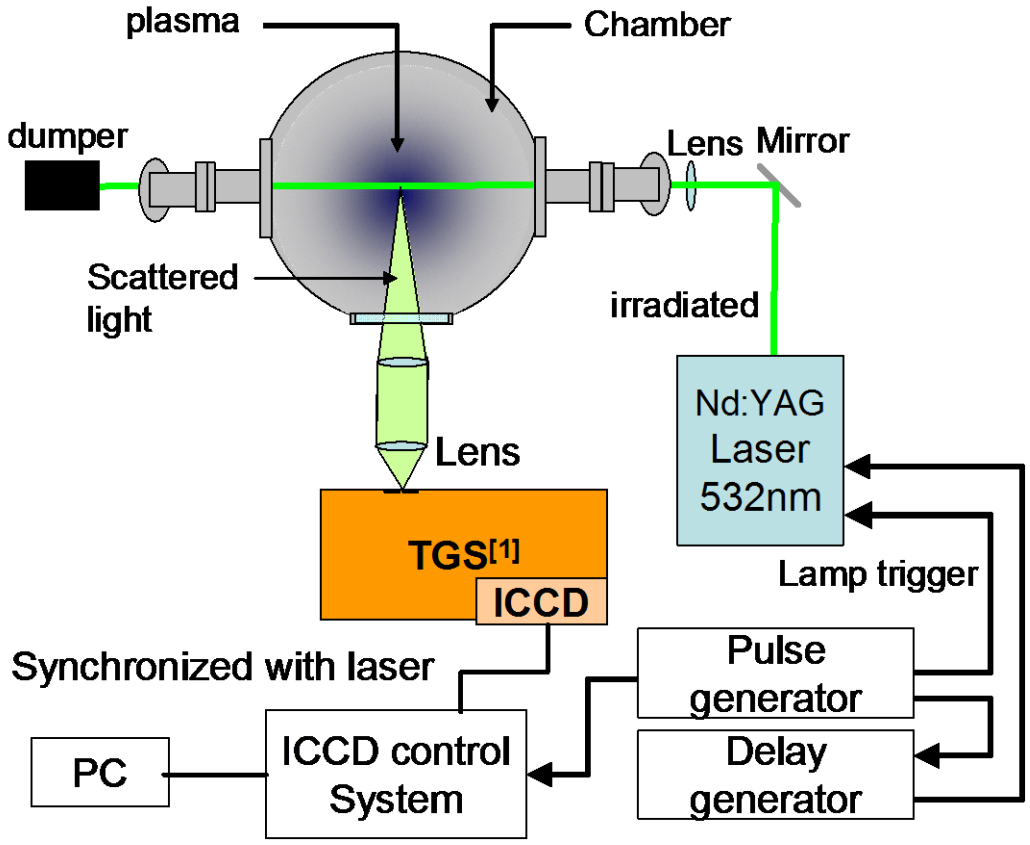

Figure 3.2 schematic diagram of laser Thomson scattering measurement system.

3.3 Results and Discussion

Figure 3.3(a), (b), (c), (d) and (e) shows Thomson scattering spectra as a function of dc bias. The spectra are plotted as a function of [10]

$$E_p \equiv m\upsilon_p^2/2, \tag{3.1}$$

where

$$\upsilon_p = \frac{c}{2\sin(\theta/2)}\frac{\Delta\lambda}{\lambda_0}. \tag{3.2}$$

Here, m is the electron mass, c the light velocity, $\Delta\lambda$ the wavelength shift of the scattered light, λ_0 the laser wavelength (532 nm), and θ the scattering angle (= 90°). In Eq. (3.2), υ_p gives the one-dimensional projection of the electron velocity in the direction of $\mathbf{k_0} - \mathbf{k_s}$, where $\mathbf{k_0}$ and $\mathbf{k_s}$ are the wave vectors of laser light and the scattered light, respectively, and hence E_p is the partial kinetic energy of electrons associated with υ_p. For convenience, we refer to a Thomson spectrum as a function of E_p as 1D EEPF (one dimensional electron energy probability function), since it has the same functional form $C\exp(-E_p/T_e)$ (T_e is the electron temperature in energy unit and C is a constant) as the usual 3D EEPF when the EEDF is Maxwellian. It is indicated that the electron temperature is directly obtained from the slope of the decaying part of the plot in Fig. 3.3.

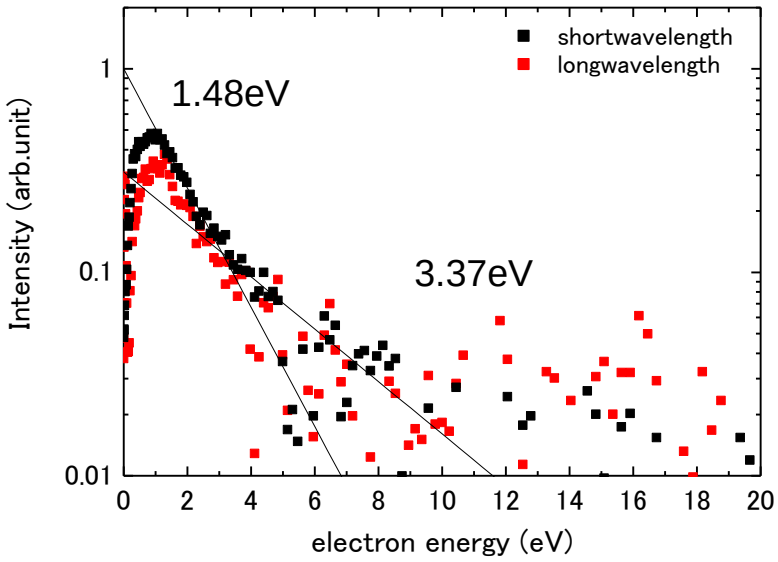

(a) DC = 0V

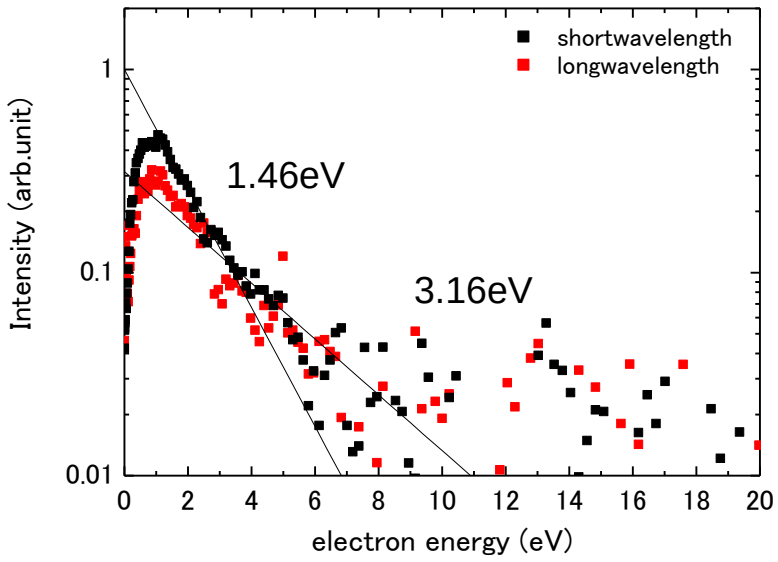

(b) DC = -180V

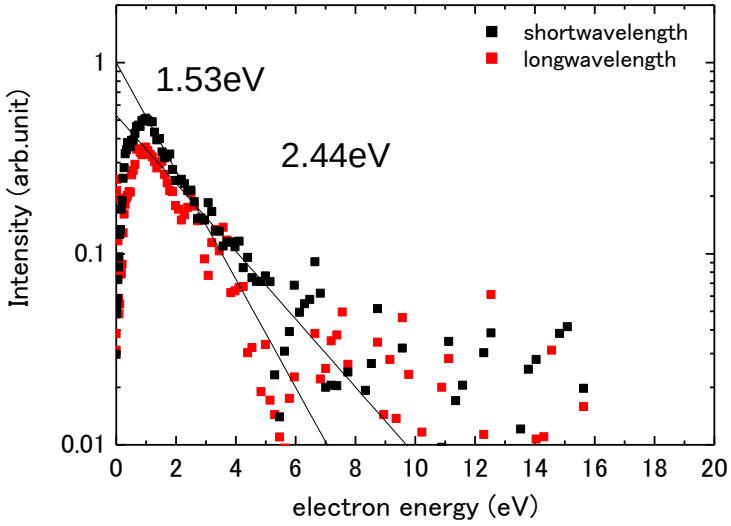

(c) DC = -230V

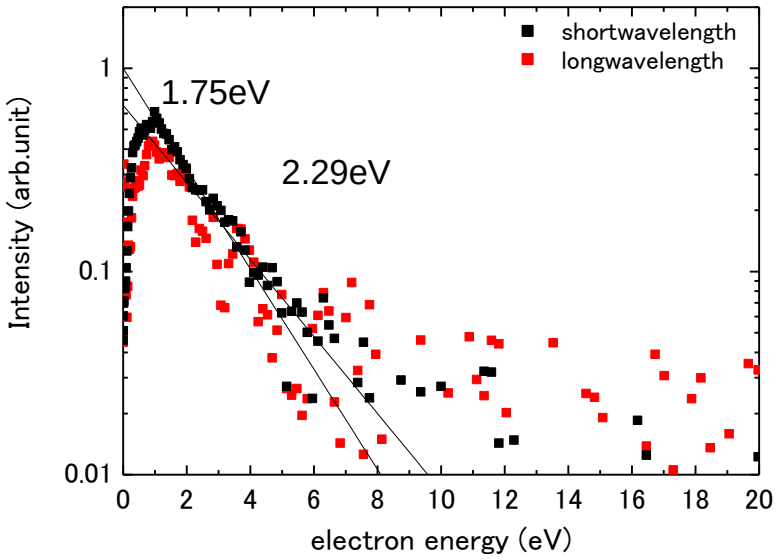

(d) DC = -310V

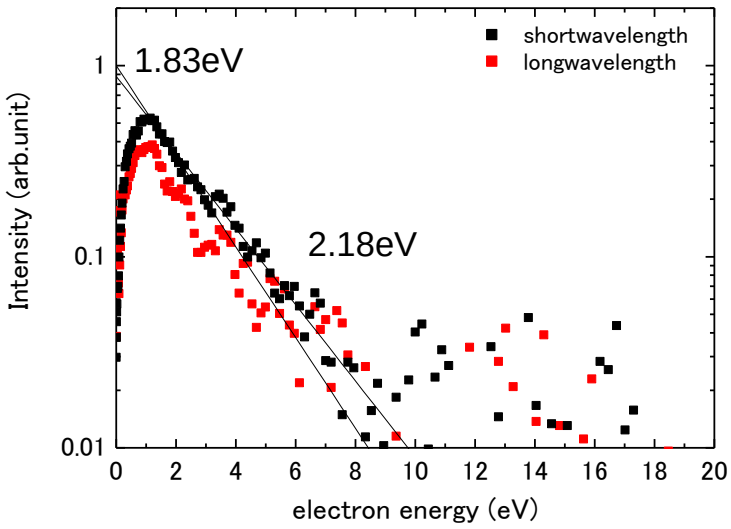

(e) DC = -410V

Figure 3.3 Thomson spectra.

The observed 1D EEPF were not Maxwellian. A non-Maxwellian EEDF was observed for all conditions in Fig. 3.3. Approximation of each plot by two straight lines is shown in the figure, together with the electron temperatures associated with the slope of the straight lines. The non-Maxwellian EEDF could be considered as a summation of Maxwellian distributions of two groups of electrons. In other words, they considered the EEDF as containing of separate low temperature and high temperature components. The figures indicate that with increasing the superposed dc bias, the electron temperature in the low-energy part was increased while that in the high-energy part was decreased. The electron temperature variation as a function of dc bias was summarized in Fig. 3.4. When the superposed dc bias was increased from 0 to -410 V, the electron temperature in the low-energy part was slightly increased from 1.48 to 1.83 eV while that in the high-energy part was decreased from 3.37 to 2.18 eV. In a CCP at low pressure, the high temperature component of the EEDF was attributed to stochastic electron heating in the

rf sheaths of the plasma. On the other hand, for a CCP driven by a combination rf and dc power sources, a dc/rf sheath develops on the negatively dc-biased electrode [5,6]. The dc/rf sheath has a dc sheath has a dc region with negligible electron density near the negatively biased electrode. In the dc region, there is no electron heating because of its negligible electron density. Hence, if the rf power absorbed by the discharge is fixed, the rf and dc regions of the voltage drop across the rf sheath are independent of dc voltage. As a result, the high temperature component of the EEDF was decreased because the dc source alters the sheath voltages and widths at the electrode surface.

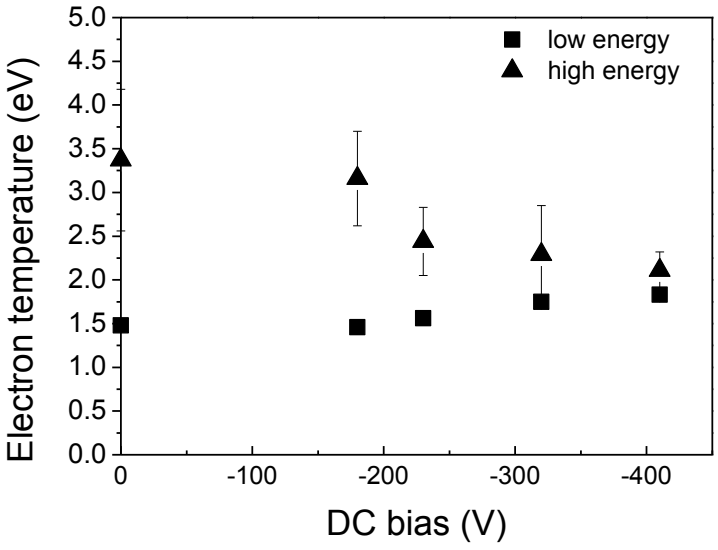

Figure 3.4 Electron temperature as a function of dc bias.

Figure 3.5 shows the electron density as a function of dc bias. When the superposed dc bias was increased from 0 to -410 V, the electron density increased from 2.2 to 2.8×10^{11} cm^{-3}. In the dc biasing, the dc source alters the sheath voltages and widths at the upper electrode and the increase in the electron density mainly depends on the γ effect, wherein positive ion bombardment of the surface of the upper electrode

increased due to the dc bias applied to the upper electrode. Following the energy dependence of secondary electron emissions, the amount of secondary electrons increases with augmentation of the negative dc bias, due to the rise in ion bombardment energy [7,8]. In fact, by superposing the dc bias on the upper electrode, the dc current flow drastically increased. Figure 3.6 shows the dc current as a function of the negative dc bias. Below Vdc of -230 V, no significant dc current flowed. Close to a Vdc of -230 V, the dc current increased abruptly from 0.1 to 2.5 A. Exceeding above the Vdc of -230 V, the dc current increased monotonically as if the secondary electron emissions increased with increasing ion bombardment. Thus, the dc current measurement indicated that the increase in dc current flow in the upper electrode arises from an increase in energy of ion bombardment accelerated by the dc bias. Secondary electrons are generated by positive ion bombardment of the electrode, and are accelerated by the sheath and injected back into the plasma. As a result, the electron density increases by the application of the dc bias.

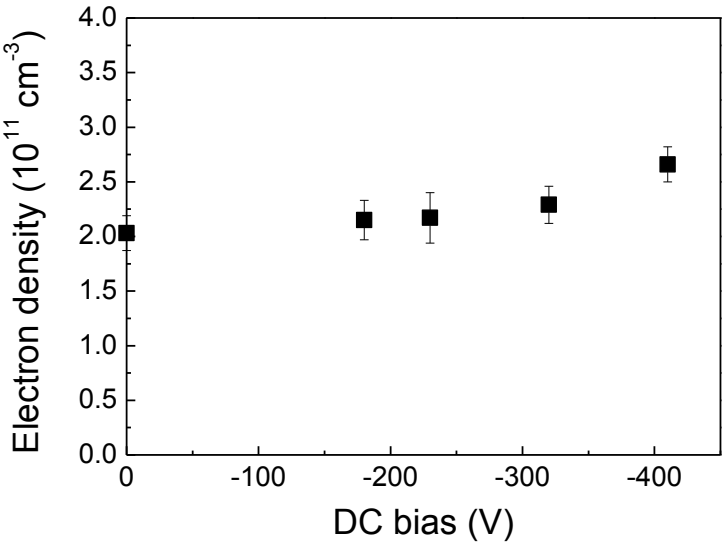

Figure 3.5 Electron density as a function of dc bias.

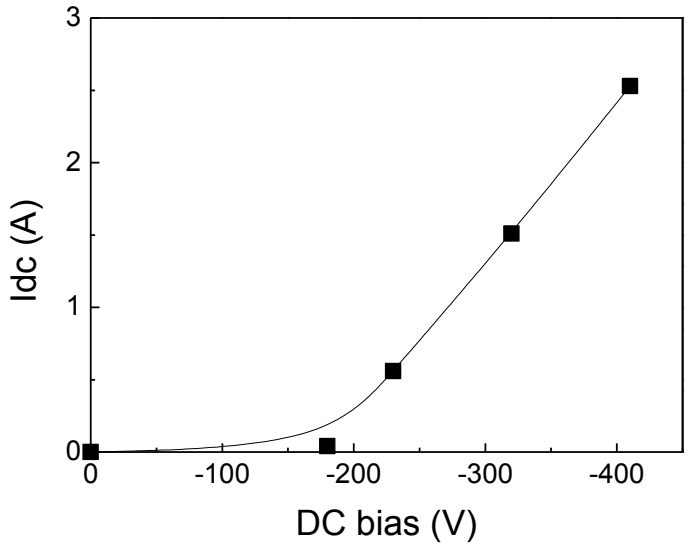

Figure 3.6 dc current flow through the upper electrode on superposed dc bias.

3.4 Summary

In summary, the author has reported measurements of the EEDF in dc superposed dual frequency capacitively coupled plasma using the methods of laser Thomson scattering. A non-Maxwellian EEDF was observed for all conditions. The non-Maxwellian EEDF could be considered as a summation of Maxwellian distributions of two groups of electrons. In other words, the EEDF was considered to contain separate low temperature and high temperature components. As the results, with increasing the superposed dc bias, the electron temperature in the low-energy part was increased while that in the high-energy part was decreased. When the superposed dc bias was increased from 0 to -410 V, the electron temperature in the low-energy part was slightly increased from 1.48 to 1.83 eV while that in the high-energy part was decreased from 3.37 to 2.18 eV. In a CCP at low pressure, the high temperature component of the

EEDF was attributed to stochastic electron heating in the rf sheaths of the plasma. On the other hand, for a CCP driven by a combination rf and dc power sources, a dc/rf sheath develops on the negatively dc-biased electrode. The dc/rf sheath has a dc sheath has a dc region with negligible electron density near the negatively biased electrode. In the dc region, there is no electron heating because of its negligible electron density. Hence, if the rf power absorbed by the discharge is fixed, the rf and dc regions of the voltage drop across the rf sheath are independent of dc voltage. As a result, the high temperature component of the EEDF was decreased because the dc source alters the sheath voltages and widths at the electrode surface. On the other hand, the results indicated the increase of electron density with increasing the dc bias voltage. When the superposed dc bias was increased from 0 to -410 V, the electron density increased from 2.2 to 2.8×10^{11} cm^{-3}. The dc source induces a dc current flow through the plasma and alters the sheath voltages and widths in the upper electrode. Secondary electrons are generated by positive ion bombardment of the electrode, and are accelerated by the sheath and injected into the plasma. As a result, the electron density increases by the application of the dc bias.

Reference

[1] S.-B. Wang and A. E. Wendt, J. Appl. Phys. **88**, 643 (2000).

[2] T. Novikova, B. Kalache, P. Bulkin, K. Hassouni, W. Morscheidt, and P. Roca i Cabarrocas, J. Appl. Phys. **93**, 3198 (2003).

[3] T. Kitajima, Y. Takeo, Z. Lj. Petrovic, and T. Makabe, Appl. Phys. Lett. **77**, 489 (2000).

[4] K. Kohler. J. W. Coburn, D. E. Horne, E. Kay, and J. H. Keller, J. Appl. Phys. **57**, 59 (1985).

[5] E. Kawamura, M. A. Lieberman, A. J. Lichtenberg, and E. A. Hudson, J. Vac. Sci. Technol. A **25**, 1456 (2007).

[6] E. Kawamura, A. J. Lichtenberg, and M. A. Lieberman, Plasma Sources Sci. Technol. **17**, 045002 (2008).

[7] K. Denpoh and P. L. G. Ventzek, J. Vac. Sci. Technol. A **26**, 1415 (2008).

[8] P. L. G. Ventzek, and K. Denpoh, J. Vac. Sci. Technol. A **27**, 287 (2009).

[9] L. Xu, L. Chen, M. Funk, A. Ranjan, M. Hummel, R. Bravenec, R. Sundarajan, D. J. Economou, and V. M. Donnelly, Appl. Phys. Lett. **93**, 261502 (2008).

[10] A. W. DeSilva and G. C. Goldenbaum, in *Methods of Experimental Physics*, edited by H. R. Lovbereg (Academic, New York, 1970), Vol. 9.

[11] C. Bohm, and J. Perrin, Rev. Sci. Instrum. **64**, 31 (1993).

[12] Y. Wang, Y. Zhao, A. Qayyum, and G. Xiao, Nucl. Instr. Meth. B **265**, 474 (2007).

Chapter 4

Measurement of Fluorine Atom Densities and Their Impacts on Highly Selective Etching of SiOCH Films over SiC in Negative DC Bias Superposed Dual Frequency Capacitively Coupled *c*-$C_4F_8/N_2/Ar$ Plasma

4.1 Introduction

Reactive ion etching using a capacitively-coupled-plasma (CCP) is widely used for ultra large-scale integrated circuit (ULSI) fabrication [1]. It is necessary to realize high performance properties of etching, such as anisotropic etching with a high aspect ratio, and high etch rates with selectively etched films against mask materials of photo-resist and the underlying materials. In a conventional CCP, two parallel-plate type electrodes with individually applied radio-frequency powers to each electrode are used. This type of reactor is named “dual frequency CCP” [2]. Here, one of the electrodes, lower electrode, is used to set up a wafer and the counter electrode (upper electrode) is powered for plasma generation. Both the electrodes build up a self-bias voltage in ion sheath in front of the electrode surface. We have examined the superposition of a negative dc voltage to the upper electrode.

The superposition of a negative dc voltage to the lower electrode in

parallel-plate type CCP was first reported in the 1990s [3]. Recently, several researchers reported their computational results that the sheath structure is superposed electromagnetically by a dc sheath and an rf sheath when the negative dc voltage is applied to the electrode [4-8]. It has been experimentally recognized that the sheath voltage is modulated by this superposition, and the bombardment of ions accelerated by the high sheath voltage will enhance the generation of secondary electron emission [8]. The electrons generated on the electrode surface are accelerated into the plasma, thereby increasing the plasma density [4-8].

Nagai *et al*. reported that the secondary electrons injected from the top electrode driven by two superposed frequencies of 450 KHz and 13.56 MHz were accelerated by the sheath and suppressed the micro-trenching at deep trench bottom due to the relaxation of positive charge on the trench bottom by high energetic electrons [9]. Thus the highly energetic secondary electrons improved the etching properties. Very recently, Wang and Kushner reported plasma etching of SiO_2 in a dc-augmented CCP using a *c*-C_4F_8/O_2/Ar gas mixture. Their computational results showed that improvements for randomly occurring divergence of hole or trench shapes from the vertical were obtained by impinging highly energetic secondary electrons onto the lower electrode surface [10, 11]. They did not, however, report any experimental results, snd only computational results were shown. Thus, any effects of the dc-superposition need to be analyzed and experimentally demonstrated.

Fluorocarbon plasmas are used for the selective etching of low dielectric constant (low-*k*) films, such as carbon-doped silicon oxides (SiOCH), with respect to copper diffusion barrier films, such as carbon-doped amorphous silicon (SiC), in the fabrication of copper dual damascene interconnects in ULSI devices. Improvements in

variability and uniformity have been inevitable issues for a large-diameter wafer processing, and hence selective etching of SiOCH over SiC is necessary. Since the dielectric properties of SiOCH films are degraded by the carbon depletion of SiOCH films during the exposure to an oxygen-containing plasma, feed gases without oxygen such as a mixture of *c*-C_4F_8/N_2/Ar gases is needed for this application [12-16].

Additionally, in the case of highly selective etching of insulating materials such as silicon dioxide (SiO_2) and SiOCH in a dual-frequency-CCP, behaviors of fluorocarbon radicals and F atoms influenced the selectivity considerably. In particular, in order to control F atom densities, the Si material has been usually employed as the upper electrode, where F atoms were consumed resulting in forming silicon fluorides [17-19]. For investigation of such actual processes, absolute densities of fluorocarbon radicals have been measured using laser diagnostics tools and relative densities of F atoms have been estimated using the actinometrical technique with optical emission spectroscopy (OES) [17-19]. However, it has been well known that the actinometrical technique was never able to be applied to the plasma when the electron temperature was varied. Therefore, the behaviors of absolute densities of F atoms in the dual frequency fluorocarbon gas CCP have never been understood under the conditions of highly selective etching. Therefore, it is crucial to develop a setup for measuring the absolute density of F atom in the production level reactor which is used for actual etching process.

In this study, we focused on the mechanism of selective etching of SiOCH over SiC under c-C_4F_8/N_2/Ar plasma chemistry by using dual frequency CCP with a superposed negative dc voltage. The novel diagnostics setup to measure the absolute densities of F and N atoms was developed by using a vacuum ultraviolet absorption

spectroscopy (VUVAS). We carried out the measurements of bulk plasma parameters such as plasma density, atom densities of N and F and radical densities of CF and CF_2 systematically for the dc superposition CCP, and compared the results with those for the conventional dual-frequency CCP without the dc-superposition. Then we discussed the mechanism of the selective etching of SiOCH over SiC.

4.2 Experimental setup

All the experiments were carried out using a commercially available dual frequency capacitively-coupled-plasma reactor, as shown schematically in Figure 4.1. The reactor can process 300 mm diameter wafers. In the conventional CCP setup, VHF (60 MHz) power is applied to the upper electrode made of silicon and sustained plasma discharge. The temperature of the upper electrode and side wall were maintained at 60 °C by circulating a temperature-control coolant. Radio frequency (13.56 MHz) power was applied to the lower electrode to control the energies for ion-bombardment onto the samples. A 300 mm wafer was electrostatically chucked on the stage, which was cooled to a temperature of 20 °C. In the case of dc-superposition, a dc bias was simultaneously applied to the upper electrode. The highest dc bias was -1200 V. A mixture of Ar, N_2 and c-C_4F_8 gases with flow rates of 800, 100, and 10 sccm, respectively, were introduced into the chamber through the shower-head of the upper electrode and maintained at a pressure of 5.3 Pa by an automatic pressure controller. The gap between the electrodes was 35 mm. The typical processing time was 60 s. Blanket SiOCH and SiC films deposited on the 300 mm wafers were used as samples. The SiOCH film was prepared by a spin-on coating method with a thickness of 500 nm. Initial dielectric constant of the SiOCH was about 2.4. The SiC film was prepared by

plasma enhanced chemical vapor deposition with a thickness of 200 nm and dielectric constant of 4.2. The thicknesses of both SiOCH and SiC films were measured before and after etching the samples, by using a spectroscopic ellipsometer (J. A. Woollam, M-2000). The etch rates was calculated from the etch depths and selectivity was estimated from the etch rate for each film.

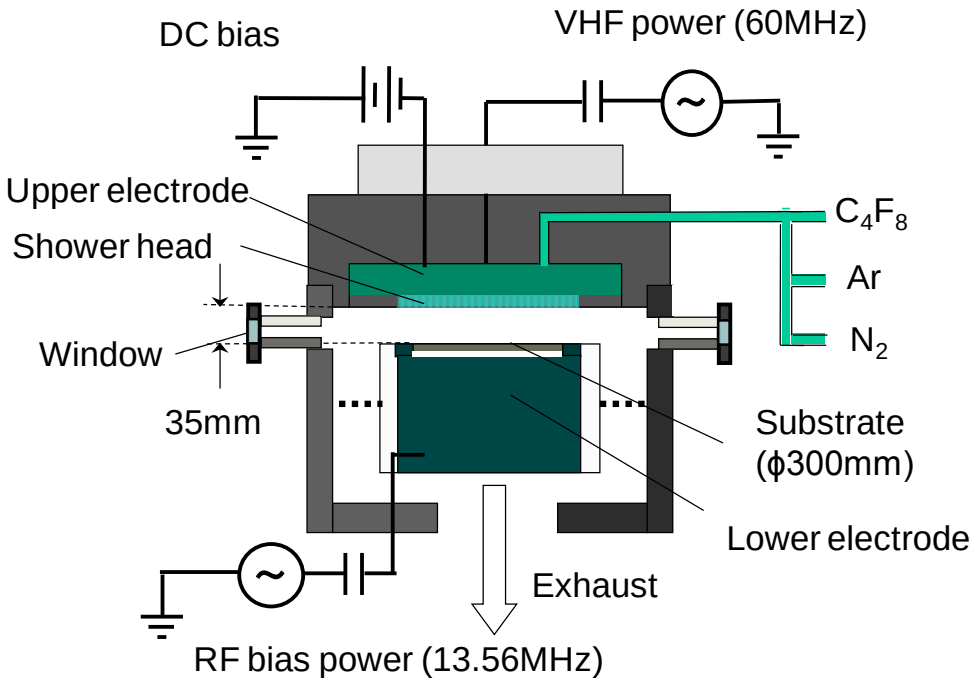

Figure. 4.1 Schematic of dual-frequency CCP reactor.

The electron density was measured by using a plasma absorption probe (PAP), which enables measurements even when the probe surface was soiled with deposited fluorocarbon film [20]. The PAP used was a coaxial cable enclosed with a quartz tube (dielectric constant ε=3.78). This quartz tube probe was inserted through the chamber-wall to the center of the chamber. The measurement location was 12 mm above the surface of the lower electrode. During the plasma discharge, the resonant absorption spectra ranging in the GHz region were measured by a network analyzer

(Agilent E5071C). According to the plasma dispersion relationship, the surface wave resonance frequency f_{sw} is proportional to the square-root of the plasma density, n_e. Although there were reports for the validity of its application to the plasma density measurements [6,20,21], we also measured the the electron density using a laser Thomson scattering [22]. These results were used for the calibration of those of PAP. Consequently, the plasma density was estimated from the following relation,

$$n_e = 1.24\times10^{10}(1+\varepsilon)f_{SW}{}^2 \tag{4.1}$$

where f_{sw} is $\omega_{SW}/2\pi$ in units of GHz and ε is 3.78, the dielectric constant of a quartz tube, because the deposited film is negligibly thin. The proportional constant given here strongly depends on the probe geometric arrangement. Here, it was assumed that the electron energy distribution in the low energy region with abundant electron density was not influenced by the superposition of negative dc bias. However, in the higher energy region, the electron energy distribution might be changed because the secondary electrons were accelerated and injected into the bulk plasma [3, 4]. Bulk electron densities for the plasma generated with or without the dc-superposition were measured and compared in this study.

Using a Laser Induced Fluorescence (LIF) spectroscopic method, the densities of CF and CF_2 radicals were measured. The output excitation light of a dye laser pumped with pulsed XeCl laser radiation passed through the center of the chamber and 7 mm above the surface of the substrate. Fluorescence light was detected at the center of the chamber at right angles to the excitation laser beam using an intensified charge-coupled device (ICCD) camera with a band-pass filter. For detection of the CF radical, the output of the dye laser was tuned at 232.66 nm ($A\ ^2\Sigma^+$-$X\ ^2\Pi$ (0, 0)), and

fluorescence at 255.2 nm (A $^2\Sigma^+$-X $^2\Pi$ (0, 3)) was observed. In the case of the CF_2 radical, the excitation of 261.7 nm (A (0,2,0)-X (0,0,0)), and fluorescence at 271.0 nm (A (0,2,0)-X (0,2,0)) were used. Since the detected signals were overlapped with the plasma emissions, the fluorescence signal of the radical was evaluated by subtracting the plasma emission signal. By comparison with the absolute density obtained by single path infrared laser absorption, absolute radical densities were calculated from the fluorescence signal intensity.

Plasma optical emissions were measured at the position identical with the LIF measurements by a spectrometer with spectral resolution of 0.023 nm (Acton Research, ACT-300). In the OES measurement, emissions due to Ar at 703.025 nm and those due to F atoms at 703.747 nm were observed. In the case of N_2 diluted fluorocarbon gas plasmas described here, however, the band head of N_2 emissions located around706 nm was strongly observed. Therefore, it has been a great problem that the F atom density has never been estimated by using OES and those behaviors have never discussed in the present conditions. In this study, we have developed a novel technique to measure the absolute densities of atomic species.

Using VUVAS, the absolute density of the N and F atomic species were measured in a cell branched from the chamber wall. The cell was constructed using a T-port, with two ports used for a VUV monochromator and a light source, and mounted on the chamber wall as shown in Figure 4.2. The T-port and the light source were separated by inserting capillary plates, and the absence of plasma generation inside the T-port was ensured by shielding using a metal-mesh. The distance between the chamber wall and the absorption points was about 20 cm. The pressure in the T-port was equalized to that of the process chamber.

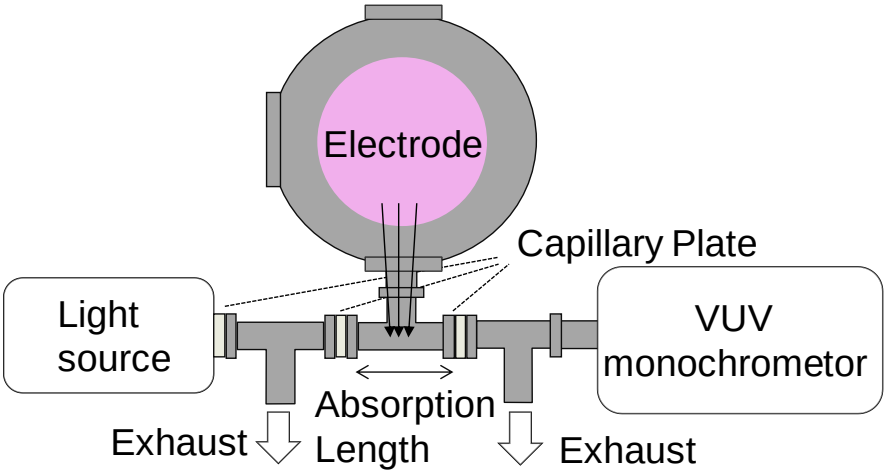

Figure. 4.2 Experimental setup for VUVAS system.

For measurement of N, we used a high pressure microdischarge hollow cathode lamp (MHCL) as a light source [22]. The absolute density of N radicals was measured by using the transitions of $2p^2\ 3s\ {}^4P_{5/2}\text{-}2P^3\ 4S^0{}_{3/2}$ at 119.95 nm, $2P^2\ 3s\ {}^4P_{3/2}\text{-}2p^3\ 4S^0{}_{3/2}$ at 120.02 nm and $2p^2\ 3s\ {}^4P_{1/2}\text{-}2p^3\ 4S^0{}_{3/2}$ at 120.07 nm. The absorption length was 15 cm. For measurement of atomic fluorine, we developed a setup utilizing another light source using an electron cyclotron resonance (ECR) plasma. The absolute density of the F radical was measured by using the transitions of $2p^4\ 3s\ {}^2P_{1/2}\text{-}2p^5\ {}^2P^0{}_{3/2}$ at 95.19 nm, $2p^4\ 3s\ {}^2P_{3/2}\text{-}2p^5\ {}^2P^0{}_{3/2}$ at 95.48 nm, $2p^4\ 3s\ {}^2P_{1/2}\text{-}2p^5\ {}^2P^0{}_{1/2}$ at 95.56 nm and $2p^4\ 3s\ {}^2P_{3/2}\text{-}2p^5\ {}^2P^0{}_{1/2}$ at 95.85 nm. The absorption length was 25 cm. Generally, in many cases in actual CCP etching processes, atomic fluorine density is too low to be detected from its optical emissions; so it is noteworthy that the VUVAS measurement for absolute F density was essentially useful for analyzing the plasma parameters. The chemical components of surfaces on SiOCH and SiC after etching were analyzed using an X-ray photoelectron spectroscopy.

4.3 Highly selective etching of SiOCH over SiC films

The etching properties of the dual frequency capacitively-coupled plasma superposed with a dc voltage to the upper electrode were investigated. In the conventional CCP, a VHF power of 800 W was applied to the upper electrode and an rf power of 1500 W was applied to the lower electrode. In this condition, without the negative dc superposition to the upper electrode, the etch rate for the SiOCH film was 100 nm/min and that for the SiC film was 18.5 nm/min; consequently, the selectivity for the etching of SiOCH over SiC was only 5.5.

Negative dc voltages were applied to the upper electrode together with the VHF power. As the negative dc voltage was changed from 0 to -1200 V, we observed that the etch rates for both SiOCH and SiC were modulated, as shown in Figure 4.3. In this condition, a self biased voltage (Vdc) of about -250 V on the upper electrode was built up by the VHF power. When the dc bias voltage was lower than the Vdc, modulation in etch performance was not recognized. When the dc bias voltage exceeded the Vdc, the SiOCH etch rates decreased first and then gradually increased with increasing dc bias and reached 90 nm/min at -1200 V. On the other hand, the etch rate of the SiC film decreased monotonically with increasing the dc bias and reached 1.3 nm/min at -1200 V. Therefore, highly selective etching of SiOCH over the SiC films was realized with the -1200 V dc bias. The selectivity significantly improved up to 68.0, while it is 5.5 for the conventional CCP without the dc bias. Since the dc voltage superposition contributed to increase the plasma density, as described in detail later, we examined the etching performance as a function of the VHF power. Figure 4.4 shows the etch rates of the SiOCH and SiC films as a function of the VHF power above 800 W without the dc bias. With increasing VHF power, the etch rate of the SiOCH film varied

slightly down and up. This behavior was similar in the case of the dc bias superposition. For a VHF power of 2000 W, the etch rate of the SiOCH film reached 90 nm/min. However, the etch rate variation of the SiC film were significantly different from the results for the dc bias superposition. The SiC etch rates remained almost constant at 18.5 nm/min, although the VHF power increased from 800 to 2000 W.

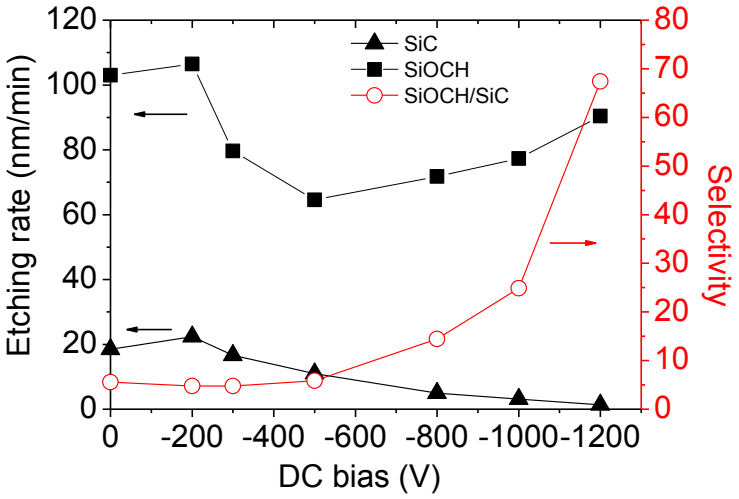

Figure 4.3 Etch rate of SiOCH (square) and SiC (triangle) films and selectivity of SiOCH over SiC etch rates (open circle) as a function of dc bias superposed to the upper electrode.

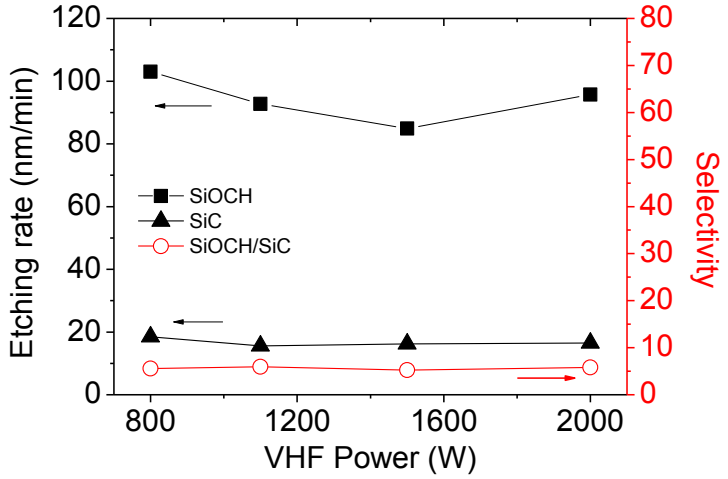

Figure 4.4 Etch rate of SiOCH (square) and SiC (triangle) films and selectivity of SiOCH over SiC etch rates (open circle) as a function of VHF power.

4.4 Electron density

For the investigating the mechanism of the selective etching mechanism described above, we conducted measurements of the plasma density when the negative dc voltage was superposed on the upper electrode. Kawamura *et al*. have reported simulation results for the characteristics of a superposed dc/rf sheath. They concluded that secondary electron emission from the surface of the electrodes significantly affected plasma parameters such as electron density and the electron energy distribution function (eedf) [3, 4]. Thus, the dependence of the electron density on the dc biasing was investigated using the plasma absorption probe (PAP). Figure 4.5 shows the electron density as a function of the dc bias under identical conditions as in Fig. 4.3. Under the condition without a dc bias, the electron density was 1.3×10^{11} cm^{-3}. As the negative dc bias increased up to -1200 V, the electron density reached 2.1×10^{11} cm^{-3}, almost twice as large value. These results experimentally demonstrated that the superposition of the dc bias increased the plasma density.

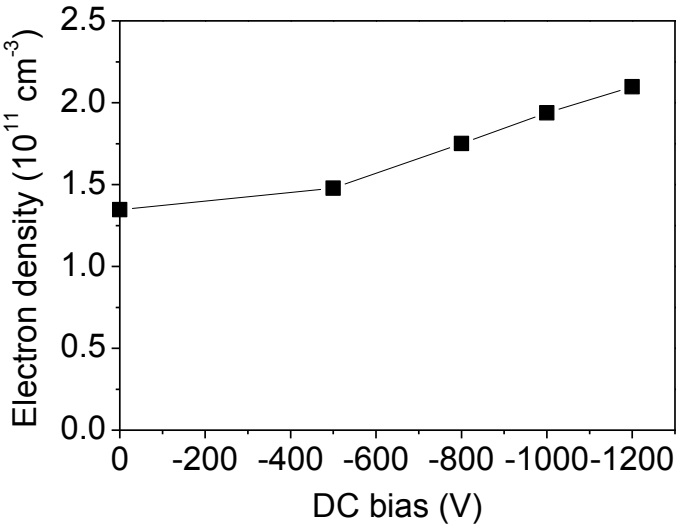

Figure 4.5 Dependence of electron density measured the PAP on the dc bias applied to the upper electrode.

In the case of dc biasing, the increase in the electron density mainly depends on the γ effect, wherein positive ion bombardment to the upper electrode surface increased by the dc bias application. Following the energy dependence of secondary electron emissions, the amount of secondary electrons increases as a result of augmentation of the negative dc bias, that corresponds approximately to the rise in ion bombardment energy [23, 24]. In fact, by applying the dc bias to the upper electrode, the dc current flow drastically increased. Figure 4.6 shows the dc current as a function of the negative dc bias. No significant dc current flow was observed at -200 V. When the applied dc bias was increased to -250 V that corresponded to the Vdc developed by the VHF power only, the dc current increased abruptly from 0.10 to 0.83 A. For Vdc exceeding -250 V, the dc current increased monotonically as if the secondary electron emissions increased with increasing ion bombardment energy. Thus, the dc current measurement indicated that the increase in dc current flow in the upper electrode arises from an increase of the ion bombardment energy due to the dc bias. Secondary electrons are generated by positive ion bombardment on the electrode, and are accelerated in the sheath and injected into the plasma. As a result, the electron density increases by the application of the dc bias.

Figure 4.7 shows the electron density as a function of the VHF power under the identical conditions as used in Fig. 4.4. The electron density monotonically increased to 2.3×10^{11} cm^{-3} when a VHF power up to 2000 W was applied. Notably, the SiOCH etch rate of 90 nm was obtained at the plasma density of more than about 2×10^{11} cm^{-3} for both conditions with the dc bias and the VHF power increasing.

As the electron density was increased, the peak-to-peak voltage (Vpp) of the lower electrode was decreased from 1480 V to 1000 V for the dc bias of -1200 V. In the

case of the same electron density with and without a dc bias superposition, both Vpp's indicated the same value. Therefore, the improvement in the selectivity by superposing a dc bias is also not explained by the difference in the ion bombardment energy which is correspondent to the Vpp. On the other hand, the SiC etch rate decreased as increasing the plasma density by dc bias application as shown in Fig. 4.3, while the SiC etch rate kept almost constant when increasing VHF power (Fig. 4.4). Thus, the SiC etch rate was not determined by phenomena induced by the increase of plasma density, such as the decrease of peak to peak voltage (Vpp) and/or the increase of the ion flux at the lower wafer electrode.

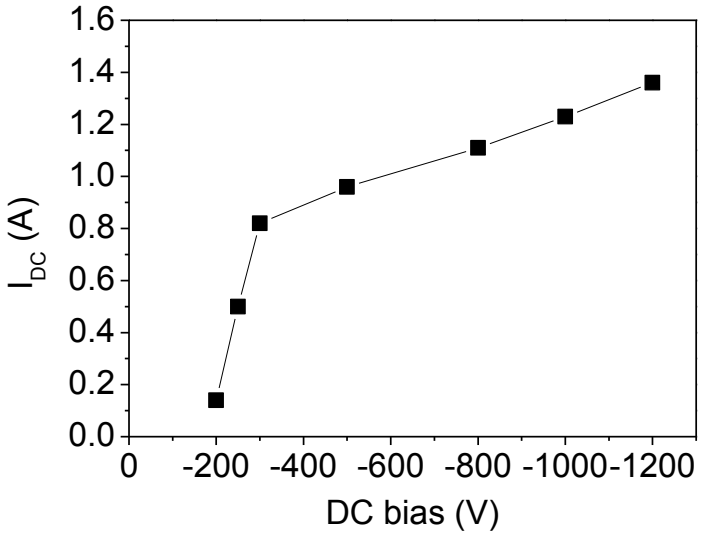

Figure 4.6 Dependence of dc current flow

through the upper electrode on superposed dc bias.

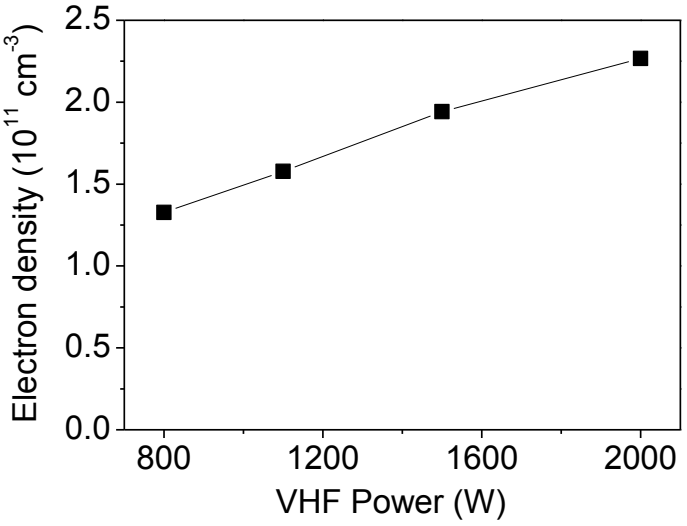

Figure 4.7 Dependence of electron density measured the PAP on the VHF power.

4.5 Atomic species and fluorocarbon radicals

We also measured the densities of gaseous chemical species such as N, CF, CF_2 and F in the plasma. Figure 4.8 and 4.9 show the densities of N atomic species as a function of the dc bias and VHF power, respectively. When the superposed dc bias was increased from 0 to -1200 V at a VHF power of 800 W, and similarly when the VHF power was changed from 800 to 2000 W with no dc-bias superposition, the N density increased from 6.0 to 8.5×10^{10} cm^{-3}. These increases of the N density simply corresponded to the increase of the electron density. The N radical is mainly generated from the dissociation of N_2 molecules by electron impact. Thus, the density of N increased in conjunction with enhanced electron-impact dissociation $e+N_2\rightarrow N(^4S)+N(^4S)+e$ and the dissociative ionization $e+N_2\rightarrow N^+ +N(^4S)+2e$ with increasing plasma density [25-27]. Meanwhile the gaseous recombination process of $N+N+M\rightarrow N_2+M$ with a reported a rate coefficient of $8.3\times10^{-34}\exp(500/T)$ cm^6/s [28] was negligible because of low pressure plasmas. Loss mechanisms were mainly considered to be recombination on the surface. Reported surface loss probabilities ranged widely as 9.3×10^{-5} for quartz, 0.0011 [29] for iron 3.2×10^{-6} [30] for Pyrex™ glass at temperature of 300 K, and 0.0075 [31], 0.03 for stainless steel [32]. Those surface loss probabilities were so low and the depletion of N_2 is negligible that it was considered that the density of N was simply determined by the plasma density.

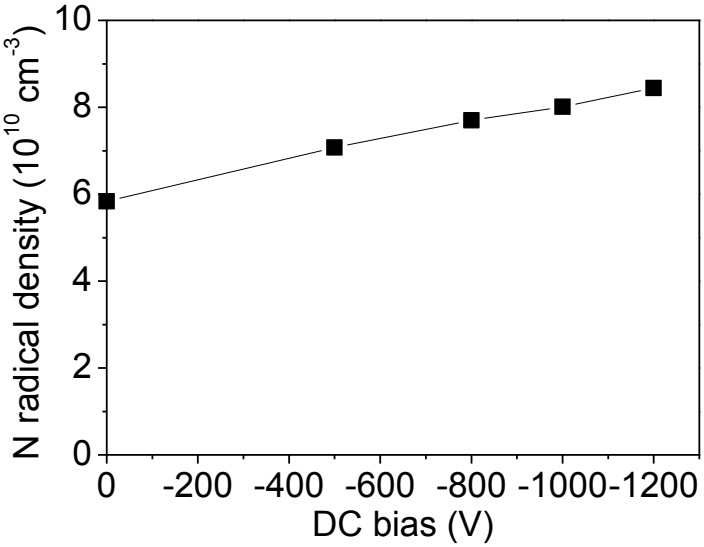

Figure 4.8 Dependence of the density of N radical

on the dc bias superposed to the upper electrode.

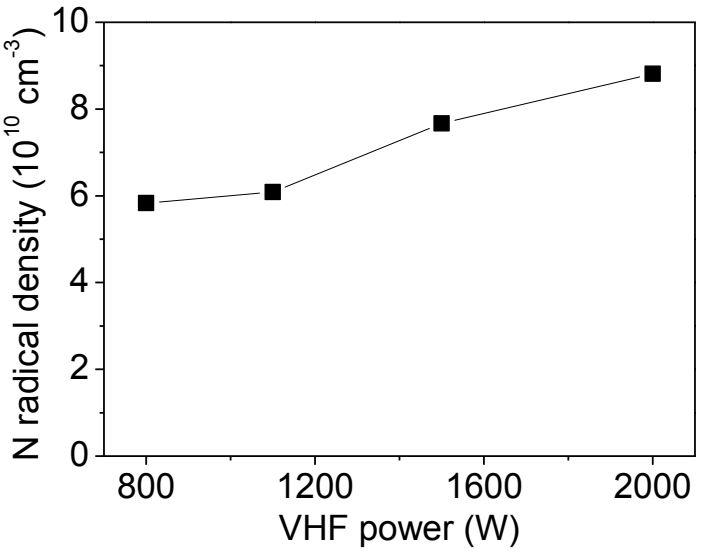

Figure 4.9 Dependence of the density of N radical on the VHF power.

Figure 4.10 and 4.11 show the CF and CF_2 fluorocarbon radicals as a function of the dc bias and VHF power, respectively. The densities of CF radical remained almost constant in spite of increased plasma density. However, it should be noted that the density of CF_2 radical showed a decrease when the dc bias was above 800 V; the decrease was about one third of the value without dc bias. This phenomenon will be discussed later. For the estimation of F atom denisty, we first conducted OES. Figures 4.12 and 4.13 show the OES spectra ranging between 695 and 705 nm. There were strong emissions from Ar and N_2, because the feed gas included Ar, N_2 in addition to *c*-C_4F_8. It was worth noting that all emissions due to F atoms were too low to be detected. Thus, the OES should not be employed for F atom density measurements of actual processing CCP for the selective etching of SiOCH over SiC.

Figures 4.14 and 4.15 show the densities of F atomic species as a function of the dc bias and VHF power, respectively. Finally, it was found out that F atom density of both plasma conditions was in the order of 10^{11} cm^{-3}. The behaviors of F atom density were considerably different in the case of dc-bias application compared to the increasing VHF power, even though the electron density increased similarly in both cases. For the dc-bias application, the density decreased from 1.3 to 0.5×10^{11} cm^{-3}, when the dc bias changed from 0 to -1200 V with 800 W of VHF power. In contrast, the F density naturally increased from 1.3 to 9.5×10^{11} cm^{-3} with increasing VHF power from 800 to 2000 W. From these experimental results, it is likely that this behavior in the F density can account for the improvement in the selectivity of SiOCH over SiC when the dc bias was applied.

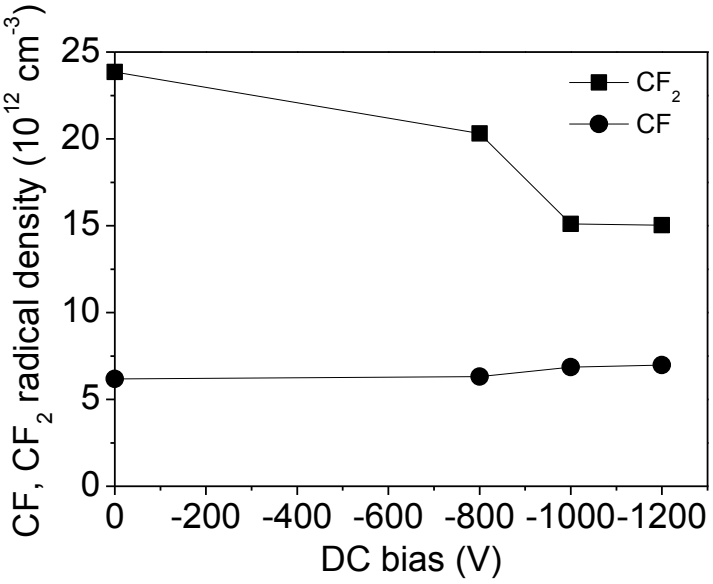

Figure 4.10 Dependence of the densities of CF (circle) and CF_2 (square) radicals on the dc bias superposed to the upper electrode.

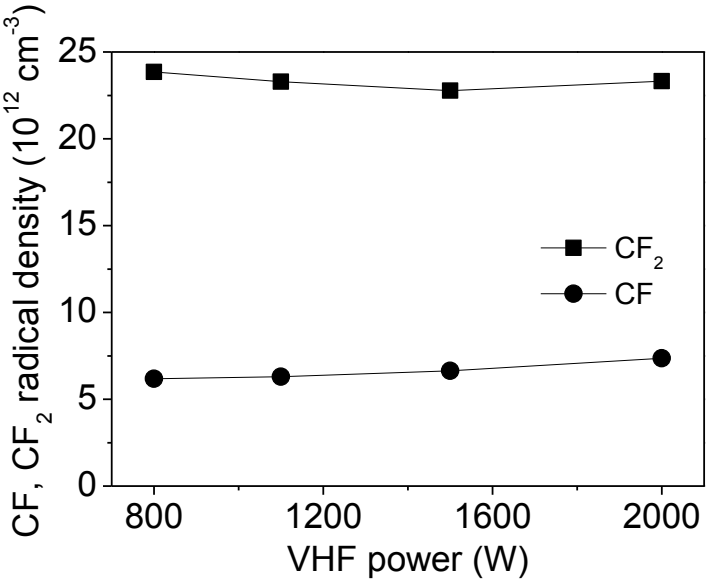

Figure 4.11 Dependence of the densities of CF (circle) and CF_2 (square) radicals on the VHF power.

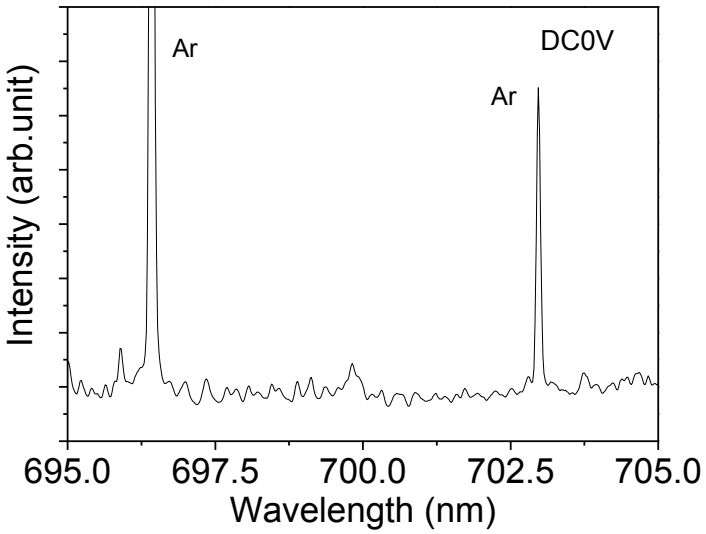

Figure 4.12 Optical emission spectrum for the plasma

without superposition to the upper electrode, i.e. with the dc bias of 0 V.

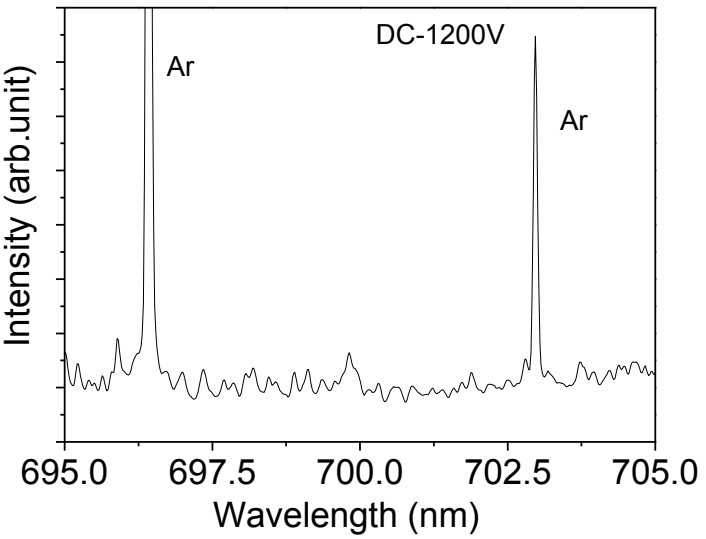

Figure 4.13 Optical emission spectrum for the plasma

with superposition to the upper electrode with the dc bias of -1200 V.

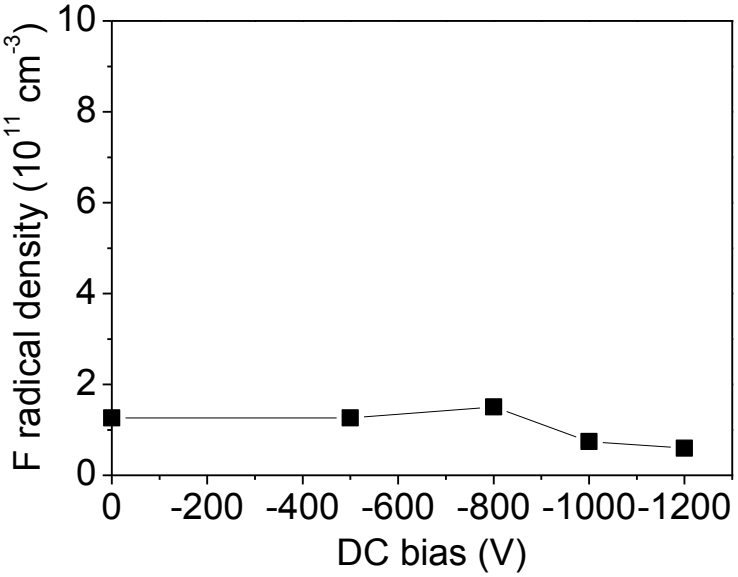

Figure 4.14 Dependence of the absolute density of F atom

at the T-port on the dc bias superposed to the upper electrode.

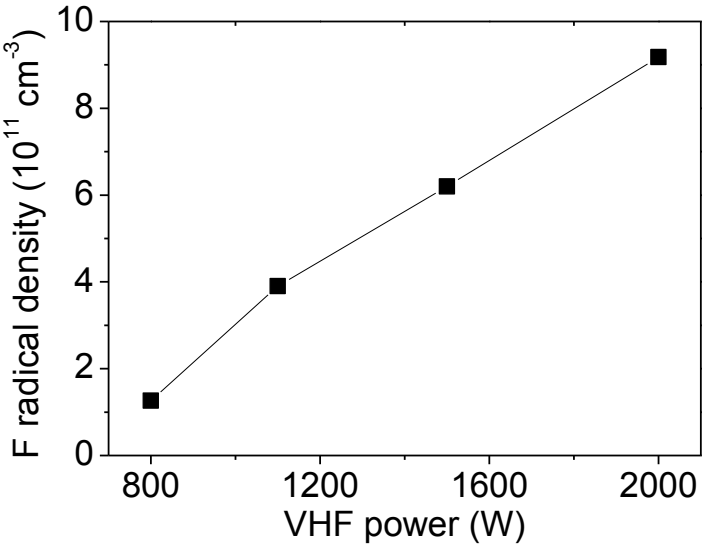

Figure 4.15 Dependence of the absolute density of F atom at the T-port on the VHF power.

To understand the behavior of the gaseous species densities, the balance between generation and loss was considered. For instance, the amount of CF_x radicals depends on the balance between the generation and loss in steady-state plasmas, is given as follows [17].

$$\frac{d[CF_x]}{dt} = [C_4F_8]n_e\langle\sigma v\rangle - \frac{[CF_x]}{\tau_{pump}} - \frac{[CF_x]}{\tau_{wall}} = 0 \tag{4.2}$$

where $[C_4F_8]$ is the density of *c*-C_4F_8, $[CF_x]$ is the density of CF_x radicals, n_e is the electron density, σ is the collision cross-section for dissociation, *v* is the electron speed, and τ_{pump} and τ_{wall} are time constants for the loss rate of the CF_x radical by pumping out and sticking to the walls. The blacket < > indicates averaging over the electron energy distribution function. τ_{wall} is given by [17]:

$$\tau_{wall} = \frac{S}{V}\frac{2s}{2-s}\frac{1}{4}[CF_x]\sqrt{\frac{8kT}{\pi M}} \tag{4.3}$$

where *V* and *S* stand for the gas plasma volume and surface area, while *k*, *T*, and *M* are the Boltzmann constant, the radical temperature and the mass of the radicals, respectively; *s* is the surface loss probability, which depends on the surface temperature and the incident ion flux on the wall surface.

As stated before, each density for the CF and CF_2 radicals was almost remained constant in spite of plasma density increasing with increasing the VHF power as shown in Fig. 4.11. Those radicals were generated by electron-impact dissociation of parent molecules [17,21,33], following the chemical dissociation such as *c*-$C_4F_8 \rightarrow C_2F_4 \rightarrow CF_2 \rightarrow CF \rightarrow F$. Thus, with increasing plasma density, the dissociation of the fluorocarbon radicals of CF and CF_2 was limited by the supply of the parent *c*-C_4F_8 gas as the source. As a result, the densities of the fluorocarbon radicals exhibited no dependence of plasma density. Similar experimental results have been reported by other

researchers [21, 34-38]. However, as an important point to be noted from these results, the density of CF_2 radicals was seen to decrease when a dc bias above 800 V were applied; it decreased to 1.5×10^{13} cm^{-3} for a dc bias of -1200 V.

In another aspect, the surface loss probability was reported by Suzuki *et al*.; 0.4 for CF and 0.06 for CF_2 [39]. Generally the CF radical were easily lost by surface recombination. Oppositely, since the CF_2 radical stays long-lived because of its lower surface loss probability. The CF_2 radical density was considered to be decreased by increasing surface loss probability with increasing energy incident ions on the reactor wall. Inayoshi *et al.* reported that the surface loss probability of the CF_2 radical increased with the creation of dangling bonds on the Si by ion bombardment [40, 41]. Likewise the surface loss probability was possibly increased when the dc bias was applied to the upper electrode. According to Eq. (4.2) and (4.3), the radical densities decreased with increasing surface loss probability. The density of CF_2 in the bulk plasma was decreased by adsorption and reaction on the upper electrode, because the formation of dangling bonds is promoted as the energy of the positive ions that bombard the electrode increases by the superposition of the dc bias. Moreover, the density of F in the bulk plasma decreased by chemical reactions with the Si of the upper electrode in the CCP etcher. The reaction $Si+4F\rightarrow SiF_4$ was enhanced with increasing energy of incident ions on the Si [18].

The CF radical density was considered to decrease by the recombination process with the N radical to generate the FCN molecule [42]. Three body associations are necessary for the recombination of the CF and N radicals; however, the recombination reaction would occur not in the gas phase, but on the electrode under the present conditions, because the mean free path is nearly 1 cm. It was considered that

recombination occurred on the surface of the electrodes more frequently than in the gas phase in the narrow gap plasma.

Summarizing our experimental results of the gaseous species, the densities of N and F were increased and the densities of CF and CF_2 were remained constant with increasing in plasma density. It should be noted that the densities of F and CF_2 had decreased only in the case of dc bias application process.

4.6 Surface reaction

To understand the surface reactions with gaseous chemical species, it is necessary to discuss the formation of a fluorocarbon (CF) polymer film working as an etch inhibitor. Since the SiOCH films contained oxygen, the CF polymer film was consumed to create both SiF_x and CO_x upon the ion bombardments, and the SiOCH films were etched [18, 43-46]. Thus the CF polymer film formed on the SiOCH was thinner than that on the SiC film. Namely SiOCH films were effectively etched by chemical sputtering (ion-assisted chemical reaction) under ion bombardment.

While N radicals are known to suppress the CF polymerization during the SiOCH etching by forming volatile HCN and C_2N_2 products [47,48]. In both plasmas with and without the dc-bias superposition, N atom densities increased with increasing electron density while etching rates of SiOCH were not increased monotonically. Therefore, it is considered that the influence of N atoms on etching rates are small in the present conditions. The SiOCH etch rates were around 90 nm/min as shown in Figs. 4.3 and 4.4. They are not so high as the etch rate under the conditions with the high-flux energetic ion irradiation. Thus, it is considered that carbon-rich state was generated in the gas phase and the competitive reaction of CF polymer (an etch inhibitor) formation

and ion-assisted etch reaction should occur.

Figures 4.16 and 4.17 show C 1s region of XPS spectra for SiOCH and SiC etched under the same electron density with and without a dc bias superposition, respectively. These spectra for the SiOCH surface were comparable while that of the SiC surface were different with and without the dc bias superposition. The signal originated from CF_2 was clearly observed the surface of SiC and the signal intensity increased by the dc bias superposition. It is considered that the deficiency of F atoms in the dc-bias superposed CCP as shown in Fig.4.13 suppressed the etching of polymer films on the SiC. Meanwhile, the F atom acts as an etchant of both SiOCH and SiC films, and thus etch rates for both SiOCH and SiC films without the dc bias superposition might increase when F atom density increased. In fact, only the etch rate of SiC film in the dc bias superposition agree with the dependence of the etch rate on the F atom density.

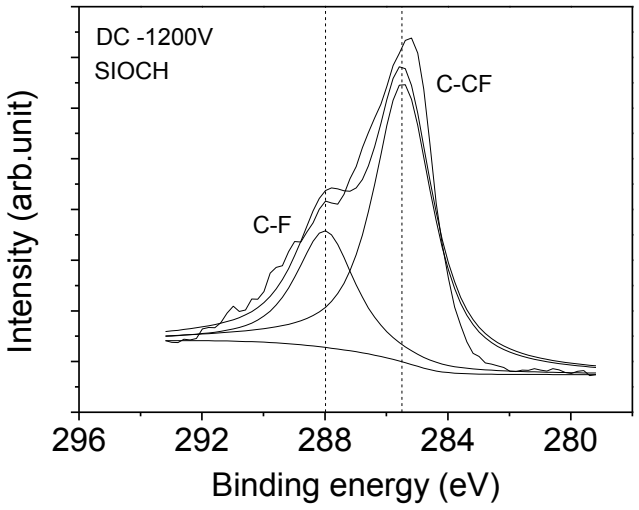

a)

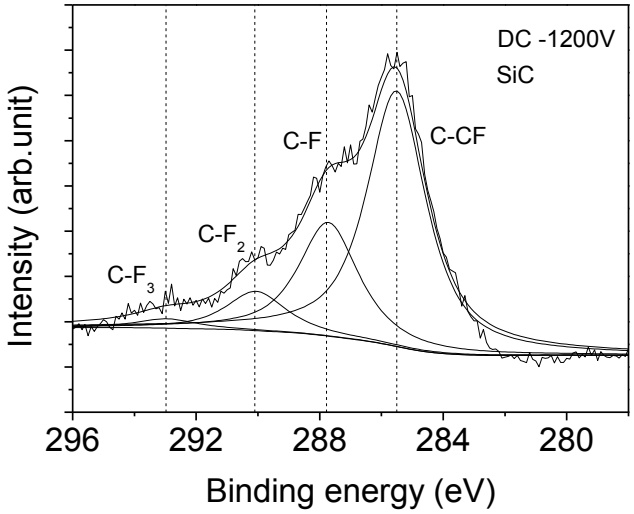

b)

Figure 4.16 XPS spectra of enlarged C 1s region

on surfaces of SiOCH (a), and SiC (b) after partially etched off

by the DS-CCP, i.e. with superposition of -1200 V to the upper electrode.

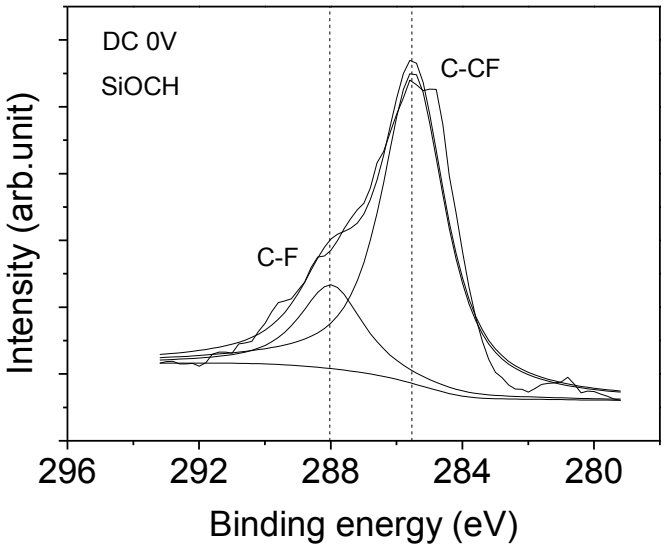

a)

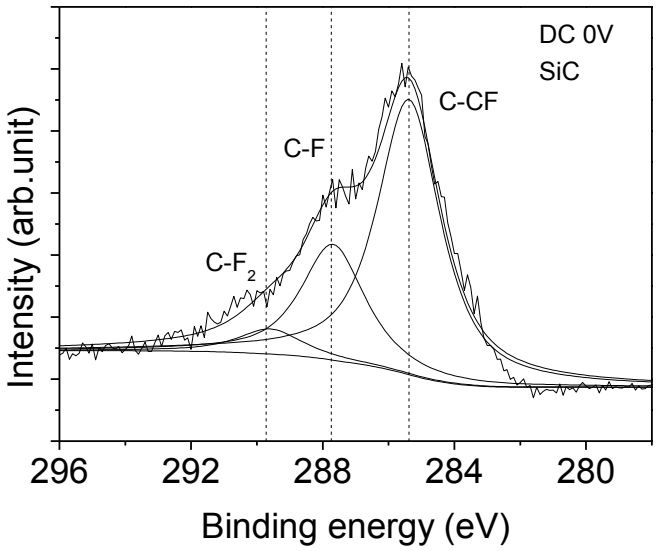

b)

Figure 4.17 XPS spectra of enlarged C 1s region

on surfaces of SiOCH (a), and SiC (b) after partially etched off

by conventional CCP, i.e. without superposition to the upper electrode.

It is speculated that because SiOCH film includes oxygen, deposition of fluorocarbon films are limited, where the oxygen included in the SiOCH film worked as etchant to reduce the fluorocarbon thickness and the etch rate was not reduced much [18, 43-46]. However, in the case of the SiC, only the F atom could etch the fluorocarbon film on the SiC by forming volatiles such as CFx. Furthermore, as the electron density increased by increasing the VHF power or dc-bias superposition, the ion flux density increased. These ion bombardments cause the interaction of radical species with SiOCH and SiC, resulting in enhancing the etching with F atoms or the carbon accumulation in the intermixing layers through the reaction with deposition species [49-51].

In this experiment, the etch rates both the SiCOH and SiC films did not have the significant dependence on CF_2 and CF radical densities and even though F and N atoms working as etchants increased by increasing the electron density, etching rates of SiOCH and SiC were not so much changed in the case of no dc bias superposition. Teii *et al.* reported that the carbon-rich plasma enhanced the higher-order radicals, which leads to the production of polymeric fluorocarbon species [52, 53]. Therefore, in the present condition, the higher order fluorocarbon species may contribute on the deposition. The decreasing in F atom densities will enhance further polymerization of fluorocarbon species on the surface. Then the etching rate of SiC will be decreased. Thus, the F deficiecy is considered to be the critical factor to reduce only the etch rate of the SiC.

Consequently, when F atom density could not suppress as in a conventional CCP [41], the flow rates of fluorocarbon feedstock gas mainly determines the etch rates of the SiOCH film. In applying the negative dc bias described herein, the F atom density efficiently became lower by F scavenging on the silicon counter electrode to which the

negative dc bias was applied, while the plasma density was enhanced by the secondary electron emission. To enhance the etching of SiC films, only the F atom contributed for the SiC etching and the reducing of fluorocarbon film formation. The densities of the CF_2 and F radicals decreased by moving the balance of the generation and loss of radicals. The loss rate of the radicals were enhanced by radical consumption at the surface of the upper electrode made of silicon. In other words, under the superposition of the negative dc bias, bulk densities of species such as CF_2 and F reduced by enhancing the surface loss under highly energetic ion bombardment. Those were the mechanism of improving selectivity the SiOCH over SiC films.

4.7 Conclusions

Dual frequency, capacitively-coupled plasma (CCP) with superposed negative dc bias is an indispensable technology to realize selective etching of the interlayer dielectric SiOCH against the underlying barrier dielectric, SiC. This technique significantly improved selectivity of the etching of SiOCH over SiC to 68.0 when a dc bias of -1200 V was superposed, compared to conventional CCP which shows a selectivity of only 5.5.

For clarification, we carried out experiments for measuring the absolute densities of gaseous chemical species such as N, F, CF, and CF_2 of the mechanism for the above phenomena. The densities of N and CF increased in conjunction with enhanced electron-impact dissociation, and conversely the densities of F, regarded as SiC etchants, decreased because by superposition of the negative dc bias, the surface loss for CF2 and F is enhanced under highly energetic ion bombardment. It is notable that the control of the bulk gaseous radical densities is feasible by utilizing application

of a negative dc bias to the counter electrode: secondary electron emissions at the surface of the electrode contributed to the increase in the plasma density; dissociation of parent gases or molecules accelerated the generation of radicals in conjunction with enhanced electron-impact; also, it enabled shift of the balance of generation and loss of radicals which is caused by modification of the surface loss on the counter electrode made of silicon.

Reference

[1] H. Abe, M. Yoneda, and N. Fujiwara, Jpn. J. Appl. Phys. **47**, 1435 (2008).

[2] M. Sekine, Appl. Surf. Sci. **192**, 270 (2002).

[3] K. Kohler. J. W. Coburn, D. E. Horne, E. Kay, and J. H. Keller, J. Appl. Phys. **57**, 59 (1985).

[4] E. Kawamura, M. A. Lieberman, A. J. Lichtenberg, and E. A. Hudson, J. Vac. Sci. Technol. A **25**, 1456 (2007).

[5] E. Kawamura, A. J. Lichtenberg, and M. A. Lieberman, Plasma Sources Sci. Technol. **17**, 045002 (2008).

[6] K. Denpoh and P. L. G. Ventzek, J. Vac. Sci. Technol. A **26**, 1415 (2008).

[7] P. L. G. Ventzek, and K. Denpoh, J. Vac. Sci. Technol. A **27**, 287 (2009).

[8] L. Xu, L. Chen, M. Funk, A. Ranjan, M. Hummel, R. Bravenec, R. Sundarajan, D. J. Economou, and V. M. Donnelly, Appl. Phys. Lett. **93**, 261502 (2008).

[9] M. Nagai, M. Hori, and T. Goto, Jpn. J. Appl. Phys. **43**, L501 (2004).

[10] M. Wang, and M. J. Kushner, J. Appl. Phys. **107**, 023308 (2010).

[11] M. Wang, and M. J. Kushner, J. Appl. Phys. **107**, 023309 (2010).

[12] K. Yonekura, K. Goto, M. Matsuura, N. Fujiwara, and K. Tsujimoto, Jpn. J. Appl. Phys. **44**, 2976 (2005).

[13] X. Hua, X. Wang, D. Fuentevilla, G. S. Oehrlein, F. G. Celii, and K. H. R. Kirmse, J. Vac. Sci. Technol. A **21**, 1708 (2003).

[14] L. Ling, X. Hua, L. Zheng, G. S. Oehrlein, E. A. Hudson, and P. Jiang, J. Vac. Sci. Technol. B **26**, 11 (2008).

[15] H. Nagai, Y. Maeda, M. Hiramatsu, M. Hori, and T. Goto, Jpn. J. Appl. Phys. **42**, L326 (2003).

[16] M. Nagai, T. Hayashi, M. Hori, and H. Okamoto, Jpn. J. Appl. Phys. **45**, 7100 (2006).

[17] H. Hayashi, S. Morishita, T. Tatsumi, Y. Hikosaka, S. Noda, H. Nakagawa, S. Kobayashi, M. Inoue, and T. Hoshino, J. Vac. Sci. Technol. A **17**, 2557 (1999).

[18] H. Hayashi, M. Okigawa, S. Morishita, and M. Sekine J. Vac. Sci. Technol. A **17**, 2517 (1999).

[19] T. Tatsumi, Appl. Surf. Sci., **253**, 6716 (2007).

[20] H. Kokura, K, Nakamura, I. P. Ghanashev, and H. Sugai, Jpn. J. Appl. Phys. **38,** 5262 (1999).

[21] K. Ishikawa, S. Hayashi, and M. Sekine, J. Appl. Phys. **93**, 1403 (2003).

[22] S. Takashima, S. Arai, M. Hori, T. Goto, A. Kono, M. Ito, and K. Yoneda, J. Vac. Sci. Technol. A **19,** 599 (2001).

[23] C. Bohm, and J. Perrin, Rev. Sci. Instrum. **64**, 31 (1993).

[24] Y. Wang, Y. Zhao, A. Qayyum, and G. Xiao, Nucl. Instr. Meth. B **265**, 474 (2007).

[25] Y. Itikawa, M. Hayashi, A. Ichimura, K. Onda, K. Sakimoto, K. Takayanagi, M. Nakamura, H. Nishimura, and T. Takayanagi, J. Phys. Chem. Ref. Data **15**, 985 (1986).

[26] B. M. Penetrante, M. C. Hsiao, B. T. Merritt, G. E. Vogtlin, P. H. Wallman, A. Kuthi, C. P. Burkhart, and J. R. Bayless, Appl. Phys. Lett. **67**, 3096 (1995).

[27] P. C. Cosby, J. Chem. Phys. **98**, 9544 (1993).

[28] C. S. Moon, K. Takeda, S. Takashima, M. Sekine, Y. Setsuhara, M. Shiratani, and M. Hori, J. Appl. Phys. **107**, 103310 (2010).

[29] T. Belmonte, L. Lefevre, T. Czerwiec, H. Michel, and A. Ricard. Thin Solid Films **341**, 27 (1999).

[30] T. Yamashita, J. Chem. Phys. **709**, 4248 (1979).

[31] S. F. Adams and T. A. Miller, Plasma Sources Sci. Technol. **9**, 248 (2000).

[32] S. Takashima, K. Takeda, S. Kato, M. Hiramatsu, and M. Hori, Jpn. J. Appl. Phys. **49,** 076101 (2010).

[33] T. Hayashi, K. Ishikawa, M. Sekine, M. Hori, A. Kono, and K. Suu, to be submitted to Jpn. J. Appl. Phys.

[34] S. Hayashi, H. Nakagawa, M. Yamanaka, and M. Kubota, Jpn. J. Appl. Phys. **36**, 4845 (1997).

[35] S. Den, T. Kuno, M. Ito, M. Hori, T. Goto, Y. Hayashi, and Y. Sakamoto, Jpn. J. Appl. Phys. **35**, 6528 (1996).

[36] J. P. Booth, H. Abada, P. Chabert, and D. B. Graves, Plasma Sources Sci. Technol. **14**, 273 (2005).

[37] J. P. Booth, G. Cunge, P. Chabert, and N. Sadeghi, J. Appl. Phys. **85**, 3097 (1999).

[38] H. Singh, J. W. Coburn, and D. B. Graves, J. Vac. Sci. Technol. A **19**, 718 (2001).

[39] C. Suzuki, K. Sasaki, and K. Kadota, Jpn. J. Appl. Phys. **36**, L824 (1997).

[40] M. Inayoshi, M. Ito, M. Hori, T. Goto, and M. Hiramatsu, J. Vac. Sci. Technol. A **16,** 233 (1998).

[41] K. Takahashi, M. Hori, M. Inayoshi, and T. Goto, Jpn. J. Appl. Phys. **35**, 3635 (1996).

[42] K. Miyata, H. Arai, M. Hori, and T. Goto, J. Appl. Phys. **82**, 4777 (1997).

[43] T. E. F. M. Standaert, P. J. Matsuo, S. D. Allen, G. S. Oehrlein, and T. J. Dalton, J. Vac. Sci. Technol. A **17**, 741 (1999).

[44] X. Hua, C. Stolz, G. S. Oehrlein, P. Lazzeri, N. Coghe, M. Anderle, C. K. Inoki, T. S. Kuan, and P. Jiang, J. Vac. Sci. Technol. A **23**, 151 (2005).

[45] M.-S. Kuo, X. Hua, G. S. Oehrlein, A. Ali, P. Jiang, P. Lazzeri, and M. Anderle, J.

Vac. Sci. Technol. B **28**, 284 (2010).

[46] X. Hua, M.-S. Kuo, G. S. Oehrlein, P. Lazzeri, E. Iacob, M. Anderle, C. K. Inoki, T. S. Kuan, P. Jiang, and W.-L. Wu, J. Vac. Sci. Technol. B **24**, 1238 (2006).

[47] K. Kurihara, A. Egami, and M. Nakamura, J. Appl. Phys. **98**, 084907 (2005).

[48] K. Ishikawa, Y. Yamaoka, M. Nakamura, Y. Yamazaki, S. Yamasaki, Y. Ishikawa, and S. Samukawa, J. Appl. Phys. **99**, 083305 (2006).

[49] K. Ishikawa, K. Karahashi, H. Tsuboi, K. Yanai, and M. Nakamura , J. Vac. Sci. Technol. A **21**, L1 (2003).

[50] K. Karahashi, K. Yanai, K. Ishikawa, H. Tsuboi, K. Kurihara, and M. Nakamura, J. Vac. Sci. Technol. A **22**, 1166 (2004).

[51] K. Yanai, K. Karahashi, K. Ishikawa, and M. Nakamura, J. Appl. Phys. **97**, 053302 (2005).

[52] K. Teii, M. Hori, M. Ito, T. Goto, and N. Ishii, J. Vac. Sci. Technol. A **18**, 1 (2000).

[53] K. Teii, M. Hori, T. Goto, and N. Ishii, J. Appl. Phys. **87**, 7185 (2000).

Chapter 5

Spatial Distributions of Electron, CF, CF_2 Radical Densities and Gas Temperature in dc-Superposed Dual-Frequency-Capacitively-Coupled Plasma Etch Reactor Employing *c*-$C_4F_8/N_2/Ar$ gas

5.1. Introduction

Reactive ion etching employing a capacitively-coupled-plasma (CCP) is a key technology for the massive production of ultra large-scale integrated circuits (ULSIs) [1]. In the conventional parallel-plate typed reactors named dual-frequency CCP, two electrodes were individually powered with radio-frequency powers [2]. The one electrode was named the “lower electrode” which is used to hold a wafer and to add a biasing power, and the counter electrode was named the “upper electrode” which is used for generating plasmas. Currently, the power of very high frequency (VHF) of 60 MHz has been applied to the upper electrode for enhancing the electron density, and to keep the lower sheath potential on the electrode, compared RF power such as 13.56 MHz.

Recently, various kinds of frequency have been tried to be superposed on the upper and lower electrode to control the uniformity of electron and ion density, ion energy distribution and so on [3]. The multi-frequency supplied to the electrodes

enabled us to have the knobs for controlling the plasma parameters but the tuning operation became much complicated.

Most recently, high performances of etching and interesting behaviors of reactive species were reported as a result of the superposition of a negative dc voltage to the upper electrode with 60 MHz frequency [4]. The negative dc voltage superposition to the lower electrode in the parallel-plate type CCP was first reported in the 1990s [5]. Several researchers reported their computational results that the sheath structure became an electromagnetical superposition of a dc sheath and an rf sheath when the negative dc voltage was applied to the electrode [6-10]. The sheath voltage was modulated by this superposition, and the bombardment of ions accelerated by the high sheath voltage would enhance the generation of secondary electron emission [10]. The electrons generated on the electrode surface accelerate into the plasma, thereby increasing the plasma density [6-10]. In view of the distribution of plasma density, when only the VHF power was applied to the upper electrode with a diameter greater than 300 mm, the uniformity was limited by the standing-wave and skin effects [11-13]. To make plasma parameters uniform in the large diameter VHF CCP, it was suggested and attempted that the powered electrode was shaped as an electromagnetic lens [14, 15], and build in a cavity to focus the electric field on the center [16, 17]. In practice, those techniques were successful in improving the uniformity of plasma parameters. To clarify the mechanism of the improvement was strongly required.

Fluorocarbon plasmas are used for the selective etching of dielectrics such as silicon dioxide (SiO_2) and carbon-doped silicon oxides (SiOCH). In particular for the SiOCH films, carbon depletion in the SiOCH due to exposure to an oxygen-containing plasma degraded its dielectric properties. Therefore, to suppress the carbon depletion,

oxygen-free plasma should be applied for this purpose. So in this study, the plasma chemistry with a mixture of c-C_4F_8/N_2/Ar plasmas has been focused on [4].

Many researchers have paid attention to the spatial distribution of fluorocarbon radicals such as CF and CF_2. Usually, the laser induced fluorescence (LIF) method has been used to detect the densities for CF and CF_2 and their spatial distribution in processing discharges [18-21]. Takahashi *et al.* pointed out that the sticking coefficient of radicals on the wall surface was significantly influenced by the radical densities in the plasma while fluorocarbon films were deposited on the chamber wall [22]. Those phenomena were supposed to result in fluctuations of not only the uniformity of the films deposited on the substrate but also the repeatability of the processes. Thus, the clarification and control of the spatial distribution of radical densities in the plasma reactor have been indispensable for achieving the high performance in the plasma etching processing.

However, previous measurements of species in the etching reactor have been performed in home-made or their own reactors. There have not been many reports on measurements of species in a reactor suitable for practical use with a high etching performance. To strength a point, the information of the behaviors of species in the plasma reactors guaranteed with a production level will be so useful to clarify the kinetics of species from the scientific viewpoint. Therefore, it is necessary to measure the plasma parameters in production level plasma etch reactors.

In this study, we have measured for the first time the spatial distributions of the electron density by using plasma absorption probe (PAP), the absolute densities of CF and CF_2 radicals by using the LIF method, and the gas temperature of N_2 by using optical emission spectroscopy (OES) in a dual frequency capacitively coupled plasma

etch reactor employing a *c*-C_4F_8/Ar/N_2 mixture gas with negative dc bias superposition to 60 MHz VHF applied to the upper electrode.

5.2. Experimental setup

All the experiments were carried out using a commercialized dual frequency capacitively coupled plasma reactor, as schematically shown in Figure 5.1. Two parallel-plate type electrodes with radio-frequency powers individually applied to each were used. The reactor could process wafers with a diameter of 300 mm. VHF (60 MHz) power applied to the upper electrode made of silicon sustained the plasma discharge. Temperatures of the upper electrode and the side wall were maintained at 60°C by circulating a temperature-control coolant. A dc voltage of −1000 V was superposed to the upper electrode. Radio frequency (13.56 MHz) power of typically 1500 W was applied to the lower electrode to control the energies for ion-bombardment onto the samples. A 300 mm Si wafer was electro-statically chucked on the stage of the lower electrode, which was cooled to a temperature of 20°C. Helium gas was filled in backside of the wafer. At the outer part of the wafer, there were rim-like extensions made of Si and further a similar extension made of quartz covering the lower electrode. A mixture of Ar, N_2 and c-C_4F_8 gases with flow rates of 800, 100, and 10 sccm, respectively, was introduced into the chamber through a shower-head type inlet on the upper electrode. The pressure was maintained at 5.3 Pa by an automatic pressure controller. Under this condition, highly selective etching of SiOCH with a rate of about 73 nm/min over SiC film with a rate of about 3.1 nm/min was actually achieved as reported in detail elsewhere [4].

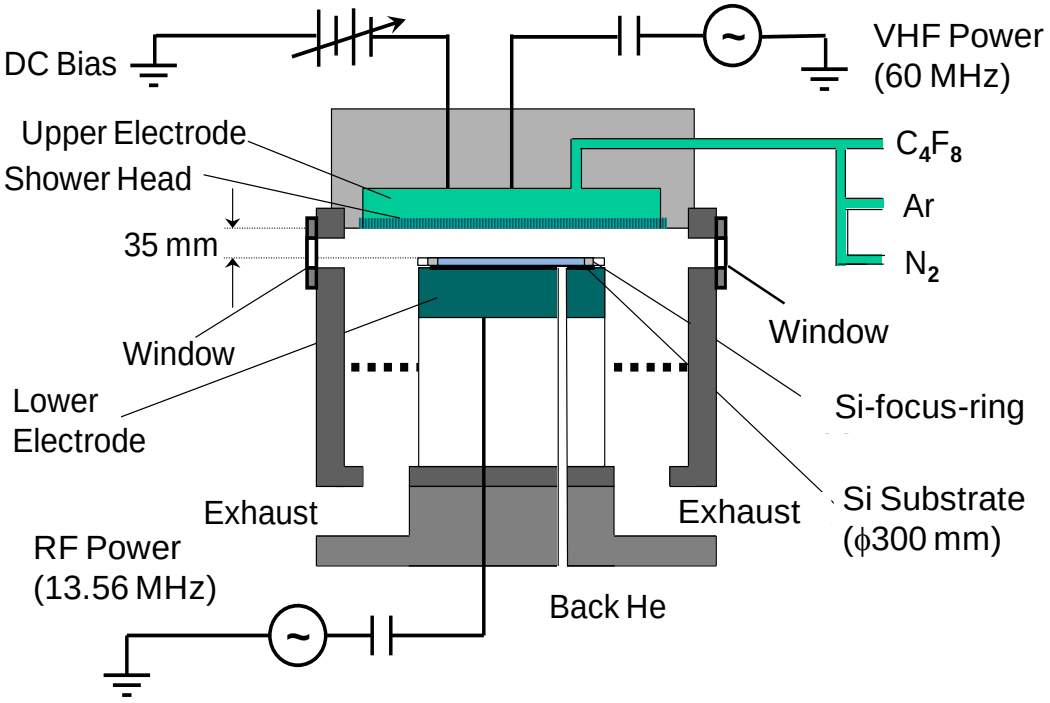

Figure. 5.1 Schematic diagram of our experimental setup with the dc-superposed df-CCP reactor.

Figure 5.2 shows a schematic diagram of the measurement setup. The electron density was measured by using a plasma absorption probe (PAP), which enabled measurements even when the probe surface was soiled with a deposited thick fluorocarbon film [23]. A coaxial cable was enclosed by a quartz tube (dielectric constant ε=3.78). This quartz tube probe was inserted through the chamber-wall to the center of the chamber. The measurement location was 12 mm above the surface of the lower electrode. During the plasma discharge, the resonant absorption spectra ranging in the order of GHz were measured by a network analyzer (Agilent E5071C). According to the plasma dispersion relationship, the surface wave resonance frequency f_{sw} is proportional to the square-root of the plasma density, n_e. There were reports for the validity of its application to the plasma density measurements [23-25]; a detailed information was given elsewhere [4].

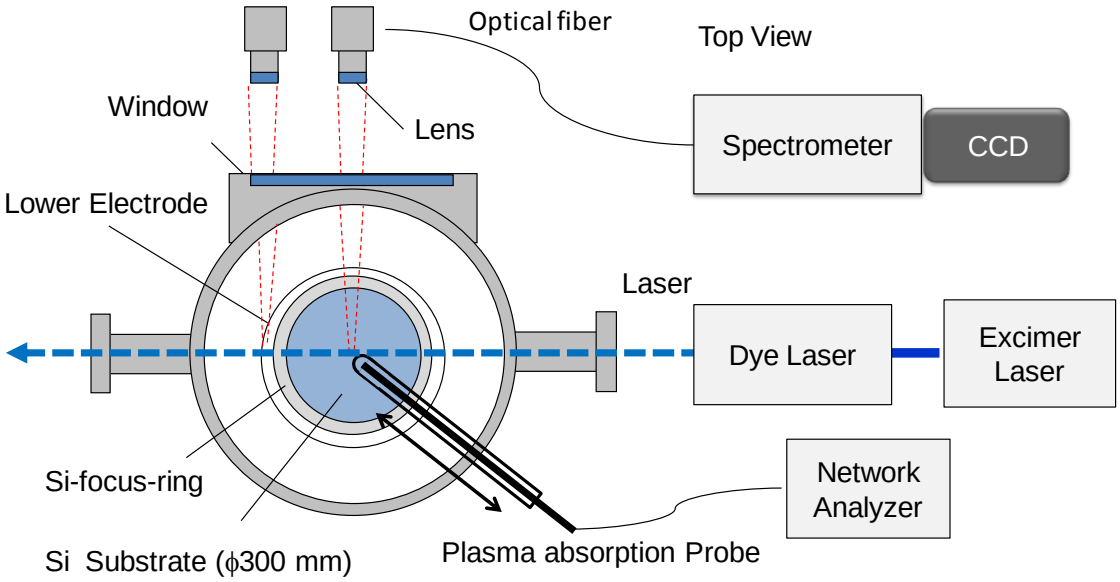

Figure 5.2 Schematic diagram of diagnostic setup for analyzing of the parameters for the CCP reactor with LIF, PAP, OES measurement system

The emission spectra of the N_2 (0-2) band located at around 308.5 nm were also measured during the processing. The measurement location was 7 mm above the surface of the lower electrode. The rotational temperature of N_2 molecule was analyzed by fitting the calculated emission spectra with assumption of Boltzmann distributions in rotational levels to that measured for the emissions around 308.5 nm arising from electronic transitions of $C^3\Pi_u$ - $B^3\Pi_g$ with vibrational band of (0-2) of N_2 molecule [26]. Usually the rotational temperature equilibrates with its kinetic temperature. Thus we considered the rotational temperature of N_2 molecule as regarded as the kinetics temperature. Spatial distributions of the optical emissions were obtained with focusing to and moving along centerline of the chamber. Here the spatial emissions were averaged profile, f(x), assuming cylindrical symmetry transform to a radial distribution, f(r), which was determined by the Abel inversion given by

$f(r) = \int_r^\infty \frac{\mathrm{d}\, f(x)}{\mathrm{d}\, x} \frac{1}{\sqrt{x^2 - r^2}} \mathrm{d}\, x$ [27]. Here we did not conduct at present the Abel

inversion of actual experimental results. At least, we confirmed that the spatial distribution shown in Fig. 5.5 was corresponded with truly radial distribution obtained by the Abel inversion. Thus simplified measured profiles where were fitted overlap of analytical functions such as Gaussian line-shape . The characteristic profile of temperature where represents the highest at the region above the silicon-ring (as described later and shown in Fig. 5.5) was corresponded with transformed results by the Abel inversion but exact radial distribution after Abel inversion of the measured profile could not performed due to erroneous.

The densities of CF and CF_2 radicals were measured by using the LIF method. The output of a dye laser pumped with pulsed XeCl laser radiation was used for excitation light and passed through the center of the chamber and 7 mm above the surface of the lower electrode. Fluorescence light was collected with a lens and transported through a fiber-optics to a spectrometer (Acton Research, Spectra Pro) during gated integration time for 100 ns just after excitation. Spatial distributions of the radical density were measured by moving the lens along the LIF excitation beam. The fluorescence light intensity was obtained by subtraction the background signal of the plasma emissions from the detected signals. For detection of the CF radical, the output of the dye laser was tuned at 232.66 nm wavelength in the transition A $^2\Sigma^+$-X $^2\Pi$ (0,0), and fluorescence at 255.2 nm in A $^2\Sigma^+$-X $^2\Pi$ (0,3) was observed. Absolute CF density was calibrated by comparing the LIF signal with that of known pressure of NO (nitric oxide) gas filled in the chamber [28]. In the case of the CF_2 radical, the excitation of 261.7 nm wavelength in the transition A (0,2,0)-X (0,0,0), and fluorescence at 271.0 nm in A (0,2,0)-X (0,2,0) were used [29]. Absolute CF_2 density was determined by fitting line-integrals of the LIF signals to the value obtained by the ultraviolet absorption

spectroscopy with a xenon lamp [30]. We noted that the heights of 12 mm for the plasma density and 7 mm for the radical density measurements were different due to instrumental limitations. Generally the plasma parameters might be nearly a constant in the region further from sheath edge. If we imagine that typical plasma density is the order of 10^{11} cm^{-3}, a sheath width becomes less than just the order of mm so that our measurement heights were possibly influenced not to change significantly both the densities [31]. However, for more detailed consideration, axial profiles are needed to include further discussion.

5.3. Results and Discussion

Figure 5.3 shows the distributions of electron density measured by the PAP. Applying the negative dc-bias of −1000 V, the spatial distribution for electron density represented to be uniform within radial position of 130 mm. At outer radial position of the monotonic decay of the density toward the chamber wall was observed. The results indicate that a profoundly good uniformity of electron density distribution over the wafer was realized for this superposed CCP reactor although the hollow distributions were frequently observed in a conventional CCP reactor. Therefore, the production of radicals through the electron impact dissociation is considered to be uniform spatially on the wafer within the radial position of 130 mm and decrease monotonically outside the position. According to this fact, the precise information for discussing the behaviors of radical densities has been needed to understand the mechanism to cause of spatial distributions scientifically with respect to the plasma parameters.

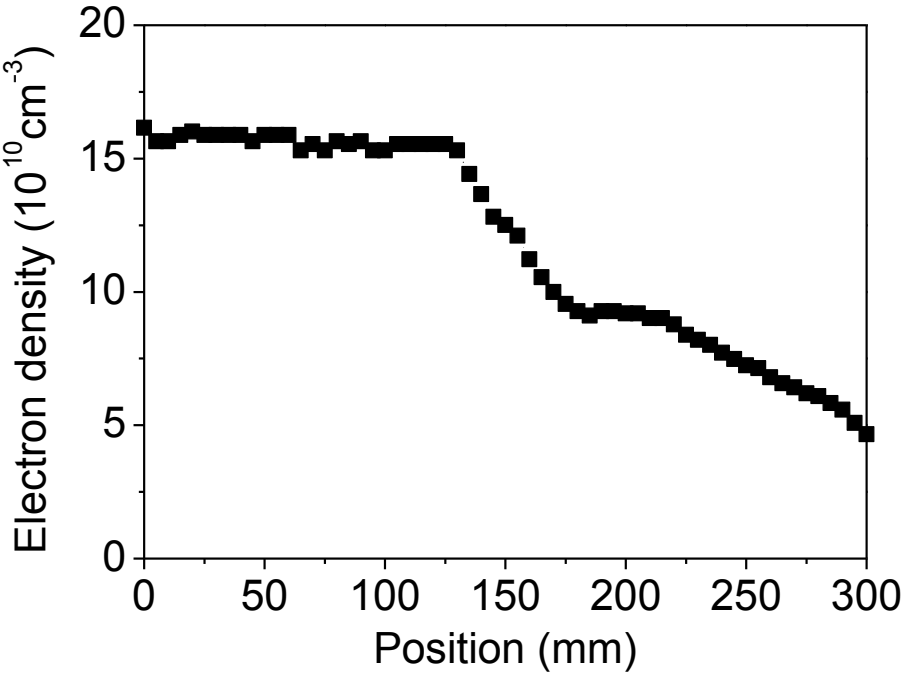

Figure 5.3 Spatial distributions of electron density of the CCP reactor during etch of the c-C_4F_8/N_2/Ar plasma with dc bias of −1000 V.

Figure 5.4 shows the spatial distribution of the absolute radical densities of CF_2 radicals by using LIF. The measured distributions of CF_2 radical density had nearly a constant value of about 1.3×10^{13} cm^{-3} at the inner region within the radial position of about 130 mm. Outside the uniform region, the density of CF_2 radical was decreased. As schematically shown in Fig. 5.1, at outside of the narrow gap region, the gap widen for evacuation. Since this conductance change may affect to the actual gas flow rate, the distribution of the CF_2 radical density is seemed to be explained by this geometric effect. However, it failed to explain due to differences in position where the radical density change with that of the end of the narrow-gap region. Notably, this almost corresponded to the behaviors of the plasma density distribution. Compared with the monotonic decay in the plasma density, the CF_2 radical density was characteristically dropped at radical

positions ranging 150 and 180 mm to about 3.0×10^{12} cm^{-3}. It was, however, found that the values were increased at the radial position at about 190 mm to about 3.0×10^{12} cm^{-3}, and then the CF_2 density was maintained this level toward the chamber wall.

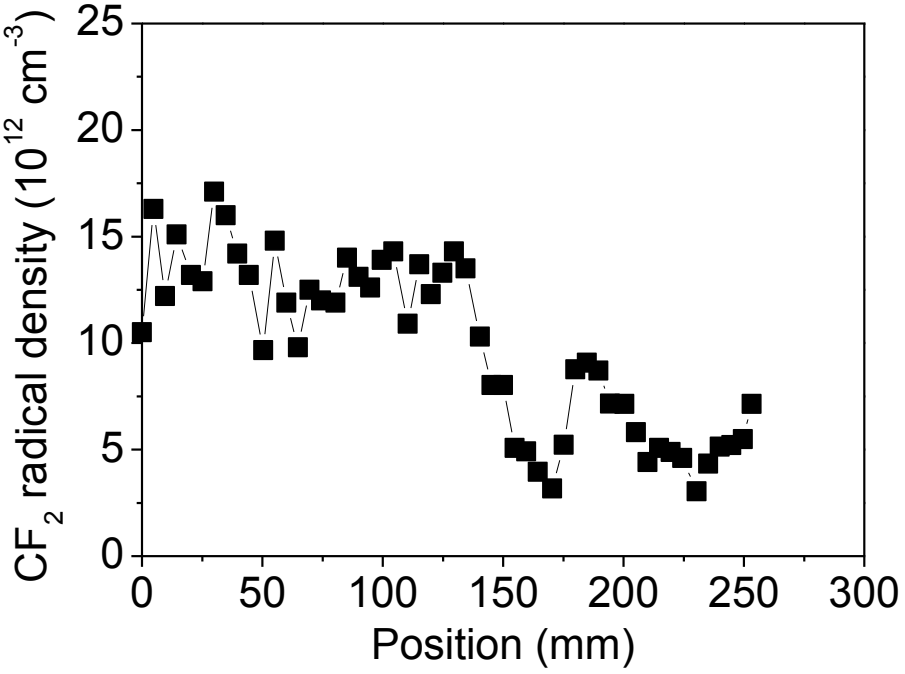

Figure 5.4 Spatial distributions of CF_2 radical density of the CCP reactor during etch of the c-C_4F_8/N_2/Ar plasma with dc bias of −1000 V.

To understand the mechanism of determining the radical densities and their distribution, balance between the generation and the loss was needed in consideration. First, the generation of radicals was significantly influenced by the dissociation process resulting from the electron impact [25,31,32]. Following this, the distribution of CF_2 radical would be represented any correlation with the electron density distribution. In our experimental results, except for the characteristic drop as described previously and discussed in details later, the distributions for plasma density and CF_2 radical density were almost agreed.

In publications with respect to electron-cyclotron-resonance (ECR) plasmas [18-20] and inductively-coupled plasmas (ICP) [21], their distributions were in many cases represented to be a hollow shape. They were rather inversely proportion to the plasma density. Namely, the radical density was increased toward the sidewall of the reactor. One of interpretations of the behavior has suggested that the CF_2 radical density is determined by a balance between generation and loss with respect to the reaction pathway of $C_4F_8 \rightarrow C_2F_4 \rightarrow CF_2 \rightarrow CF+F$ [31]. Although the CF_2 radical produced by electron-impact dissociation from the parent molecule on the whole plasma region, the produced CF_2 radical is lost by destruction into smaller fragments at the center rather than outside of the plasma [25]. The second one is that becomes sparse as a result of the increase in the gas-temperature when the plasma density was relatively high as of the order of 10^{11} cm^{-3}. Several researchers reported that the gas temperature became above 600 K [33]. Following simple estimate, the radical density drop is inversely proportion to the temperature rise. The last one is the generation from the reactor wall or by the recombination of CF with F in the gas phase at the periphery [29]. The larger molecules adsorb on the surface, and then energetic ion bombardment might produce CF_2 radical at the surface [34].

However, in cases of the CCP with a narrow gap between the electrodes, it is supposed to be a significant situation that the high-density plasma was confined in a small space between the electrodes so that the electron density was decreased toward of the reactor the sidewall under the depletion of C_4F_8 gas. Additionally, the production of CF_2 on the surface by the ion bombardment inside the electrode might be decreased as the electron density, that is, corresponding to the ion density was decreased outside of the electrode. Therefore, in the narrow-gap CCP, the CF_2 radical density distribution

corresponded to the plasma density distribution, namely, which was determined by the production process through the electron impact rather than the loss process.

As described before, the CF_2 density at radial distances from 150 to 180 mm dropped to a quarter value of the density at the center and the values at radial distances from 180 to 210 mm were increased again to a half value of that at the center. This characteristic drop position corresponded to the radial positions above the Si-focus-ring (radial position of 150 to 180 mm). This means that the drop occurred because of the Si-focus-ring. Although the wafer was cooled by chucking to the stage maintained at 20°C, the Si-focus-ring was not cooled but electrically connected the lower electrode. Due to plasma irradiation, the ring temperature was generally increased to values above 200°C, depending on the processing time and conditions [35]. Figure 5.5 shows the rotational temperature of N_2 molecule. Since the rotational temperature is regarded as in equilibrium with a kinetic temperature, the rotational temperature of N_2 molecule can be used to estimate the behavior of the gas kinetic temperature. At radial positions within 130 mm, the rotational temperature was about 530 K and uniform. (After the Abel inversion, this temperature may become less than 450 K. However the exact transform to the radial distribution is at present not conducted. More precise analysis will need to be performed.) It is noteworthy that the temperature at radial positions ranging between 150 to 180 mm, corresponding to the position above the Si-focus-ring, had higher values of about 630 K. This indicated that the Si-focus-ring was heated by plasma irradiations and then gas molecules above the ring was raised in temperature since their mean-free-path length was as low as mm range at the relevant pressure range.

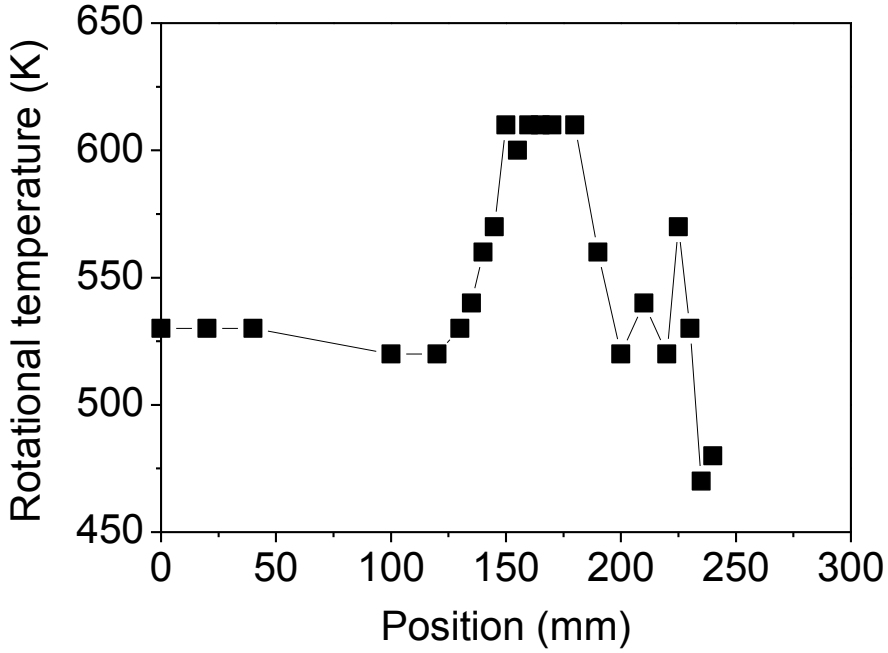

Figure 5.5 Spatial distributions of rotational gas temperature of N_2 molecule of the CCP reactor during etching in c-C_4F_8/N_2/Ar plasma with dc bias of −1000 V.

Following the result with respect to increase of the N_2 temperature, the CF_2 radicals above the ring were similarly heated and then the CF_2 radical density might become sparse to show lower densities. Compared with the actual density drop, this interpretation is not enough to fully explain because the density changes only 20% by considering the temperature rise. As stated before, in the narrow gap CCP case, the radical generation rather than loss is dominant. Namely, this indicates that surface reaction should be included with consideration. If the surface temperature increased, the chemical reaction would be enhanced. Thus the CF_2 radicals might react with the surface of the Si-focus-ring. This reaction made the surface loss probabilities, γ, rises. Based on the Milne boundary condition with $2\gamma/(2-\gamma)$, the bulk density, in particular close to the boundary, relates to the CF_2 outward flux [36]. As noted, the surface loss might also enhance by the energetic ion bombardment. If the surface loss probabilities

increase, then the bulk density decreases with almost inversely proportion. For example, if surface loss probability, which was reported the order of 0.01 for CF_2 [36], becomes 0.04, the density would decrease to quarter of the density. As not enough to prove completely, we believe that the density drop can be explained by the effect of rise in the loss-probability on the heated surface.

In outside the region where CF_2 radical density increases again as shown in Fig. 5.4, the surface loss process of CF_2 radical is considered to decrease due to the decrease in the electron density. In this outer region with low plasma density, the surface loss process of CF_2 radical would be decreased by since the surface is less activated because of less frequent ion bombardment and also the quartz surface has a lower surface loss probability. It was valid that the density of feedstock gas of C_4F_8 was also much depleted in the region due to dissociation in the central region, and thus the generation of CF_2 radical was limited and the surface loss process of CF_2 radical due to ion bombardment dominantly determined the density. As the results, the distribution of CF_2 radical increased again in that region. Consequently, the CF_2 radical acted as a long-lived radical inside the plasma, and the radical distribution was likely to be influenced by distribution of the plasma density and temperatures of surfaces and the supply of the parent gas.

Figure 5.6 shows the spatial distribution of the absolute radical densities of CF radicals by using LIF method. The measured distributions of CF radical density were nearly constant at about 7.0×10^{12} cm^{-3} in the whole radial positions to about 260 mm. As described above, following the result with respect to increase of the N_2 temperature, if it supported that the CF radical density should become sparse to show as similar as lower densities the CF radicals above the heated ring. This contradicted here the CF

radical density. Thus we preliminary believe that surface reaction with increase temperature affects to determine the bulk radical densities. In the other view, the absolute density of the CF radical at center position was lower than the CF_2 radical density. Since the main channel of generation of the CF radicals is considered to be the electron-impact-dissociation of the CF_2 radicals, the CF radical density should also correspond to the electron density distribution. However, the CF radical density distribution was considerably different from that of CF_2 radical density.

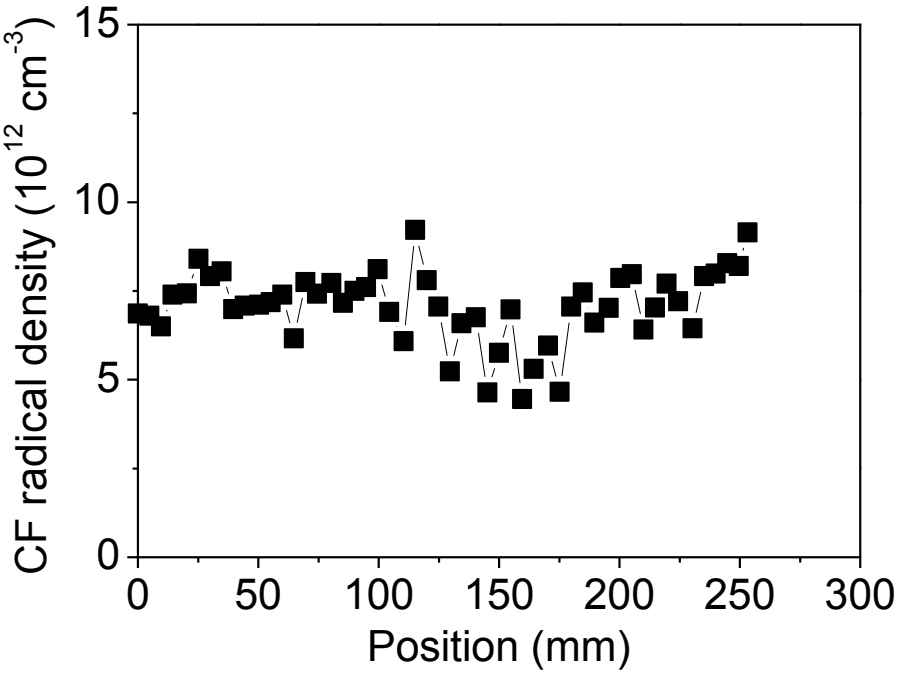

Figure 5.6 Spatial distributions of CF radical density of the CCP reactor during etch of the c-C_4F_8/N_2/Ar plasma with dc bias of −1000 V.

In previous studies, in cases of the ECR plasma and the ICP as mentioned before, it was reported that the CF density distributions were relatively flattened compared with that for the CF_2 radical. There were several interpretations with respect to this behavior. One was that the CF radicals have the high diffusion coefficients and

the high surface loss probability compared with the CF_2 radicals. Namely the CF radical generated in the uniform region in the plasma would be diffused rapidly to the outer regions and lost at the surface of the chamber wall.

In this study, the production of CF radical through the electron impact will be decreased by the decrease of CF_2 radical density as shown in Fig. 5.4 and electron density as shown in Fig. 5.3. However, the CF radical distribution became flat in the whole region. The production process should exist in the outer region. One possible mechanism is the decreasing of surface sticking loss on the heated Si-focus ring compared with that on the wafer surface.

Finally, on the basis of the present study using production-level etch reactor, we point out that the control of surface temperature and the design of the plasma reactor with appropriate material of the electrode are needed to obtain the uniformity of radical densities as well as the uniformity of gas temperature.

5.4. Conclusion

We investigated the spatial distribution of plasma parameters such as plasma density, gaseous temperature, and absolute CF and CF_2 radical densities in the dual frequency CCP with 60 MHz VHF superposed with negative dc bias. Applying a dc bias of −1000 V, the distribution of electron density was uniform within the radial position of about 130 mm. It was noteworthy that the spatial distributions of CF and CF_2 densities were also uniform in correlation with the uniform electron-density distribution. The measured CF and CF_2 radical density at the center were 7.0×10^{12} cm^{-3} for CF and 1.3×10^{13} cm^{-3} for CF_2. At positions above the heated surface of the Si-focus-ring, it evidenced for the ring temperature rise caused by temperature rise by plasma irradiation that the gas-temperature increase at least from about 530 K to about 630 K. Notably the

CF_2 radical density was dropped to one-fourth of the center value. This was interpreted due to increased surface-loss-probabilities at the reactive ring surface with energetic ion bombardment and temperature rise. Oppositely, the distribution of CF radical density was uniform across the whole region. Thus, the temperature and material in the plasma reactor should be property selected in order to obtain uniform distribution, since the CF_2 radical density was affected by modified surface-loss probability coupled with the surface temperature.

References

[1] H. Abe, M. Yoneda, and N. Fujiwara, Jpn. J. Appl. Phys. **47**, 1435 (2008).

[2] M. Sekine, Appl. Surf. Sci. **192**, 270 (2002).

[3] D. Sung, S. Jeoung, Y. Park, V. N. Volynets, A. G. Ushakov, and G. Kim, J. Vac. Sci. Technol. A **27**, 13 (2009)

[4] T. Yamaguchi, C. Koshimizu, S. Takashima, K. Takeda, H. Kondo, K. Ishikawa, M. Sekine and M. Hori: submitted to J. Appl. Phys.

[5] K. Kohler. J. W. Coburn, D. E. Horne, E. Kay, and J. H. Keller, J. Appl. Phys. **57**, 59 (1985).

[6] E. Kawamura, M. A. Lieberman, A. J. Lichtenberg, and E. A. Hudson, J. Vac. Sci. Technol. A **25**, 1456 (2007).

[7] E. Kawamura, A. J. Lichtenberg, and M. A. Lieberman, Plasma Sources Sci. Technol. **17**, 045002 (2008).

[8] K. Denpoh and P. L. G. Ventzek, J. Vac. Sci. Technol. A **26**, 1415 (2008).

[9] P. L. G. Ventzek, and K. Denpoh, J. Vac. Sci. Technol. A **27**, 287 (2009).

[10] L. Xu, L. Chen, M. Funk, A. Ranjan, M. Hummel, R. Bravenec, R. Sundarajan, D. J. Economou, and V. M. Donnelly, Appl. Phys. Lett. **93**, 261502 (2008).

[11] M. A. Lieberman, J. P. Booth, P. Chabert, J. M. Rax, and M. M. Turner, Plasma Sources Sci. Technol. **11**, 282 (2002).

[12] P. Chabert, J. Phys. D: Appl. Phys. **40**, R63 (2007).

[13] I. Lee, D. B. Graves, and M. A. Lieberman, Plasma sources Sci. Technol. **17**, 015018 (2008).

[14] H. Schmidt, L. Sansonnens, A. A. Howling, Ch. Hollenstein, M. Elyaakoubi, and J. P. M. Schmitt, J. Appl. Phys. **95**, 4559 (2004).

[15] L. Sansonnens and J. Schmitt, Appl. Phys. Lett. **82**, 182 (2003).

[16] A. Koshiishi, Y. Araki, S. Himori, and T. Iijima, Jpn. J. Appl. Phys., Part 1 **40**, 6613 (2001).

[17] A. Koshiishi, S. Himori, and T. Iijima, Jpn. J. Appl. Phys., Part 1 **46**, 4289 (2007).

[18] K. Takahashi, M. Hori, and T. Goto, J. Vac. Sci. Technol. A **14**, 2011 (1996).

[19] M. Nakamura, H. Nakayama, M. Ito, M. Hori, T. Goto, A. Kono and N. Ishii, Jpn. J. Appl. Phys. Part 2 **38**, L1469 (1999).

[20] M. Nakamura, M. Hori, T. Goto, M. Ito and N. Ishii, J. Vac. Sci. Technol. A **19**, 2134 (2001).

[21] M. Nakamura, M. Hori, T. Goto, M. Ito and N. Ishii, J. Appl. Phys. **90**, 580 (2001).

[22] H. Nakagawa, M. Okigawa, S. Morishita, S. Noda, H. Hayashi, K. Ito, M. Inoue and M. Sekine, Jpn. J. Appl. Phys. Part 1 **41**, 319 (2002).

[23] C. Suzuki, K. Sasaki, and K. Kadota, J. Appl. Phys. 82, 5321 (1997).

[24] H. Kokura, K, Nakamura, I. P. Ghanashev, and H. Sugai, Jpn. J. Appl. Phys. **38,** 5262 (1999).

[25] K. Denpoh and P. L. G. Ventzek, J. Vac. Sci. Technol. A **26**, 1415 (2008).

[26] K. Ishikawa, S. Hayashi, and M. Sekine, J. Appl. Phys. **93**, 1403 (2003).

[27] D. M. Phillips, J. Phys. D: Appl. Phys., Vol. **8**, 507 (1975)

[28] H. Hayashi, S. Morishita, T. Tatsumi, Y. Hikosaka, S. Noda, H. Nakagawa, S. Kobayashi, M. Inoue, and T. Hoshino, J. Vac. Sci. Technol. A **17**, 2557 (1999).

[29] C. Bohm, and J. Perrin, Rev. Sci. Instrum. **64**, 31 (1993).

[30] C. Koshimizu, T. Ohta, T. Matsudo, S. Tushitani, and M. Ito, Applied Physics Express **3**, 056201 (2010).

Chapter 6

Study on Physical Properties of Plasma Generated by YAG Laser in Liquid

6.1 Introduction

Although a large number of studies have been made on laser-produced plasmas on solid surfaces [1, 2] and in gas phases [3, 4], little is known about the laser-produced plasma in a liquid. Thus, the purpose of this study is to clarify the physical properties of the laser-produced plasma in a liquid. One of the applications of this study is to improve the quality of water by resolving environmental pollutants. Especially, the endocrine disruptor chemicals, such as the polychlorinated biphenyl (PCB), bisphenol A, being included in the waste water discharged from factories etc. cause some problems. However, the laser-produced plasma in liquid may avoid the problem, because the polluted materials can be decomposed by this plasma with a high efficiency due to a high electron density or electron temperature. The dimensions of the laser-produced plasma are not generally large (depending on beam size of laser). This becomes one of the problems in the efficient removal. Thus, we study a laser-produced plasma in liquid to obtain the information on the optimum conditions and properties for efficient plasma

generation.

The plasma was generated by focusing Nd:YAG laser beam in liquid. The ultra pure water with NaCl dissolved up to 24 % was used as a test liquid. NaCl was used as an impurity.

The breakdown threshold was observed at NaCl concentrations up to 24 %. When the NaCl concentration was 0 %, the threshold intensity was about 2×10^{14} W/m^2. It decreased with increasing NaCl concentration.

The laser light in liquid is attenuated by absorption and scattering. Thus, the accurate light intensity in liquid must be corrected by knowing the loss coefficient. The loss coefficient was measured to be about 3 m^{-1}.

The electron density of laser-produced plasma in liquid was measured by a laser interferometer. Two different probe laser sources (Ar-ion laser and He-Ne laser) were used to estimate the influence of the refractive index of neutral atoms. Then, electron density distribution on the optical axis of the YAG laser was measured. It is found that this plasma had a high electron density of the order of 10^{25}-10^{26} m^{-3}.

The electron temperature was measured by using spectral line intensity ratio obtained from the spectroscopic analysis. Spectral lines emitted by every atom (H, O, Na, Cl) included in the liquid was observed. According to a result obtained from the emission lines of H atoms, the electron temperature was about 5000 K.

6.2 Experimental setup

The experimental setup is shown in Fig. 6.1. A Nd:YAG laser with a second harmonic wavelength of 532 nm was used, which had a maximum energy of 180 mJ and a full-width at half maximum pulse duration of 15 ns. The laser power was controlled

by an optical filter, and the laser beam was focused by a lens with a focal length of 60 mm placed outside of the liquid in a chamber. The chamber is as large as 75×45×70 mm, and it is made of acrylic and has three windows of quartz glass. The quartz glass has a height of 25 mm, a width of 30 mm and a thickness of 2 mm. The ultra pure water or the ultra pure water with dissolved NaCl was used as a test liquid. The NaCl concentration was changed from 0 % to 24 %. The focal spot diameter measured by knife edge method was about 80 μm in the water.

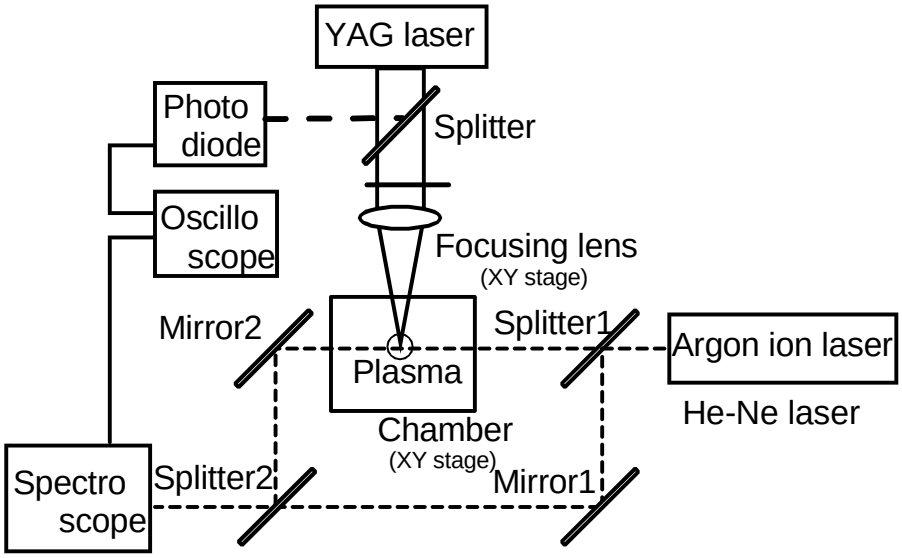

Figure 6.1 Experimental setup.

The electron density of the laser-produced plasma was measured by means of a Mach-Zender interferometer using an Ar-ion laser. To remove the influence of refractive index of neutral atoms, the density was also measured by using a He-Ne laser and only the electron density of plasma was obtained by taking the difference of two results. When the electron density distribution on the optical axis was measured, the position of the focusing lens and the chamber was moved by X-stage, while the position of probe laser was fixed. The spectroscope was used as a detector in the interferometer to prevent

the influence of stray light.

In order to estimate the electron temperature, the emission spectral intensity was obtained by spectroscopic analysis. The emission spectrum was observed by imaging the light emitted from the plasma onto the input slit of the spectroscope, using a relay lens with a focal length of 100 mm. The spectrum was obtained in the wavelength range from 240 nm to 850 nm in steps of 0.1 nm. The spectroscope was the Czerny-Turner type with a focal length of 1 m and a resolution of 0.016 nm.

6.3 Breakdown threshold

When the laser light was focused in liquid, it was visually observed whether the plasma was produced or not. The plasma production probability plotted against the light intensity is shown in Fig. 6.2. The plasma production probability was a percentage of plasma production in 20 laser irradiations. The plasma was hardly generated when the light intensity was lower than the breakdown threshold, but the plasma production probability increases rapidly when the light intensity exceeded the breakdown threshold. When the intensity was high, the plasma was practically always generated. With increasing NaCl concentration, the plasma was generated at lower light intensities.

Figure 6.3 shows a breakdown threshold light intensity against the NaCl concentration. The threshold intensity was the light intensity at which the plasma production probability was 50 %. The threshold decreased with increasing NaCl concentration. It is assumed that the plasma in liquid was generated by inverse-bremsstrahlung absorption of laser light and cascade ionization as in high pressure gas [3]. As the elastic collision cross section of Na atom with an electron was higher than that of another atom included in the test liquid, the threshold decreased with increasing NaCl concentration.

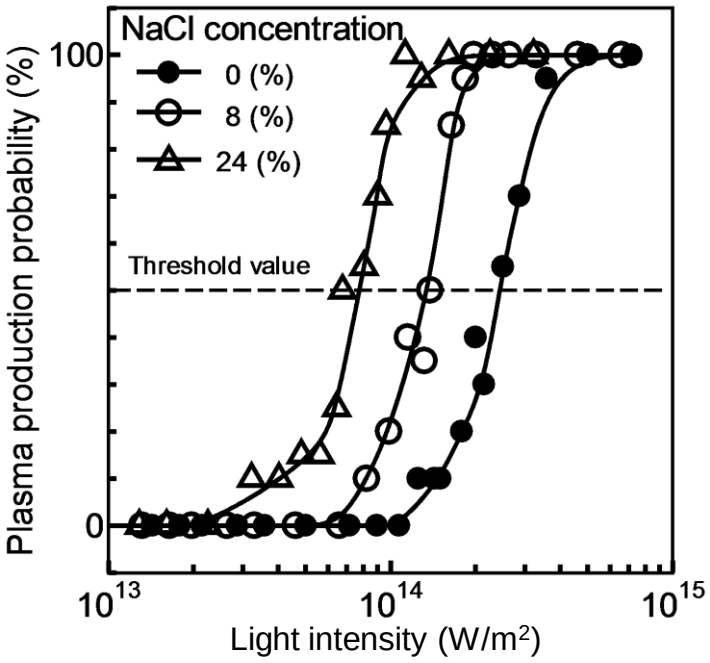

Figure 6.2 Plasma production probability.

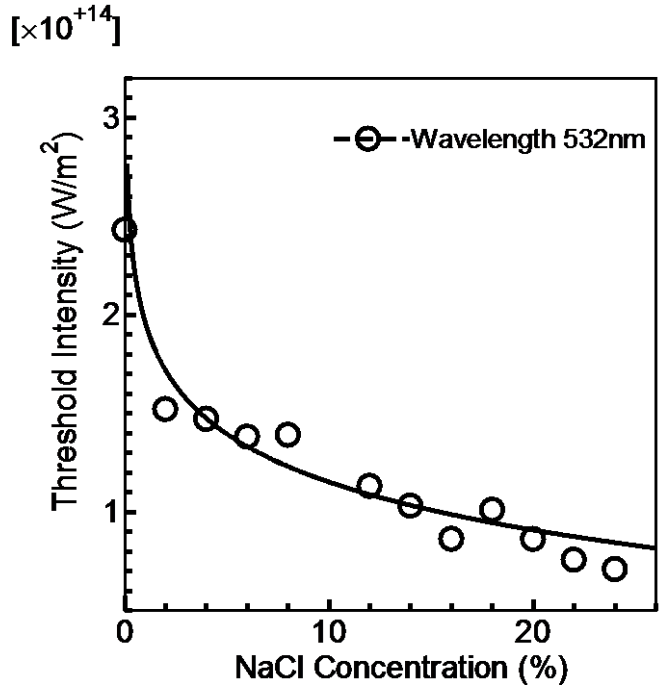

Fig 6.3 Breakdown threshold intensity.

6.4 Loss coefficient

When the laser irradiated the liquid, the laser light was attenuated by absorption and scattering in liquid. The laser light intensity propagating in liquid was given by Lambert's law,

$$I = I_0 \exp(-\alpha d) \tag{6.1}$$

where I is the transmitted light intensity, I_0 is the incident light intensity, α is the loss coefficient and d is the optical length. The optical length d is 45 mm. The incident light intensity on the chamber and the transmitted one were measured, and the loss coefficient was calculated from eq. (6.1). A measured loss coefficient is shown in Fig. 6.4. Even if the NaCl concentration was changed, the loss coefficient was almost constant and was about 3 m^{-1}. The measured absorption coefficient of water using an incoherent light source was about 3.6×10^{-2} m^{-1} when the wavelength is 532 nm [5]. Thus, the influence of the scattering was so large that the absorption could be ignored and the loss coefficient was not dependent on the NaCl concentration.

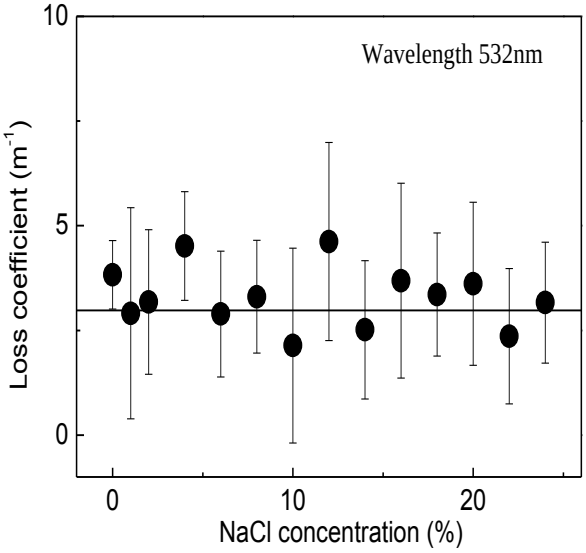

Figure 6.4 Loss coefficient.

6.5 Electron density

The electron density of the laser-produced plasma in liquid was measured by using the Mach-Zender interferometer. Ar-ion laser was used as a probe laser. An example of interferometric signals and the laser pulse are shown in Fig. 6.5. It is difficult to find out a turning point in the fringe pattern at which the electron density reaches a maximum. It is assumed that the laser pulse is very short compared with measuring time and the electron density decreases monotonically in the measurement time. An example of the extrapolation is shown in Fig. 6.6.

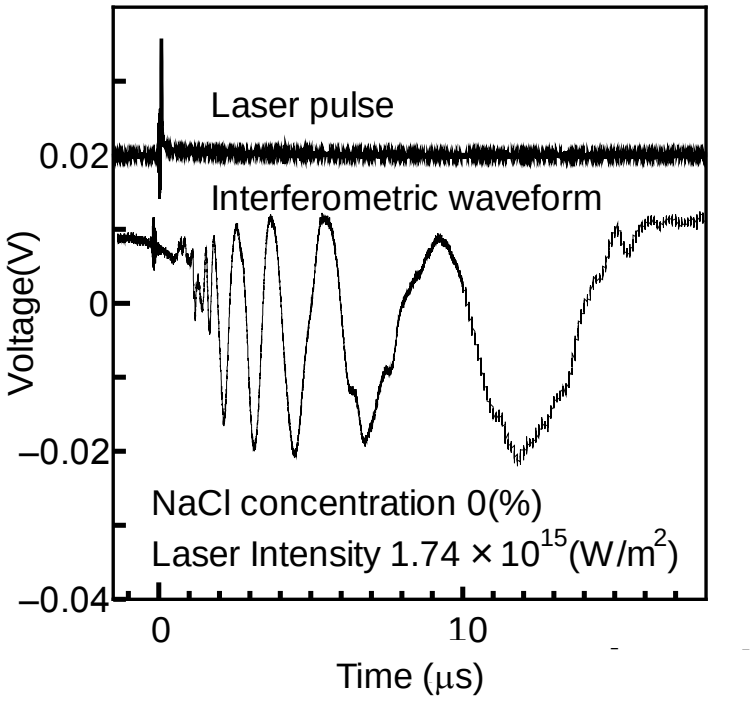

Figure 6.5 Interferometric signal and laser pulse.

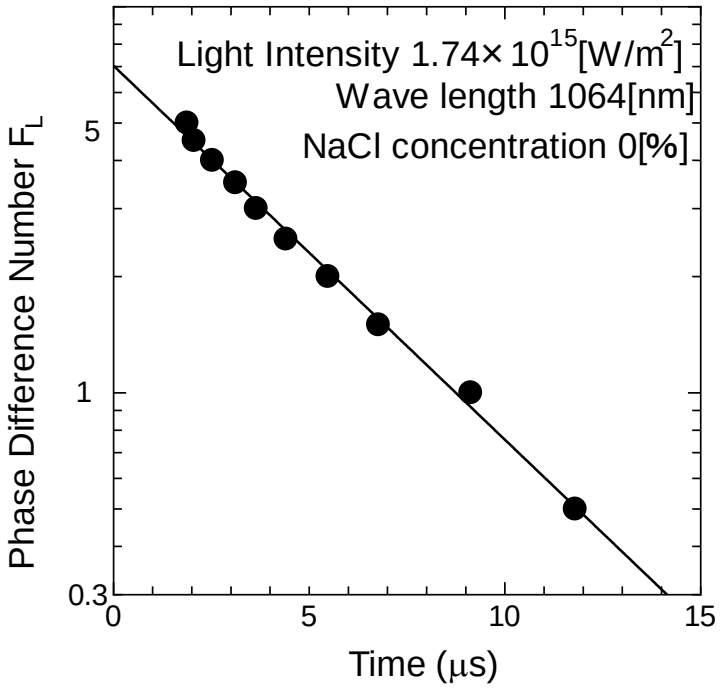

Figure 6.6 Example of extrapolation.

The maximum electron density was obtained from the following equation by estimating the maximum fringe number F_L,

$$n_e = 2.18\times10^{15}\frac{F_L}{L\lambda} \tag{6.2}$$

where n_e is the electron density, L is the optical length of the probe laser and λ is the wavelength of the probe laser. The optical length L necessary to estimate electron density from the fringe number was calculated from the spot diameter of YAG laser and theoretical optical path of Gaussian beam, where L is 0.08 mm at the focal point and 0.165 mm at the position of -1mm.

Fig. 6.7 shows the electron density distribution of the plasma on the YAG laser optical axis obtained from eq. (6.2). The error bar shows a maximum deviation in 5 time measurements. When the light intensity of YAG laser was 1.3×10^{15} W/m^2 at the focal

spot, and the NaCl concentration was 0 %, the dense plasma with electron density of the order of 10^{26} m^{-3} was obtained. The electron density was highest at the focal spot. Moreover, the laser-produced plasma in liquid developed not only backward but also forward, and the electron density decreased with increasing distance from the focal spot. The electron density of backward plasma was observed in a wider range than that of forward one. The YAG laser light was almost reflected by plasma, and it could not sufficiently transmit to forward because the plasma frequency was almost the same as the laser frequency.

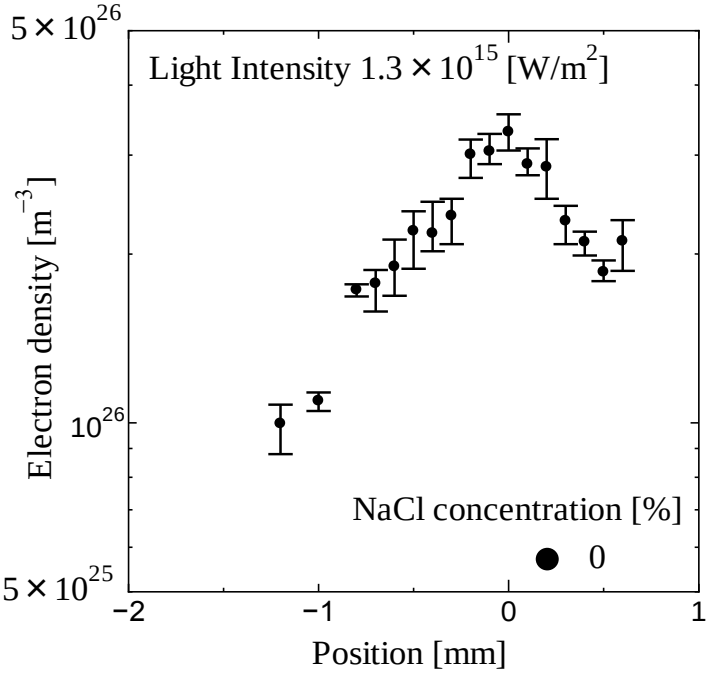

Figure 6.7 Electron density distribution.

The electron density of laser-produced plasma in liquid may be estimated by a single probe laser. However, the influence of the neutral atom also has to be considered. As the density of the neutral atom changes temporally with changing density of the

plasma, the refractive index measured by the single probe laser can not accurately estimate only the density of the plasma. The electron density was also measured by using He-Ne laser as a probe laser. Then, the density of plasma free from the influence of the neutral atom can be obtained by using the following equation from the result measured by Ar-ion laser and that by He-Ne laser [6],

$$n_e = \frac{n_{(Ar)} - n_{(He-Ne)}}{4.5\times10^{-16}(\lambda^2_{(He-Ne)} - \lambda^2_{(Ar)})} \tag{6.3}$$

where $n_{(Ar)}$ is the average refractive index change for Ar-ion laser, $n_{(He\text{-}Ne)}$ is the average refractive index change for He-Ne laser, $\lambda_{(Ar)}$ is the wavelength of Ar-ion laser, and $\lambda_{(He\text{-}Ne)}$ is the wavelength of He-Ne laser.

The electron density distribution on optical axis by He-Ne laser is shown Fig. 6.8. The electron density measured by He-Ne laser was of the order of 10^{26} m^{-3} and highest at the focal spot and decreased with increasing distance from it as well as the result measured by Ar-ion laser. However, the electron density measured by He-Ne laser was always lower than that by Ar ion laser. Then, by taking the difference of the refractive index obtained by Ar-ion laser and that by He-Ne laser, the density of only the plasma was obtained as shown in Fig. 6.9. The electron density estimated by using Eq. 6.3 was of the order of 10^{25}-10^{26} m^{-3} when the light intensity of YAG laser was 1.3×10^{15} W/m^2 at the focal spot. As the error increased by taking the difference of the two average refractive index changes, it is difficult to get the accurate electron density distribution. However, the electron density calculated by Eq. 6.3 was of the same order as that measured by only Ar-ion laser. It is considered that the influence of the neutral atom was not so large that the electron density of plasma could be approximately estimated by only Ar-ion laser.

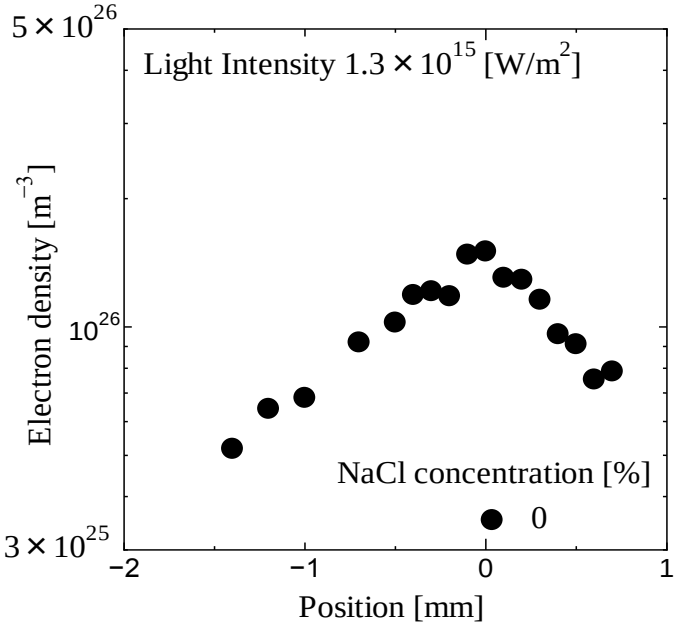

Figure 6.8 Electron density by He-Ne laser.

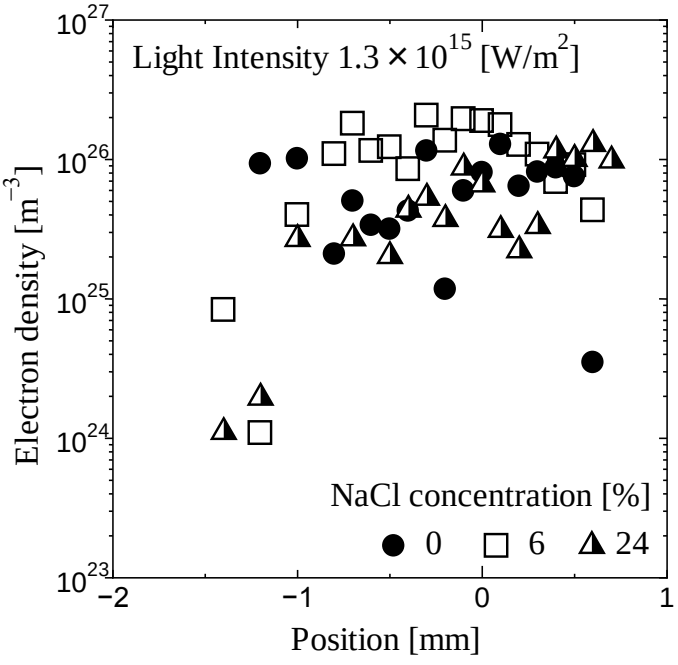

Figure 6.9 Electron density of laser-produced plasma removed the influence of the neutral atoms.

The dependence of the electron density measured by Ar-ion laser on NaCl concentration is shown in Fig. 6.10 and Fig. 6.11. When the intensity of YAG laser was high, and NaCl concentration was 0 %, the electron density had a peak at the focal spot. A similar trend was shown not only at higher intensity but also at lower intensity. The effect of NaCl was particularly appeared in the condition of the lower light intensity and higher NaCl concentration as shown in Fig. 6.11. When NaCl concentration was 0 and 6 % at the lower light intensity, fringe pattern was not detected at backward over -0.5 mm because the light intensity was low, and therefore the electron density could not be observed. On the other hand, in the condition of NaCl concentration 24 %, the dense plasma of the order of 10^{26} m^{-3} was observed in a wider region than that at lower concentration as the elastic collision cross section of Na atom with an electron was higher than that of another atom included in the test liquid. However, in the condition of higher NaCl concentration or higher light intensity, the ionization was caused at wide position, and the highest of electron density did not necessarily correspond to the focal spot.

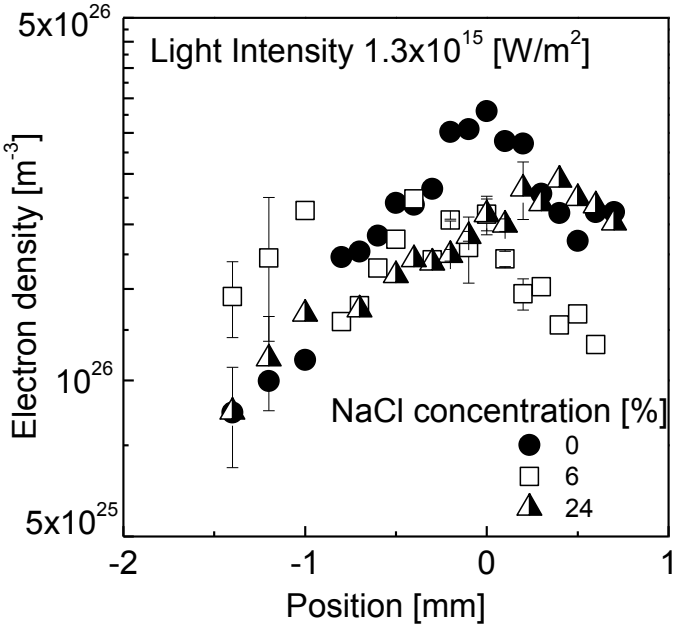

Figure 6.10 Electron density distribution at higher light intensity.

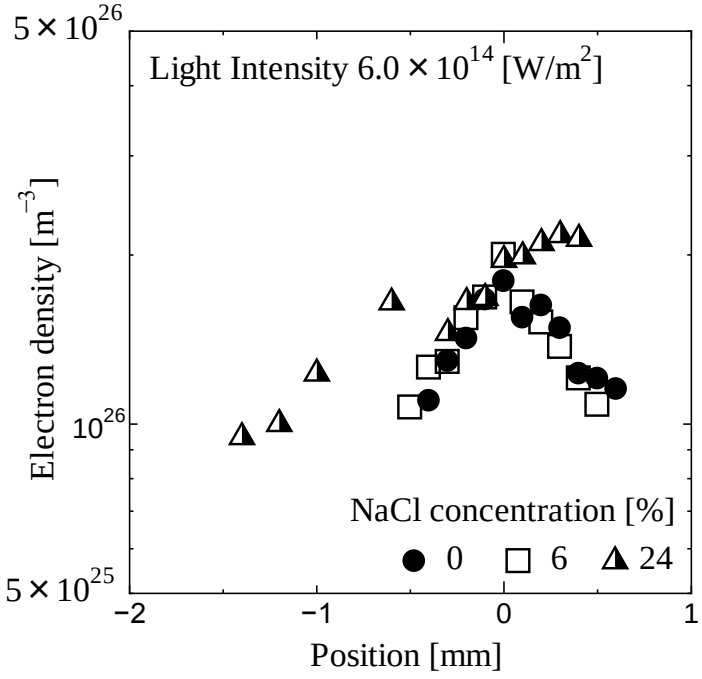

Figure 6.11 Electron density distribution at lower light intensity.

6.6 Electron temperature

In order to estimate the electron temperature, the spectral intensity emitted from the plasma was obtained by spectroscopic analysis. Fig. 6.12 shows the spectral intensity signal at the wavelength of 386.9 nm and the laser pulse. The spectral signal from the plasma rises after about 20 ns from the laser pulse, and its full-width at half maximum is about 80 ns. Fig. 6.13 shows the spectrum obtained from the peak value of the spectral signal in the range from 240 nm to 850 nm. The peak time of the spectral signal was almost constant for all the measured wavelengths. The spectral line from every atom (H, O, Na, Cl) included in the liquid was observed [7]. Especially, H atom had lines in a range from visible region to near-ultraviolet, and its lines were observed well. The line in the vicinity of 532 nm was scattered light of YAG laser beam.

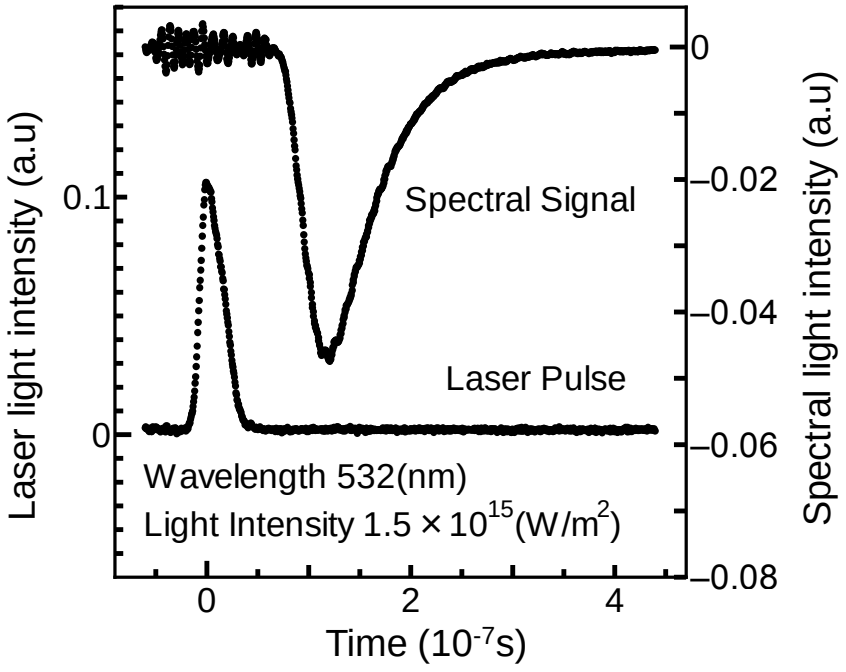

Figure 6.12 Spectral signal and laser pulse.

As the electron density was as high as the order of 10^{25}-10^{26} m^{-3}, the radiation and absorption process in the plasma could be generally ignored compared with the collision process. Thus, the electron temperature of the plasma was calculated using the following equation [8]

$$\ln\frac{I_{21}\lambda_{21}}{A_{21}g_2} = -\frac{E_2}{kT_e} + \ln C \tag{6.4}$$

where I_{21} is the spectral intensity, A_{21} is the transition probability, g_2 is the statistical weight, λ_{21} is the transition wavelength, E_2 is the upper level energy, T_e is the electron temperature, k is the Boltzmann constant and C is a constant. Thus, the electron temperature was calculated from the gradient by plotting the spectral intensity as a function of the upper level energy E_2 as shown in Fig. 6.14. The electron temperature calculated from the emission lines of H atom is about 5000 K. The wavelength λ_{21}, the lower energy level E_1, the upper energy level E_2, the statistical weight g_2 and the transition probability A_{21} of Hydrogen used for calculation of electron temperature are shown in Table 6.1.

Table.6.1 Emission line of Hydrogen

λ_{21} [nm]	E_1 [eV]	E_2 [eV]	g_2	A_{21} [sec^{-1}]
386.9	10.20	13.39	128	2.22E+05
435.1	10.20	13.06	50	2.53E+06
483.4	10.20	12.75	32	8.42E+06
676.3	10.20	12.09	18	4.41E+07
845.0	12.09	13.55	578	3.44E+03

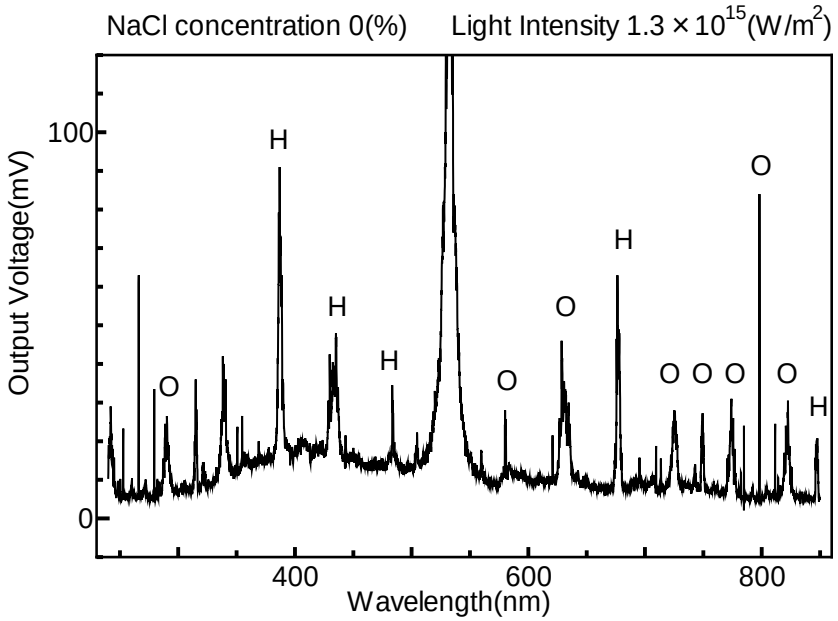

Figure 6.13 Spectrum.

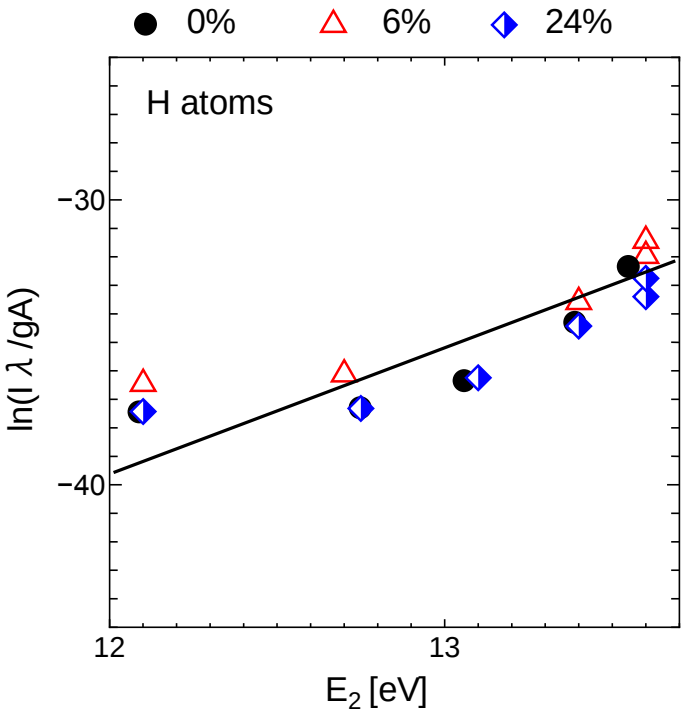

Figure 6.14 Light intensity of measured H lines as a function of upper energy level.

6.7 Summary

The physical properties of the plasma produced when YAG laser beam is focused in liquid have been studied. The electron density of the plasma was measured with a laser interferometer. The dense plasma with electron density of the order of 10^{25}-10^{26} m^{-3} was obtained. The electron density was highest at the focal spot, and decreased with increasing distance from it. Even if the light intensity was changed, the electron density at focal spot was almost a constant.

In order to estimate the electron temperature, the spectral intensity emitted from the plasma was observed with a spectroscope. As the electron density was high, the electron temperature of the plasma was calculated using the spectral line intensity ratio. The electron temperature calculated from the emission lines of H atom was about 5000 K.

Reference

[1] R. Kodama, P. Norreys, K.Mima, et al.: Nature 412, 798.

[2] Tabak M, Clark DS, Hatcheff SP, et al. PHYSICS OF PLASMAS Volume: 12]

[3] N. Tsuda and J.Yamada: Jpn. J. Appl. Phys. 38 (1999) 3712.

[4] N. Tsuda and J.Yamada: J. Appl. Phys. 81 (1997) 582.

[5] G. M. Hale and M. R. Querry: Appl. Opt. 12 (1973) 555.

[6] S. Takeda: Plasma no kiso (fundament of plasma) (Asakurasyoten, Tokyo,1966) p. 186 [in Japanese]

[7] A.R. Striganov and N. S. Sventitskii: *TABLES OF SPECTRAL LINES OF NEUTRAL AND IONIZED ATOMS* (IFI/PLENUM, New York, 1968) p.73

[8] M. Yamamoto and S. Murayama: Plasma no bunnkoukeisoku (spectroscopy of plasma) (Gakkaisyuppanncenter, Tokyo, 2002) p.116 [in Japanese]

Chapter 7

Conclusions

7.1 Summary of this thesis

In the plasma application processes, the plasma generation and the control for each process are needed and it is important to understand the reaction processes in the plasma and on the surface. The development of the plasma generation and control technology based on the plasma science, the plasma diagnostics technology and a new plasma application process are demanded and advanced. In Chapter 3, 4 and 5, the author described a dual frequency capacitively coupled plasma (CCP) with negative dc bias superposed on VHF power on the upper electrode. In the process for fabricating ULSI, it is necessary to realize anisotropic etching with a high aspect ratio, the high etching rate, and a high etching selectivity over photo resists and underlying materials, as well as the high repeatability and the high uniformity. In order to achieve such high etching performances, the dc superposed dual frequency CCP have been proposed as a new technology for advanced plasma processing. However, there are no experimental reports, only computational results were published. Thus, any effects of the dc-superposition need to be analyzed and experimentally demonstrated. In Chapter 6, the physical properties of a laser-produced plasma in liquid were investigated. Although a large number of studies have been made on the laser-produced plasma on a solid

surface and in a gas, little is known about the laser-produced plasma in a liquid.

In Chapter 2, the theories of plasma absorption probe (PAP), laser Thomson scattering, Mach-Zender interferometer, laser induced fluorescence (LIF), vacuum ultra violet absorption spectroscopy (VUVAS) and optical emission spectroscopy (OES), which are mainly used in the present study for investigating the plasma characteristics, were described. The principles of X-ray photoelectron spectroscopy (XPS) and spectroscopic ellipsometer used for film properties characterization were introduced.

In Chapter 3, the author has reported measurements of the EEDF in dc superposed dual frequency capacitively coupled plasma using the methods of laser Thomson scattering. A non-Maxwellian EEDF was observed for all conditions. The non-Maxwellian EEDF could be considered as a summation of Maxwellian distributions of two groups of electrons. In other words, the EEDF was considered to contain separate low temperature and high temperature components. As the results, with increasing the superposed dc bias, the electron temperature in the low-energy part was increased while that in the high-energy part was decreased. When the superposed dc bias was increased from 0 to -410 V, the electron temperature in the low-energy part was slightly increased from 1.48 to 1.83 eV while that in the high-energy part was decreased from 3.37 to 2.18 eV. In a CCP at low pressure, the high temperature component of the EEDF was attributed to stochastic electron heating in the rf sheaths of the plasma. On the other hand, for a CCP driven by a combination rf and dc power sources, a dc/rf sheath develops on the negatively dc-biased electrode. The dc/rf sheath has a dc sheath has a dc region with negligible electron density near the negatively biased electrode. In the dc region, there is no electron heating because of its negligible electron density. Hence, if the rf power absorbed by the discharge is fixed, the rf and dc regions of the

voltage drop across the rf sheath are independent of dc voltage. As a result, the high temperature component of the EEDF was decreased because the dc source alters the sheath voltages and widths at the electrode surface. On the other hand, the results indicated the increase of electron density with increasing the dc bias voltage. When the superposed dc bias was increased from 0 to -410 V, the electron density increased from 2.2 to 2.8×10^{11} cm^{-3}. The dc source induces a dc current flow through the plasma and alters the sheath voltages and widths in the upper electrode. Secondary electrons are generated by positive ion bombardment of the electrode, and are accelerated by the sheath and injected into the plasma. As a result, the electron density increases by the application of the dc bias.

In Chapter 4, the dual frequency capacitively-coupled plasma (CCP) with superposed negative dc bias is investigated as an indispensable technology to realize selective etching of the interlayer dielectric SiOCH against the underlying barrier dielectric, SiC. This technique significantly improved the selectivity of the etching of SiOCH over SiC to 68.0 when a dc bias of -1200 V was superposed, compared to conventional CCP which shows a selectivity of only 5.5. For clarification, we did characterize experimentally by measuring the absolute densities of gaseous chemical species such as N, F, CF, and CF_2 for the first time to determine the mechanism of the selective etching. The densities of N and CF increased in conjunction with enhanced electron-impact dissociation, and conversely the densities of F, regarded as SiC etchants, decreased because by superposition of the negative dc bias, bulk densities of species such as CF_2 and F enhanced surface loss under highly energetic ion bombardment. This is notably that it opens to a new control method of bulk gaseous densities by utilizing application of a negative dc bias to the counter electrode; secondary electron emissions

at the surface of the electrode gained to increase the plasma density; dissociation of parent gases or molecules accelerated the generation of radicals in conjunction with enhanced electron-impact; also, it enabled moving the balance of generation and loss of radicals due to loss by consumption at the surface of the counter electrode made of silicon.

In Chapter 5, we investigated the spatial distribution of plasma parameters such as plasma density, gaseous temperature, and absolute CF and CF_2 radical densities in the dual frequency CCP with 60 MHz VHF superposed with negative dc bias. Applying a dc bias of −1000 V, the distribution of electron density was uniform within the radial position of about 130 mm. It was noteworthy that the spatial distributions of CF and CF_2 densities were also uniform in correlation with the uniform electron-density distribution. The measured CF and CF_2 radical density at the center were 7.0×10^{12} cm^{-3} for CF and 1.3×10^{13} cm^{-3} for CF_2. At positions above the heated surface of the Si-focus-ring, it evidenced for the ring temperature rise caused by temperature rise by plasma irradiation that the gas-temperature increase at least from about 530 K to about 630 K. Notably the CF_2 radical density was dropped to one-fourth of the center value. This was interpreted due to increased surface-loss-probabilities at the reactive ring surface with energetic ion bombardment and temperature rise. Oppositely, the distribution of CF radical density was uniform across the whole region. Thus, the temperature and material in the plasma reactor should be property selected in order to obtain uniform distribution, since the CF_2 radical density was affected by modified surface-loss probability coupled with the surface temperature. Moreover, the results of systematic measurements in this study will be very useful not only in the understanding of the kinetics of radicals but also in the development of computer simulation and the

design of the next generation's etch reactor.

In Chapter 6, the physical properties of the plasma produced when YAG laser beam is focused in liquid have been studied. The electron density of the plasma was measured with a laser interferometer. The dense plasma with electron density of the order of 10^{25}-10^{26} m^{-3} was obtained. The electron density was highest at the focal spot, and decreased with increasing distance from it. Even if the light intensity was changed, the electron density at focal spot was almost a constant. In order to estimate the electron temperature, the spectral intensity emitted from the plasma was observed with a spectroscope. As the electron density was high, the electron temperature of the plasma was calculated using the spectral line intensity ratio. The electron temperature calculated from the emission lines of H atom was about 5000 K.

7.2 Scope of future work

Reactive plasmas are widely used in several industries and also important in the large flat panel manufacturing industry. Plasma processes are indispensable for manufacturing the ULSIs. The author has investigated the dual frequency capacitively-coupled plasma (CCP) with superposed negative dc bias which has been proposed as advanced plasma processing in ULSI fabrication.

In Chapter 4, the author actually realized the highly selective etching of the interlayer dielectric SiOCH against the underlying barrier dielectric, SiC under c-C_4F_8/N_2/Ar plasma chemistry by using dual frequency CCP with a superposed negative dc voltage. Moreover, in Chapter 5, the author investigated the spatial distribution of plasma parameters in the dual frequency CCP with 60 MHz VHF superposed negative dc bias. The uniformity of electron density was realized by

applying a dc bias. The dc-superposed CCP will have a lot of advantages for high accuracy etching. Moreover, systematically measured results in this study will be so useful not only in the understanding of the kinetics of radicals but also in the development of computer simulation and the design of the next generation's etch reactor.

As a future work, it is necessary to collect more information as a function of dc superposition. Moreover, in this thesis, although authors considered electron and radicals such as N, F, CF and CF_2 to interpret the mechanism of the highly selective etching and improvement of the uniformity, actually other internal parameters such as other radicals and ions have to be considered for the sophisticated interpretation with reproducibility. Especially, the negative ions might become an important factor in the dc superposition because it is considered that negative ions emitted from deposited film on dc electrode are accelerated by the sheath as well as electrons. In addition, it is expected that the dc superposition technique can achieve not only the highly selective etching of SiOCH over SiC films and uniformity but also high accuracy processing such as a high selective etching over photo resist and an isotropic etching with a high aspect ratio.

Recently, plasma processes are also extended for the steel, biomedical, and toxic waste management industries. In Chapter 6, the author investigated the physical properties of plasma generated YAG laser in liquid. Although a large number of studies have been made on the laser-produced plasma on a solid surface and in a gas, little is known about the laser-produced plasma in a liquid. He actually clarified the physical properties of the laser-produced plasma in liquid. However, the research for the application is not performed. One of application of this study is to improve the quality of the water by resolving the environmental pollutants. Especially, the environmental

endocrine disruptor chemicals such as PCB, bisphenol A, being included in the waste water discharged from factories etc. cause serious problems for water pollution. Therefore, it is necessary to research for the application such as the removal effect of these contaminants in the future.

Acknowledgements

The present research was performed in Professor Hori and Professor Sekine Laboratory, Department of Electrical Engineering and Computer Science, Nagoya University. Author would like to appreciate his research advisor, Professor Masaru Hori, Department of Electrical Engineering and Computer Science, Nagoya University, for his guidance, advices, and encouragements through the course of this research. The author also would like to thank his vice-advisor, Professor Makoto Sekine, Plasma Nanotechnology Research Center, Nagoya University, for lots of valuable comments. At the same time, he wishes to express his gratitude to his vice-adviser, Professor Akihiro Kono, Department of Electrical Engineering and Computer Science, Nagoya University, for his valuable suggestions in preparing this thesis. The author also would like to thank his vice-advisers, Professor Keiji Nakamura, Department of Electrical and Electronic Engineering, Chubu University, for their guidance and valuable suggestions in preparing this thesis.

The author is enormous grateful to Professor Jun Yamada, Department of Electronic Engineering, Aichi Institute of Technology, Associate Professor Norio Tsuda, Department of Electronic Engineering, Aichi Institute of Technology, Professor Masafumi Ito, Department of Electrical and Electronic Engineering, Meijo University, Dr. Hiroyuki Kano, NU Eco-Engineering Co., Ltd., Associate Professor Hiroki Kondo, Department of Electrical Engineering and Computer Science, Nagoya University, Associate Professor Kenji Ishikawa, Plasma Nanotechnology Research Center, Nagoya University, Assistant Professor Keigo Takeda, Department of Electrical Engineering and

Computer Science, Nagoya University, for their valuable comments and suggestions. The author would like to acknowledge Dr. Seigo Takashima, Dr. Noboru Ebizuka, Dr. Inseob Bae, Dr. Fengdong Jia and Dr. Jagath Kularatne for their fruitful discussions and valuable suggestions.

The author would like to appreciate having the opportunity to research in Ruhr University Bochum, Germany, from January to March, 2009, in the course of International Training Program (Program for incubating young researchers on plasma nanotechnology materials and device processing, conducted by Japan Society for the Promotion of Science). He would like to greatly appreciate Professor Uwe Czarnetzki, Faculty for Physics and Astronomy, Ruhr University Bochum, for his special management and hearty supports in International Training Program. The author would like to thank, Mr. Yusef Celik who have researched in Prof. Czarnetzki Laboratory., Faculty for Physics and Astronomy, Ruhr University Bochum, for his ultimate kind supports of experiments.

The author would like to acknowledge Mr. Chishio Koshimizu, Mr. Yoshinobu Ohya at Tokyo Electron AT., Ltd and Dr. Shoji Den, Dr. Koji Yamakawa and Mr. Shunji Takahashi at Katagiri Engineering Co., Ltd. for their helpful advices and discussions.

The author also thanks sincerely Mr. Satoshi Kono, Mr. Kenichi Ando, Mr. Tetsuya Kimura, Mr. Tatsuya Komuro, who aided his experimental works carried out in this study and also expressed their valuable suggestions and discussions. The author thanks Dr. Wakana Takeuchi, Dr. Chang Sung Moon, Dr. Shingo Kondo, Mr. Hirotoshi Inui, Mr. Masayoshi Kashihara, Ms. Sachiko Iseki, Ms. Emi Shibata, Mr. Arkadiusz Malinowski, Mr. Hiroshi Yamamoto, Mr. Yusuke Abe, Mr. Takehiro Hiraoka, Mr. Hiroki Kuroda, Mr. Takuya Takeuchi, Mr. Hyung Jun Cho, Mr. Shang Chen, Mr. Lu Yi, Mr.

Kota Mase, Mr. Yuto Matsudaira, Mr. Hiroyuki Mikuni, Mr. Yudai Miyawaki, Mr. Hitoshi Watanabe, Mr. Yoshihiro Itani, Mr. Sho Kawashima, Mr. Tokushige Kino, Mr. Toshiyuki Kuroda, Mr. Hironao Shimoeda, Mr. Toshiya Suzuki, Mr. Shinpei Amasaki, Mr. Masanori Kato, Mr. Takayuki Kanda, Mr. Yusuke Kondo, Mr. Naoya Sumi, Mr. Tatsuya Hagino, Mr. Koji Yasuda, Mr. Leyong Yu, Ms. Lu Ya, Mr. Kohei Asano, Mr. Minyoung Ahn, Mr. Jun Kuki, Mr. Ryosuke Kometani, Mr. Atsushi Fukushima, Mr. Takeyoshi Horibe and all other students who have studied in Profeessor Hori and Professor Sekine Laboratory.

The author appreciates Ms. Tomoko Yokoi, Ms. Azusa Ohta, Ms. Megumi Oshigane, and Ms. Rie Nozaki for lots of encouragements and helpful advices in day-to-day life.

Finally, the author would like to appreciate his parents, his sister, all his teachers, and good friends.

Tsuyoshi Yamaguchi
February 2011

List of Papers

1. Original Papers

	Title	*Journal*	*Authors*
1	Property of Laser-Induced Plasma in Liquid	Journal of Plasma and Fusion Science Series Vol.8, pp.619-622 (2009).	N. Tsuda, T. Yamaguchi, and J. Yamada (Chapter 6)
2	Study on Physical Properties of Plasma Generated by YAG Laser in Liquid	IEEJ Transactions on Fundamentals and Materials Vol. 130 No. 7 Sec. A, pp.677-682 (2010).	T. Yamaguchi, N. Tsuda, and J. Yamada (Chapter 6)
3	Spatial Distributions of Electron, CF, CF_2 Radical Densities and Gas Temperature in dc-Superposed Dual-Frequency-Capacitively-Coupled Plasma Etch Reactor Employing c-C_4F_8/N_2/Ar gas	Japanese Journal of Applied Physics, (accepted).	T. Yamaguchi, T. Kimura, C. Koshimizu, K. Takeda, H. Kondo, K. Ishikawa, M. Sekine, and M. Hori (Chapter 5)
4	Measurement of Fluorine Atom Densities and Their Impacts on Highly Selective Etching of SiOCH Films over SiC in Negative DC Bias Superposed Dual Frequency Capacitively Coupled c-C_4F_8/N_2/Ar Plasma	Journal of Applied Physics, (submitted).	T. Yamaguchi, S. Takashima, K. Takeda, C. Koshimizu, H. Kondo, K. Ishikawa, M. Sekine, and M. Hori (Chapter 4)

2. International Conferences

	Title	*Conference*	*Authors*
1	Electron density of laser induced plasma in liquid	The 19th Europhysics Sectional Conference on the Atomic and Molecular, Physics of Ionized Gases, (2008)	N. Tsuda, T. Yamaguchi, and J. Yamada
2	Property of Laser-Induced Plasma in Liquid	14th International Congress on Plasma Physics, (2008)	N. Tsuda, T. Yamaguchi, and J. Yamada
3	Radical density distribution in Dual Frequency Capacitively Coupled Etching Plasma	13.European Summer School ”Low Temperature Plasma Physics: Basics and Applications”, (2008)	T. Yamaguchi, T. Kimura, K. Ando, K. Takeda, M. Sekine, and M. Hori
4	Behavior of Radicals in Dual Frequency Capacitively Coupled Etching Plasma	2nd Japanese-German Student Workshop on Plasma Science and Technology, (2008)	T. Yamaguchi, T. Kimura, K. Ando, K. Takeda, M. Sekine, and M. Hori
5	Laser Thomson Scattering Approach for Electron Density and Temperature in Dual Frequency Plasma Processing	The 8th International Workshop of Advanced Plasma Processing and Diagnostics Joint Workshop with Plasma Application Monodzukuri (PLAM), (2009)	K. Ando, T. Yamaguchi, T. Kimura, K. Takeda, K. Kubota, C. Koshimizu, A. Kono, M. Sekine, and M. Hori

	Title	*Journal*	*Authors*
6	Fluorocarbon Species Measured by LIF in Dual Frequency Plasma Processing	The 8th International Workshop of Advanced Plasma Processing and Diagnostics Joint Workshop with Plasma Application Monodzukuri (PLAM), (2009)	T. Kimura, K. Ando, T. Yamaguchi, K. Takeda, A. Kono, M. Sekine, and M. Hori
7	Measurements of Electron Energy Distribution Function in Dual Frequency Capacitively Coupled Plasma Using Laser Thomson Scattering	The 2nd International Conference on Plasma-NanoTechnology & Science, (2009)	K. Ando, T. Kimura, T. Yamaguchi, K. Takeda, K. Kubota, C. Koshimizu, A. Kono, M. Sekine, and M. Hori
8	Behavior of Rotational Temperature in Dual Frequency Capacitively Coupled Plasma	2nd International Symposium on Advance Plasma Science and its Application (ISPlasma2010), (2010)	T. Yamaguchi, T. Kimura, K. Takeda, C. Koshimizu, M. Sekine, and M. Hori
9	Investigation of VHF Capacitively Coupled Plasma with DC Bias for Low-k film	The 3rd International Conference on PLAsma-Nano Technology & Science (IC-PLANTS2010), (2010)	T. Kimura, T. Yamaguchi, K. Takeda, C. Koshimizu, M. Sekine and M. Hori

	Title	*Journal*	*Authors*
10	Highly selective etching of SiOCH over SiC films by Dual Frequency CCP with DC bias superimposed to upper electrode	AVS 57th International Symposium and Exhibition, (2010)	T. Yamaguchi, K. Takeda, C. Koshimizu, H. Kondo, K. Ishikawa, M. Sekine and M. Hori

3. Research Project

・13. European Summer School (Low Temperature Plasma Physics: Basics and Applications) in Germany, 2008

・International Training Program (Program for incubating young researchers on plasma nanotechnology materials and device processing, conducted by Japan Society for the Promotion of Science) in Ruhr University Bochum, Germany, from January to March, 2009

4. Award

・Scholarly Encouragement Award, Nagoya University, Japan (2008).